Searching for Nucleus Obscuration in the Infrared Spectra of Nearby FR-I Radio Galaxies

by

Robert Gleisinger

A Thesis submitted to the Faculty of Graduate Studies of
The University of Manitoba
in partial fulfillment of the requirements of the degree of

MASTER OF SCIENCE

Department of Physics and Astronomy
University of Manitoba
Winnipeg

Abstract

Why are there so many types of active galactic nuclei (AGN)? Astronomers have proposed numerous AGN unification models to explain the vast array of different AGN types with a single type of object. The most prominent of these features a supermassive black hole's accretion disk obscured by a torus of discrete dusty clouds. The applicability of this model to low-luminosity AGN such as Fanaroff & Riley class I (FR-I) radio galaxies is controversial. We present a wide-band infrared spectroscopic analysis of ten nearby FR-I radio galaxies. We used Markov-chain Monte Carlo algorithms to fit a set of models to *Spitzer*/IRS spectra with wide-band behaviour constrained by photometry from 2MASS, *Spitzer*/IRAC, *Spitzer*/MIPS, and *Herschel*/SPIRE. We find one galaxy is best fit by a torus and three others show some thermal mid-infrared component. We conclude that 40% of our FR-I radio galaxies show evidence of obscuring dusty material.

Contents

List of Figures

List of Tables

Contributions

This work has been done in collaboration with my advisor, Dr. C. O'Dea, as well as project members Dr. J. Gallimore, Dr. S. Wykes, and Dr. S. Baum.

Dr. O'Dea, in his role as advisor, has been a constant source of guidance throughout my time at the University of Manitoba. He initially suggested this project back when I was interning here as an undergraduate summer student at McGill University. His suggestions helped me to fit my work into the larger picture of active galactic nuclei. Most of the checks I performed between our results and the literature were based on his recommendations. Last, but most certainly not least, he was my primary source of feedback on every draft of this thesis and the associated paper which I hope to submit by the end of the summer.

Dr. Gallimore is the lead developer of the pahfitMCMC and clumpyDREAM software used in this project and he also ran the software as requested since he had the computation resources required to run the software in a reasonable time frame. Running clumpyDREAM on what resources we had available at the University of Manitoba early in the project took two weeks for one set of runs. In contrast, Dr. Gallimore was able to run the same set in about three days.

Dr. Wykes and Dr. Baum have both provided significant feedback on my earlier paper drafts which I eventually adapted into this thesis.

I assisted Dr. Gallimore in testing new versions of clumpyDREAM, adapted an older version of clumpyDREAM's fake galaxy spectrum creation code, adapted clumpyDREAM's plotting code to produce plots more appropriate for this format, performed all the checks

against the literature recommended by Dr. O'Dea, wrote the code to get useful diagnostic information from pahfitMCMC's line fits, extracted IRAC and MIPS photometry from archival data and informed the restrictions required to produce the Bayesian priors necessary for the more general clumpyDREAM to properly fit FR-I sources.

Acknowledgements

I would like to thank my parents and grandmother for their constant support, my friends for the distraction when I really needed one, and Diesel (my Mom's husky-german shepherd mix) for always putting a smile on my face.

On a more formal note, I'd like to thank my advisor, Chris O'Dea, for his guidance and patience through the last two-and-a-bit years. I probably wouldn't be at the University of Manitoba at all if I hadn't sent an email to this random University of Manitoba professor, of whom I'd never previously heard, while looking for an internship three years ago. He was usually able to get me around a problem on which I had gotten stuck when I would have otherwise just kept (figuratively) beating my head against the screen. He often encouraged me to present my work, even before I was really comfortable doing so, which allowed me to meet many new people and put me in the position to figure out my next step.

I'd especially like to thank my collaborator, Jack Gallimore, since without his codes and computer time this project would have had to be written in IDL and run on a machine with only eight available cores i.e., not impossible but pretty close.

Thanks (and perhaps apologies) to my remaining committee members, Samar Safi-Harb and Jennifer Van Wijngaarden for agreeing to read this thesis in a timescale that is rather more compressed than is ideal for its $\sim 100-$page length without seeing it first. Also, Samar's outgoing demeanour and scientific insights made the astronomy-group meetings into far more enjoyable events than they would likely have been otherwise.

Next are my other collaborators, Sarka Wykes and Stefi Baum, who I'd like to thank for

their feedback on earlier iterations of what would become this thesis.

I'd like to thank Maiko Langelaar for figuring out my confusing computer needs and for fixing what I broke while trying to fix something else by myself.

I'd like to thank my fellow rear-of-501 astronomy graduate students Erica Franzmann, Ben Guest, Mainak Singha, and Victor Arendt for their help getting computers to do what I want and their insight into some of the intricacies of the University of Manitoba system.

That finally brings me to my appreciation for the administrative assistants in the Department of Physics and Astronomy here at the University of Manitoba, especially Robyn Beaulieu and Susan Beshta. They made the otherwise seemingly sisyphean paperwork associated with funding, reimbursements, teaching assistantships, and course registration far more tolerable and far less stress-inducing on my part. Susan even went above and beyond by helping me look into scholarships outside the university.

Chapter 1

Introduction

Some galaxies have cores that outshine all their stars combined. A vast diversity of these active galactic nuclei (AGN) have been discovered and catalogued and it is clear that the only thing that could be powering them is accretion onto a supermassive black hole. This raises the question — why are there so many classes of AGN? What makes them distinct? Why are the optical spectra of some AGN dominated by optical line emission? Why are others powerful radio emitters?

To answer these questions some astronomers have proposed AGN unification models. The most successful of these is the clumpy torus model, in which those AGN which are relatively dim in visible light are dim because we are viewing the accretion disk though a torus composed of many small, warm, and optically thick clouds of dust and gas. In contrast, optically bright AGN are viewed face on so that the light from the accretion disk is unobscured. While this model has been very successful AGN with high optical luminosity its applicability to AGN with with low luminosity is controversial.

Therefore, we seek to determine whether there is evidence for a clumpy torus nucleus obscuration in a sample of ten nearby low luminosity radio galaxies. We used Markov-chain Monte Carlo fitting algorithms to fit spectral lines and an underlying spectral energy distribution to infrared (IR) observations.

We provide an overview of the concepts involved and previous evidence surrounding the possibility of nucleus obscuration in Section 1.1 followed by an overview of the IR instruments and surveys involved in data collection for this research in Chapter 2 along with the processing of our broadband ancillary data. We then describe our sample of FR-I radio galaxies in Chapter 3. In Chapter 4 we provide our analysis of the narrow spectral features in the *Spitzer*/IRS spectra for each source, with particular focus on AGN and star formation tracers and the 10 and 18 μm silicate features. In Chapter 5 we show the results of fitting various spectral energy distribution models to our entire broadband data set for each source and provide upper limits on any possible torus component (or equivalent mid-infrared thermal component) in those sources which do not require one. See Figure 1.1 for a flow chart summarising our analysis pipeline. In Chapter 6 we discuss the implications of the models which best agree with the observations, compare our results to those of previous authors, and consider potential extensions to this research involving the current and upcoming generations of telescopes.

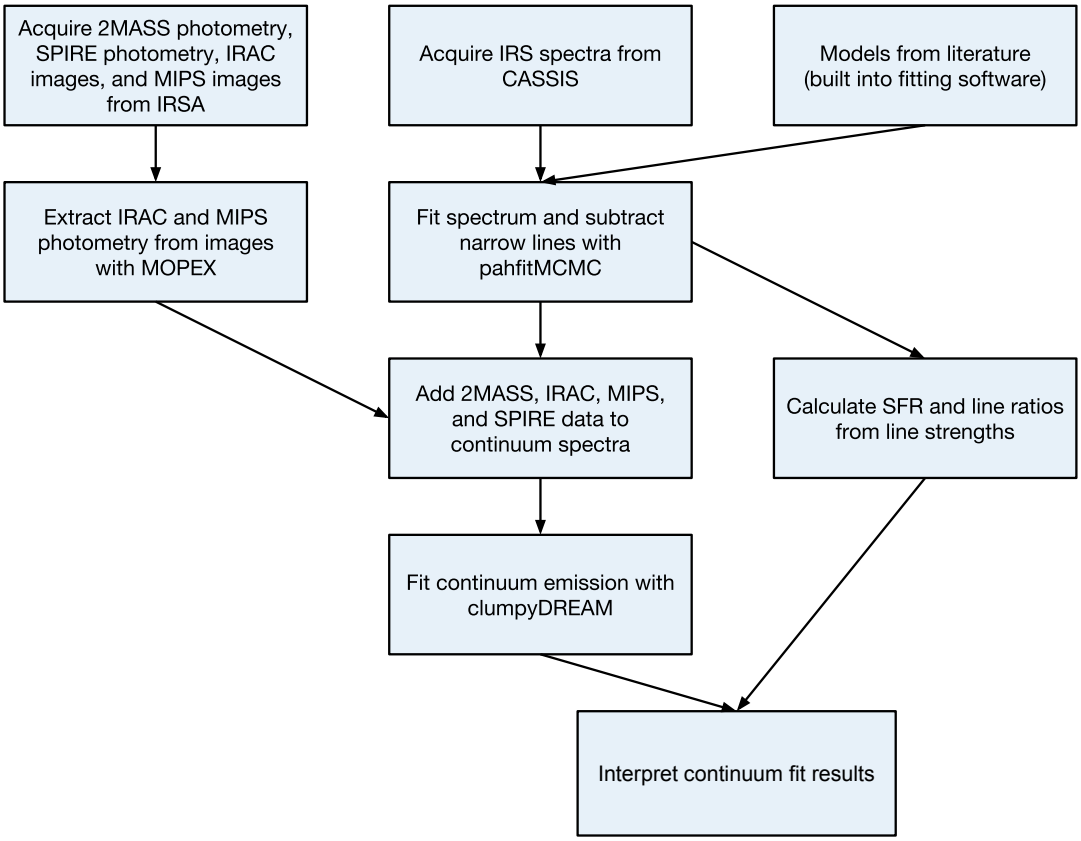

Figure 1.1 Flow chart depicting analysis pipeline.

1.1 Active galactic nuclei

As previously mentioned, active galactic nuclei (AGN) are highly luminous objects in the cores of some galaxies. AGN show a vast array of different spectra, collectively nicknamed the "AGN zoo", but are grouped primarily into broad categories based on their radio luminosities and the presence or absence of broad optical emission lines. Radio-quiet AGN include, for example, Seyferts and radio-quiet quasars. Most radio AGN are classified by the Fanaroff & Riley classes I and II described in Section 1.2 but Fanaroff & Riley class 0 radio galaxies have since been discovered. See Peterson (1997) for a basic overview of early AGN research and Padovani et al. (2017) for an update.

All AGN appear in the optical as point sources embedded within the extended source that is their host galaxy. In bands where galactic emission is brightest it can be difficult to detect AGN against the background, some AGN have low intrinsic luminosity, and in some others extinction by dust lanes within the host galaxy can obscure the AGN. Some AGN are still obvious, however, because the mechanism of emission in AGN is distinct from that in stars so they may be far brighter even in those bands where the stellar population is bright (e.g., quasars), they may show unusual line emission, or they may dominate the galaxy in bands where stars are dim (e.g., radio galaxies). Since some AGN classes can only be detected by some of these methods (e.g., radio galaxies are dim in optical and so are likely to be missed by optical surveys), each method is subject to selection biases which Padovani et al. (2017) describe in detail.

The spectral features of particular interest to us are those which can be prominent in the IR; they are especially prominent in the mid-infrared (MIR). These include a narrow line region, hot dust, cold dust, a synchrotron jet (see Section 5.1.1 for more on these), a warm and dusty obscuring torus (see Section 1.3.1) and those spectral lines which are tracers of astrophysical processes such as high-ionization lines (Section 4.2.2), silicate features (Section 4.2.3), and polycyclic aromatic hydrocarbon (PAH) lines which are tracers of star formation (Section 4.2.1). Another spectral feature which was relevant to sample selection is a nuclear

broad line region which is not visible in the total luminosities of our sample galaxies, although a hidden broad line region has been detected in NGC 315 (Barth et al., 1999) and 3C 270 (Antonucci, private communication) with spectropolarimetry via broad polarised Hα. These broad lines are Doppler-broadened by velocity dispersions between $\Delta v_{\mathrm{FWHM}} \approx 500\,\mathrm{km\,s^{-1}}$ and $\Delta v_{\mathrm{FWHM}} \approx 10^4\,\mathrm{km\,s^{-1}}$ with typical widths of $\Delta v_{\mathrm{FWHM}} \approx 5000\,\mathrm{km\,s^{-1}}$ (Peterson, 1997).

1.2 Fanaroff & Riley class I radio galaxies

In his review of faint radio sources, Padovani (2016) characterizes radio galaxies as galaxies with 1 GHz radio luminosities of $\geq 10^{22}\,\mathrm{W\,Hz^{-1}}$. These objects' radio luminosity is typically dominated by a synchrotron spectrum associated with a jet. These objects generally resemble quiescent elliptical galaxies in the optical.

Fanaroff & Riley (1974) originally described two main classes of high radio-power AGN which now bear their names. Fanaroff & Riley class I (FR-I) radio galaxies are low-luminosity radio galaxies with sub-relativistic jets that are brightest near their core whereas Fanaroff & Riley class II (FR-II) radio galaxies have higher radio luminosity and their radio emission is brightest from radio lobes which a can be far larger than the host galaxy. We show an example of each Fanaroff & Riley radio class in Figure 1.2. These lobes form at the ends of relativistic jets. Ledlow & Owen (1996) find a fairly sharp boundary between the two classes at

$$P_{178\,\mathrm{MHz}} \approx \frac{10^{26}}{\left(\frac{H_0}{70\,\mathrm{km/s/Mpc}}\right)^2}\,\mathrm{W\,Hz^{-1}} \tag{1.1}$$

or

$$P_{1.4\,\mathrm{GHz}} \approx \frac{2\times 10^{25}}{\left(\frac{H_0}{70\,\mathrm{km/s/Mpc}}\right)^2}\,\mathrm{W\,Hz^{-1}}. \tag{1.2}$$

They also found that the cut-off is dependent on optical luminosity but Gendre et al. (2013) have since refuted that.

FR-I jets are typically not straight and so have likely been affected by winds or buoyancy

in the intergalactic medium (IGM); this is in contrast to FR-II jets which are typically straight until they terminate in bright hot-spots. Indeed, Gendre et al. (2013) have found that radio galaxies in rich clusters are more likely to have FR-I morphology than those in field galaxies. For more details on extragalactic radio jets see Bridle (1984).

The hosts of FR-I radio AGN are typically, but not universally, giant ellipticals populated by low-mass red stars. In Section 1.3.2 we discuss what is currently considered to be the most likely reason, which is that low luminosity radio galaxies are powered by accretion from the hot IGM whereas high luminosity radio galaxies are more likely to be powered by cold gas accretion. Since said cold gas will also feed star formation, AGN fed by cold gas accretion will tend to reside in galaxies with bluer colours.

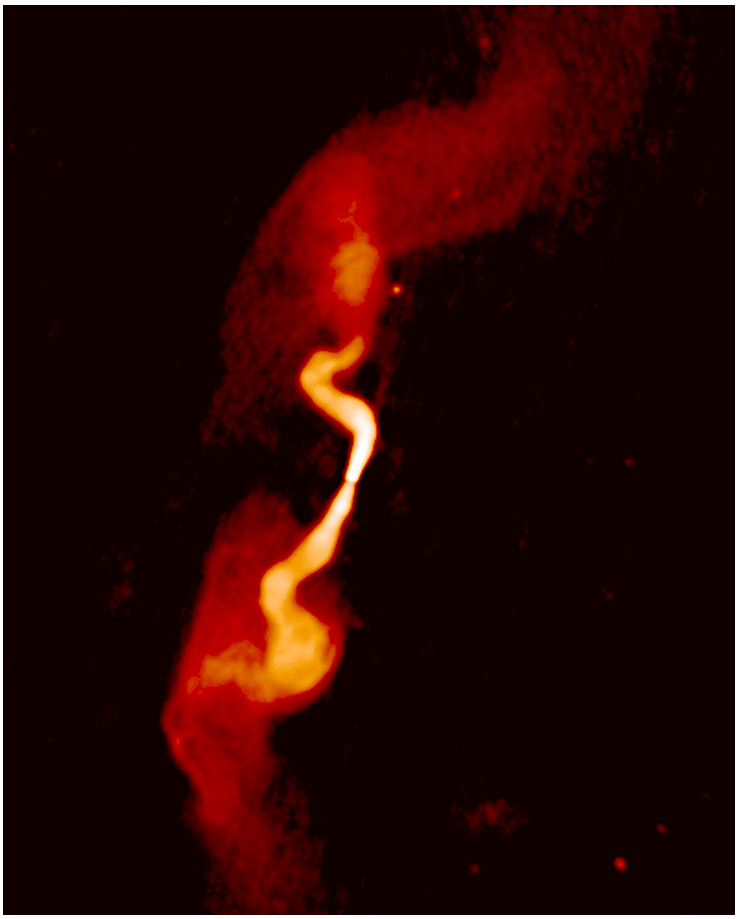

(a) 1.4 GHz VLA image of FR-I radio galaxy 3C 31 by Laing et al. (2008).

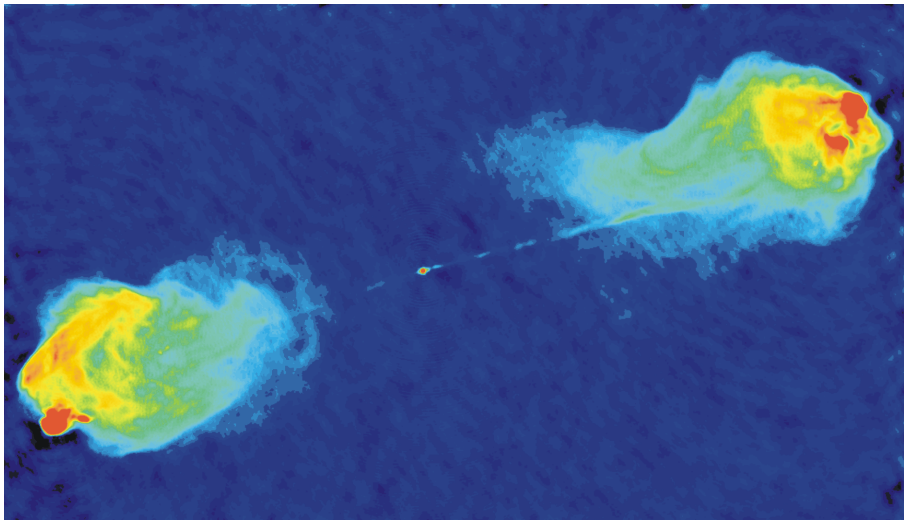

(b) 5 GHz VLA image of FR-II radio galaxy Cygnus A by Perley et al. (1984).

Figure 1.2 Radio images of examples of each of the two classes of radio galaxies. Note the straight jets and prominent hot spots at the ends of the jets in Cygnus A in contrast with the bent jets of 3C 31 which are brightest in the inner regions.

1.3 AGN unification

The vast set of different AGN types has prompted attempts to unify all of the various AGN types into a single model. These AGN unification models typically consist of a central engine, consisting of matter accreting onto a supermassive black hole as a geometrically thin accretion disk, and some anisotropic distribution of gas and dust which scatters, absorbs, or reflects light from the central engine. We show a simple diagram by Urry & Padovani (1995) of an early AGN unification model in Figure 1.3. Our description of this model follows those by Antonucci (1993) and Netzer (2015), see the former paper for an in-depth review of early thinking on AGN unification and the latter for a more up-to-date view. In such a model, the inner parts (central engine and broad line region) will be obscured from some angles by a warm torus of gas and dust producing AGN with low optical brightness along such near-equatorial sight lines. However, this torus would be transparent to radio waves, far-infrared, and hard X-rays and some optical line emission would be reflected into equatorial sight lines by narrow-line region (NLR) clouds out of the plane of the accretion disk. In contrast, high optical power sources such as quasars would have an unobstructed view of the accretion disk and broad line region which is composed of clouds near the accretion disk and so sees a much greater dispersion in radial velocity. If a relativistic jet is present, polar sight lines will see relativistic beaming which results in objects such as blazars. Figure 1.4 provides a cross-section of such an object similar to that depicted in Figure 1.3 and in particular depicts how such a source with low radio power would be classified as a Seyfert 1, 1.5, or 2 based on orientation alone.

Most early AGN unification models resemble that shown in Figures 1.3 and 1.4. The main driver of all AGN models is an accreting supermassive black hole (SMBH). In these early models, the accreting material forms an optically thick but geometrically thin accretion disk which is obscured from some lines of sight by an optically thick, warm ($\sim 200-1000\,\mathrm{K}$) mass of dusty material with a roughly toroidal geometry. This torus was believed to be clumpy (i.e., composed of discrete clouds) but Pier & Krolik (1992, 1993) originally modelled it as

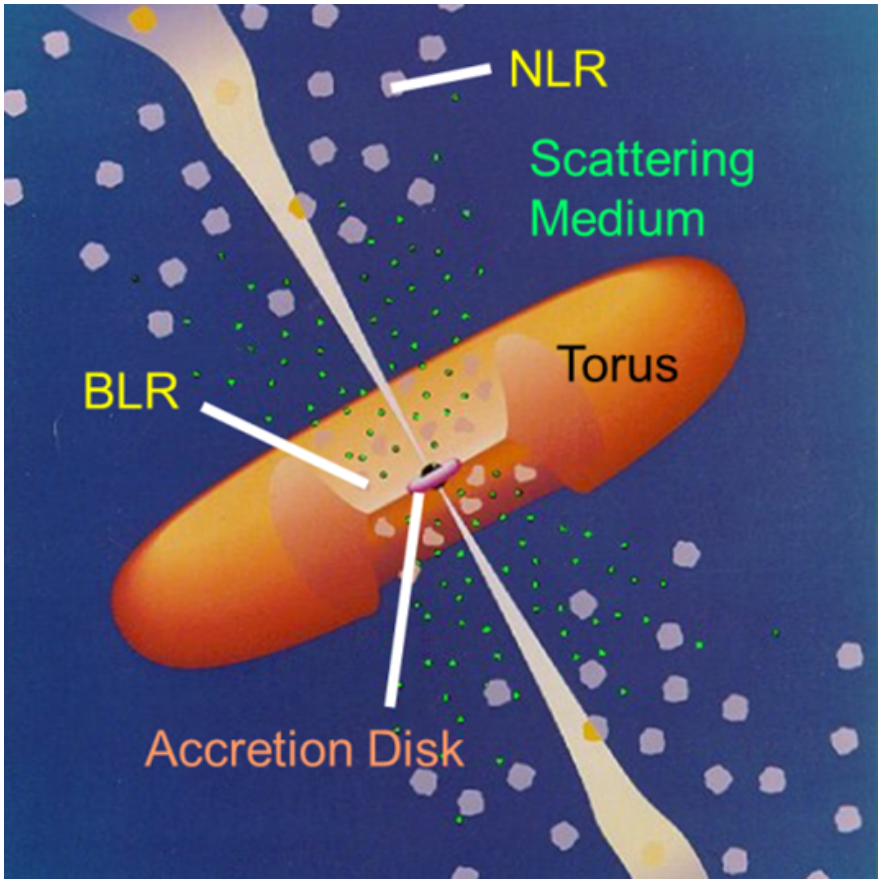

Figure 1.3 Diagram of an early smooth-torus AGN unification model by Urry & Padovani (1995).

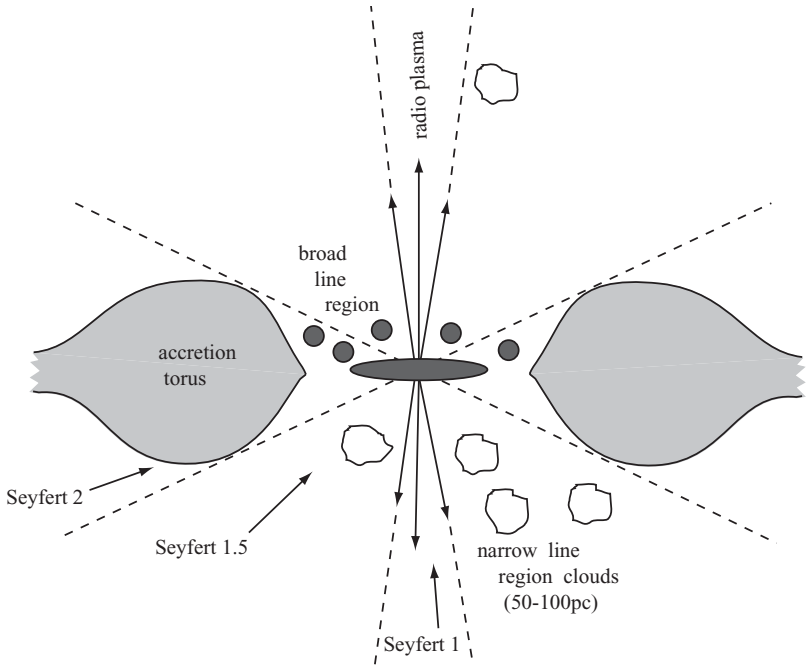

Figure 1.4 A diagram by Sparke & Gallagher (2007) of a smooth torus AGN unification model which demonstrates how line-of-sight effects can lead to various different observed AGN classes despite having a common physical object at their source.

a smooth continuous cloud of variable density due to computing constraints. Nenkova et al. (2002) modelled the clumpiness of the torus in a model which we describe in Section 1.3.1.

1.3.1 Clumpy torus model

Granato & Danese (1994) and Granato et al. (1997) found that the smooth torus model described in Section 1.3 requires fine-tuning in order to match the suppressed 10 μm silicate features observed in infrared spectral energy distributions. Now, any model that requires fine-tuning each object in a large population is suspect. Fortunately, Pier & Krolik (1992) had previously suggested that the torus could instead be clumpy although they could not model this "clumpy torus" model at the time. Rowan-Robinson (1995) found that clumpiness in the obscuring torus could adequately explain the silicate feature suppression in Seyfert 1 galaxies. Nenkova et al. (2002) formalised the clumpy torus model and they further refined the model in Nenkova et al. (2008a) and Nenkova et al. (2008b).

This clumpy torus model, which we show in Figure 1.5, describes an obscuring torus as being composed of small, discrete, optically thick clouds. The inner radius is generally set by the sublimation radius R_d for the component dust grains, the minimum distance from the central engine at which a grain can exist without sublimating, which Nenkova et al. (2008b) give as

$$R_d \sim 0.4\sqrt{\frac{L}{10^{45}\,\mathrm{erg\,s^{-1}}}}\left(\frac{1500\,\mathrm{K}}{T_{\mathrm{sub}}}\right)^{2.6}\,\mathrm{pc} \tag{1.3}$$

for a central engine of bolometric luminosity L and dust sublimation temperature T_{sub}. Since some dusty clumps at radii larger than the inner radius of the torus ($\mathrm{R_i}$ in Figure 1.5) will be exposed to the central engine unobscured while other clumps will be blocked by clumps at smaller radii, this model can explain observations of co-spatial 200 K and $>$ 800 K dust (Schartmann et al., 2005). The remaining parameters Nenkova et al. (2008a) and Nenkova et al. (2008b) include in their torus model are the optical depth of a single torus clump at 550 nm τ_V (assumed to be the same for all clumps), the mean number of clouds along a radial equatorial line N_0, the radial extent of the torus in units of the dust sublimation Y (equivalent to R_o/R_i in Figure 1.5), the inclination of the torus with respect to the line of sight i (defined such that 0° is pole-on), the angular scale height of the torus σ, and the power law index of the radial distribution of clumps q. From these they show how to calculate the half-opening angle of the torus (Θ in Figure 1.5) and the probability of a photon getting through the torus without interacting (called the "escape probability").

1.3.2 Two-mode AGN model

The unification models described in Section 1.3 have fallen out of favour with a two-mode model (see Antonucci (2012) for a review) being dominant now. The high excitation mode generally resembles the old unification models, these are what Antonucci (2012) calls "thermal AGN" and are typically emitting with Eddington ratios $L_{\mathrm{AGN}}/L_{\mathrm{Edd}}$ of $1-10\%$ (Best & Heckman, 2012). The Eddington ratio represents the luminosity as a proportion of the Ed-

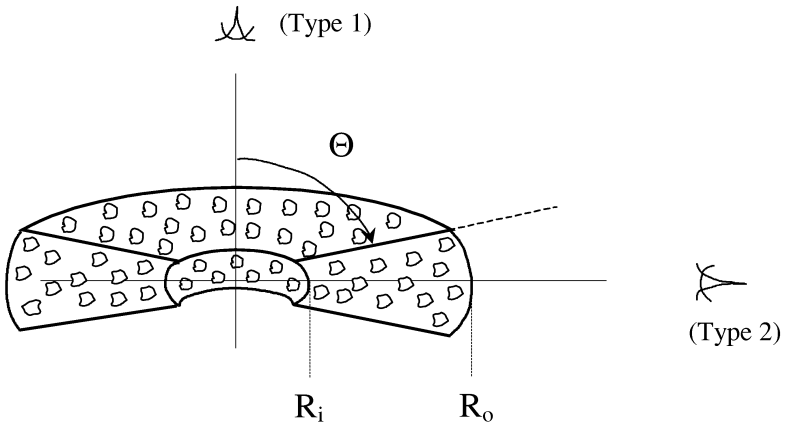

Figure 1.5 Diagram of an obscuring clumpy torus by Nenkova et al. (2002). Θ is the half-opening angle of the torus and R_i and R_o refer to the inner and outer radii of the torus respectively. The lines of sight describe the viewing angles required to see a Seyfert AGN of the listed type.

digton luminosity $L_{\rm Edd}$ which is the maximum luminosity at which a structure of a given size and mass can radiate while remaining stable. Carroll & Ostlie (1996) gives the Eddington luminosity of a black hole with mass $M_{\rm BH}$ as

$$L_{\rm Edd} = \frac{4\pi G c M_{\rm BH}}{\sigma_T} \simeq 1.2 \times 10^{38} \left(\frac{M_{\rm BH}}{M_\odot} \right) {\rm erg\,s^{-1}}, \tag{1.4}$$

where G is the gravitational constant, c is the speed of light in vacuum, and $\sigma_{\rm T}$ is the Thomson scattering cross-section. The low excitation mode, or "'nonthermal AGN" features an advection dominated accretion flow (ADAF) in which the accreting material forms a hot corona around the central SMBH and the majority of energy outflow from the central engine takes the form of kinetic energy in a radio-bright relativistic jet. Nonthermal AGN are far less radiatively efficient than thermal AGN and typically emit at $< 1\%$ of their Eddington rate (Best & Heckman, 2012). Some papers, particularly those focused on radio such as Padovani (2016) and Gendre et al. (2013), use the terms "jet-mode" to refer to low-excitation sources and "radiative mode" to refer to high-excitation sources. radio galaxies in the high-excitation mode (high-excitation radio galaxies or HERGs) should show the

evidence of thermal emission from a warm dusty torus around $\sim 10 - 20\,\mu$m and radio galaxies in the low-excitation mode (low-excitation radio galaxies or LERGs) should show no or weak thermal emission in that waveband, being instead dominated by emission from the host galaxy or a synchrotron-emitting jet.

An optically thin ADAF is one of four solutions to the hydrodynamic equations of viscous differentially-rotating flows described by Narayan et al. (1998): a thin-disk solution (Shakura & Sunyaev, 1973; Lynden-Bell & Pringle, 1974) believed to power high-excitation AGN, a thermally unstable two-temperature plasma (Shapiro et al., 1976), an optically thick ADAF (Katz, 1977) which requires super-Eddington accretion rates, and an optically thin ADAF (Ichimaru, 1977) which dominates for AGN luminosities far below Eddington luminosity. In an optically thin ADAF accreting gas cannot cool efficiently within an accretion time due to its low density and so all its viscous energy is stored as thermal energy and advected onto the black hole. Note that this heating preferentially heats ions over neutrals. An optically thin ADAF appears as a synchrotron spectrum in radio, an inverse-Compton spectrum in optical, a bremsstrahlung spectrum in X-rays and a pion-decay spectrum in γ-rays. For more on the multi-wavelength properties of an optically thin ADAF see Figure 5 of Narayan et al. (1998) which we include as Figure 1.6.

The change between the two modes is typically thought to be dictated by the environment. Allen et al. (2006) found that spherically symmetric accretion onto a point mass onto the SMBH from the hot X-ray emitting IGM is sufficient to power the AGN jets in several nearby low-excitation sources. This accretion, called Bondi accretion (Bondi, 1952), is subsonic until a critical "Bondi radius" at which point the flow becomes supersonic and more closely resembles free-falling gas. Following up on the work of Allen et al. (2006), Hardcastle et al. (2007) found that Bondi accretion of hot X-ray gas onto the SMBH can power all low-excitation sources and they further attribute high excitation radio AGN to accretion of cold gas from unrelated processes (such as galaxy mergers) onto the SMBH. This has ramifications in the context of AGN feedback and the cooling flow problem which

are beyond the scope of this thesis.

Part of the appeal of this two-mode model is that Elitzur & Shlosman (2006) found that, in their hydromagnetic wind models, central engines with a bolometric luminosity of less than $\sim 10^{42}\,\mathrm{erg\,s^{-1}}$ cannot sustain the mass outflow rates of material needed to maintain a dusty torus. This model retains the explanations for high-luminosity AGN from the unification models and also accounts for low-luminosity AGN at the cost of a well-motivated increase in complexity.

In a study conceptually similar to ours, González-Martín et al. (2015) searched for AGN obscuration in *Spitzer*/IRS (see Section 2.2.2) spectra and *Chandra* photometry of a sample of low-ionization nuclear emission region (LINER) AGN. They found that the dusty torus present in brighter sources disappeared below bolometric luminosities $L_{\mathrm{bol}} \simeq 10^{42}\,\mathrm{erg\,s^{-1}}$, consistent with Elitzur & Shlosman (2006), and that the MIR spectra of such sources is dominated by host, jet, and/or ADAF emission.

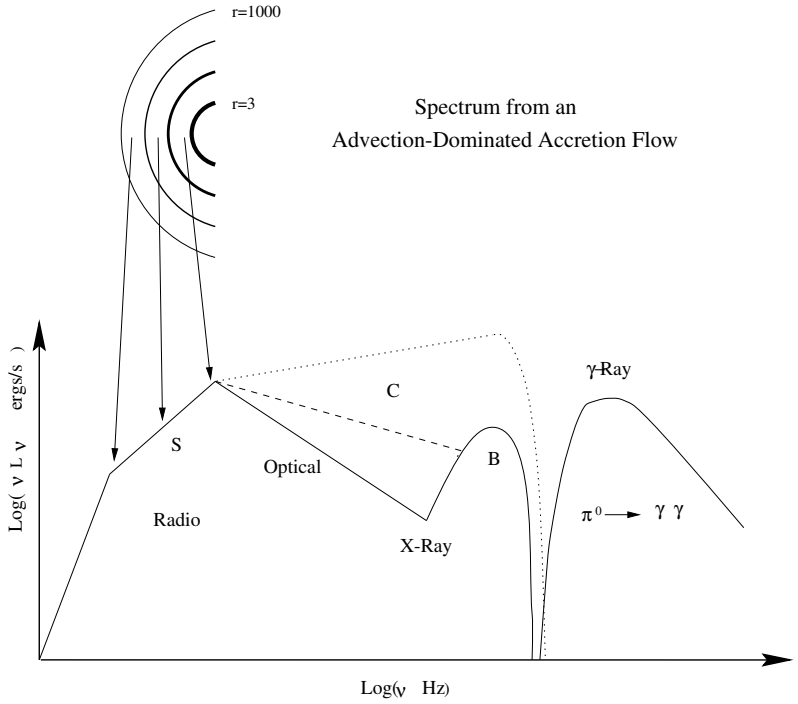

Figure 1.6 Sketch of the multi-wavelength emission spectrum of an optically thin ADAF by Narayan et al. (1998). 'S', 'C', and 'B' represent synchrotron, inverse-Compton, and thermal Bremsstrahlung spectra, respectively.

It is worth noting that Quataert et al. (1999) found that they could explain the spectral energy distributions of two low-luminosity AGN, M 81 and NGC 4579, using a hybrid "truncated thin-disk" model also mentioned by Narayan et al. (1998) in which an accretion flow of $\dot{M} \sim 0.01 - 0.03\,\dot{M}_{\rm Edd}$ forms an outer thin disk which blends into an optically thin ADAF at $\sim 100\,R_{\rm S}$. We show a diagram by Nemmen et al. (2014) of this model in Figure 1.7. Their assumed black hole masses were inconsistent with later measurements but Xu & Cao (2009) found that a similar model would still work, this time with $\dot{M} \sim 2.5 \times 10^{-4}\,\dot{M}_{\rm Edd}$, suggesting the likelihood that there exist at least some hybrid sources contrary to the usual dichotomy. Xu & Cao (2009) also observed X-ray lines characteristic of the transition between the 10^{9-10} K ADAF and 10^{4-5} K outer thin disk which are consistent with Keplerian motion at $\sim 100\,R_{\rm S}$. These X-ray observations provide further support for their model in these particular sources.

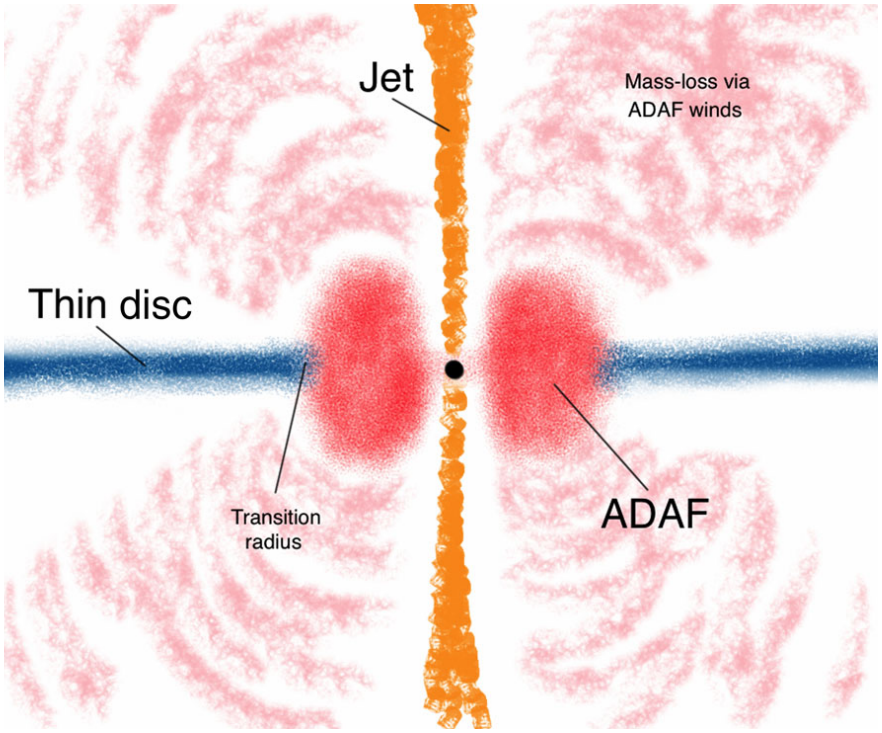

Figure 1.7 Simple diagram by Nemmen et al. (2014) of the hybrid model described by Quataert et al. (1999) and Xu & Cao (2009).

1.4 Existing evidence in FR-I radio galaxies

How do FR-I radio galaxies fit into the AGN models described in Section 1.3? This boils down to two separate but related questions:

1. What is the nature of the accretion structure which is powering the radio jet?

2. Is the light from the central engine being obscured and, if so, how?

These are related because if FR-Is are powered by an accretion structure with a high intrinsic optical luminosity such as a Keplerian thin disk then the central engine must be obscured in order to match observations. In Sections 1.4.1 and 1.4.2 we review the literature on each of the above questions in turn.

1.4.1 Accretion structure

Baum et al. (1995) put forward the possibility that FR-I radio galaxies are intrinsically distinct from FR-II radio galaxies based in part on the work of Rees et al. (1982). They claim that FR-I radio galaxies are produced when the central engine is fed at a lower accretion rate and more of the output power of the central engine is emitted in the form of jet kinetic energy. They additionally suggest the possibility that the source of the differences between the FR-I and FR-II morphology may be due to a higher rate of SMBH spin in FR-II sources than in FR-I sources. As an early paper, the distinction between HERGs and LERGs was not considered.

Buttiglione et al. (2010) use emission line measurements of a homogeneous 92% complete optical sample of 3CR radio galaxies at $z < 0.3$ by Buttiglione et al. (2009) to compare HERGs and LERGs (distinguished based on narrow emission line ratios). They find that all the HERGs in their sample have FR-II morphology and 178 MHz radio line luminosities of $> 6.31 \times 10^{25}$ W whereas LERGs cover 178 MHz line luminosities from $\sim 5 \times 10^{23} - 2 \times 10^{28}$ W and show both FR-I and FR-II morphologies. They conclude that accretion rate alone

cannot explain the difference between HERGs and LERGs and they instead favour two distinct accretion modes which depend on the environment around the AGN similar to that in Section 1.3.2.

A large-scale sample of 18286 radio AGN by Best & Heckman (2012) put the critical radio luminosity at which HERGs begin to dominate the statistics at $L_{1.4\,\mathrm{GHz}} \sim 10^{26}\,\mathrm{W\,Hz^{-1}}$. This critical luminosity is not a hard cut-off, however, and there are HERGs with radio powers of less than that especially in galaxies with relatively low stellar and black hole masses.

Gendre et al. (2013) looked for relations between extended radio morphology and accretion mode in radio galaxies. They find no correlation between the two properties and that instead the extended radio morphology is dependent only on jet power and the interactions of said jet with the environment. They additionally find that FR-I radio galaxies are preferentially found in high density environments which is consistent with FR-I jets being disrupted by interactions with the environment. They note, however, that they found significant overlap in environment between FR-I and FR-II radio galaxies and they found no clear factor behind the separation. Even the combined effects of variation in radio luminosity, accretion mode, large-scale environment, and the optical luminosity of the host galaxy is insufficient to explain the large scale morphology.

Ineson et al. (2015) looked at the environment around radio galaxies and found evidence for a correlation between cluster X-ray luminosity and LERG radio luminosity but none between cluster X-ray luminosity and HERG radio luminosity. They attribute this to HERGs being fuelled by accretion of cold gas (from mergers with small gas-rich galaxies) in the form of a radiatively efficient accretion disk while LERGs are fuelled by hot phase accretion from the hot intracluster medium. This is consistent with the two-mode model described in Section 1.3.2. They additionally compare the radio galaxy populations at $z \sim 0.1$ and $z \sim 0.5$ and find evidence of evolution in the HERG populations at the two epochs but not between the LERG populations and found similar results for the evolution of the environments i.e., the environments around HERGs show tentative evidence of evolution while those around

LERGs do not.

1.4.2 Obscuration

Chiaberge et al. (1999) detected the central core component in 85% of *Hubble* Space Telescope observations of FR-I radio galaxies and so put an upper limit on the covering fraction of any obscuring torus with the caveat that the base of an optical jet may appear as an alternate source of optical continuum emission.

Whysong & Antonucci (2004) found that the MIR core component of M 87 is dominated by synchrotron emission from the base of its relativistic jet and Perlman et al. (2007) put further limits on a a warm obscuring torus in M 87 which effectively rule it out. van der Wolk et al. (2010a) found no evidence for warm dust tori in any of the eight FR-I sources in their observations from the Very Large Telescope's VLT Imager and Spectrometer for the Mid Infrared. Note that one of the FR-I sources in the van der Wolk et al. (2010a) sample is 3c 270, which is also in our sample.

In *HST* images of the optical nuclei of a sample of 54 FR-I and 55 FR-II radio galaxies at $z < 0.3$, Kharb & Shastri (2004) found that the optical emission in these sources is primarily non-thermal emission from a relativistic jet. They also found no significant contribution from a thermal accretion disk in FR-I or narrow-line emitting FR-II but there may be significant emission from an accretion disk in broad-line emitting FR-II. They additionally found that the luminosity of the optical nuclei in FR-I radio galaxies show strong dependence on the radio core prominence R_c, which is a common statistical indicator of orientation, and from this they conclude that their results a consistent with the lack of a torus in FR-I radio galaxies.

In UV spectra of 31 3C and Parkes radio galaxies Zirbel & Baum (2003) found no strong UV continuum source in narrow-line FR-II radio galaxies and found that FR-I radio galaxies only show a strong UV continuum component in sources with a prominent optical jet. They attribute the UV emission in these FR-I radio galaxies to those sources being at a critical

angle in which some but not all nuclear emission is blocked.

Overall, recent studies favour the two-mode models (see Section 1.3.2) in which some but not all FR-I radio galaxies have some sort of obscuring material around their central engines and the remainder have central engines which are too dim in IR to distinguish from the emission of their hosts. These dim central engines will still produce jets which may appear in the IR as a synchrotron spectrum. This is likely due to environmental factors relating to the source of the accreting material. The structure of this obscuring material is, however, not necessarily a torus like that described by Nenkova et al. (2002, 2008a,b).

1.5 The big picture

What powers the radio emission in FR-I radio galaxies and how do they fit into the broader picture of AGN? To answer this we search for the spectral signature of warm obscuring dust, as predicted by AGN unification models, in the infrared spectra of ten nearby FR-I radio galaxies from a well-studied sample (see Chapter 3). Our primary focus is on continuum emission in the band covered by the *Spitzer* Space Telescope's Infrared Spectrograph. We analyse archival spectra using a pair of specialised fitting codes based on Markov chain Monte Carlo techniques.

Chapter 2

Instruments and Surveys

2.1 Two Micron All Sky Survey

Two Micron All Sky Survey (2MASS), as described by Skrutskie et al. (2006), was a J, H, and K-band survey covering 99.998% of the sky performed between June 1997 and February 2001. Observations were performed by two 1.3 m telescopes in Mount Hopkins, Arizona, USA and in Cerro Tololo, Chile.

The data products of the survey consist of 25.4 TB of raw data released as 4.1 million compressed FITS images, 471 million point source extractions, and 1.6 million extended source extractions. The point source extractions used an instantaneous point-spread function width of 4" with sky background subtraction in an annulus with inner radius of 14" and an outer radius of 20". We list the central wavelength, bandwidth, and zero magnitude flux density for each filter in Table 2.1 along with the point source detection level. Extended source extractions used a fiducial ellipse determined by the 20 mag/arcsec^2 isophote for each source. We list the semi-major axes for these ellipses in Table 2.2. Both sets of extractions are described in more detail by Cutri et al. (2003).

For 2MASS data, as for *Spitzer*/IRAC in Section 2.2.1, we use point source extractions of our target AGN as a lower bound and extended source extractions as an upper bound. This

Band	Central Wavelength (μm)	Bandwidth (μm)	10σ Detection Level (mag, Point Source)	0 mag flux density (Jy)
J	1.235 ± 0.006	0.162 ± 0.001	15.8	1594 ± 27.8
H	1.662 ± 0.009	0.251 ± 0.002	15.1	1024 ± 20.0
K_s	2.159 ± 0.011	0.262 ± 0.002	14.3	666.7 ± 12.6

Table 2.1: Band sensitivity and detection information for 2MASS. Detection level from Skrutskie et al. (2006) and everything else from Cohen et al. (2003).

is because the nucleus itself should be an unresolved point source whereas emission from the host galaxy will dominate on wider scales. Recall that we list the band information and zero magnitude flux for each 2MASS filter in Table 2.1. 3C 66B is not in the 2MASS Extended Source Catalogue so we replaced it with extended source photometry by Lilly et al. (1985).

Source	Semi-major axis (arcsec)	J (ap. mag)	H (ap. mag)	K_s (ap. mag)
NGC 315	65.6	9.044 ± 0.012	8.301 ± 0.016	8.050 ± 0.017
3C 31	49.9	9.619 ± 0.014	8.894 ± 0.018	8.599 ± 0.023
NGC 541	37.8	10.462 ± 0.017	9.772 ± 0.026	9.484 ± 0.034
3C 66B*	-	-	-	-
NGC 3801	49.9	9.999 ± 0.013	9.264 ± 0.020	9.004 ± 0.020
NGC 3862	30.7	10.707 ± 0.021	9.976 ± 0.025	9.720 ± 0.034
3C 270	79.9	8.355 ± 0.016	7.652 ± 0.016	7.407 ± 0.017
M 84	115.0	7.260 ± 0.015	6.587 ± 0.016	6.222 ± 0.023
NGC 7052	61.9	9.628 ± 0.012	8.934 ± 0.015	8.653 ± 0.020

Table 2.2: 2MASS extended source extraction information. Semi-major axes refer to the K_s-band 20 mag/arcsec^2 isophotal fiducial ellipse used in the extraction. *not in extended source catalogue

2.2 The *Spitzer* Space Telescope

The *Spitzer* Space Telescope was launched on August 25, 2003 as part of NASA's Great Observatories program. The telescope has three focal plane instruments, the Infrared Array Camera (IRAC), the Infrared Spectrometer (IRS), and the Multiband Imaging Photometer

for *Spitzer* (MIPS). We describe these instruments individually in Sections 2.2.1-2.2.3 and Werner et al. (2004) describes the telescope as a whole in detail.

2.2.1 Infrared Array Camera

Spitzer/IRAC, as described by Fazio et al. (2004), is a cryogenic ($\sim$ 1.2 K) four-channel IR imager. We list the wavelength response characteristics and full width at half maximum (FWHM) of the point-spread function for each channel in Table 2.3.

Channel	Isophotal wavelength* (μm)	Bandpass (μm)	Mean FWHM (arcsec)
1	3.550	3.19-3.94	1.66
2	4.493	4.00-5.02	1.72
3	5.731	4.98-6.41	1.88
4	7.872	6.45-9.34	1.98

Table 2.3: IRAC instrument specifications. Based on the work of Werner et al. (2004) and Fazio et al. (2004). *see definition by Fazio et al. (2004) — in short, the isophotal wavelength is the wavelength assigned to the flux density of the broadband mesurement

Our *Spitzer*/IRAC data are archival images from the *Spitzer* Heritage Archive. We list the astronomical observation request key (AORKEY) for each source in Table 2.4. For each source we performed a point-spread function fit to provide a lower bound to the flux and an aperture extraction with the same 4" aperture as 2MASS as an upper bound. Both extractions were centered on the CASSIS source centroid. For this purpose we used the Overlap, Mosaicking, and Multiframe aperture extraction of the Mosaicking and Point Source Extraction (MOPEX) software by Makovoz & Marleau (2005). We show the images and extraction locations for each source in Appendix C. All ten sources had usable images for channel 2 (effective wavelength $\lambda_{eff} = 4.493\,\mu$m) and all but M 84 had usable images for channel 1 ($\lambda_{eff} = 3.550\,\mu$m). We list the IRAC photometry in Tables 2.7.

Source	IRAC AOR	MIPS AOR
NGC 315	19169024	4427776
3C 31	14805760	21681920/4691968*
NGC 541	19170048	4345088
3C 66B	14806016	10927360
NGC 3801	19170304	19168512
NGC 3862	14807552	4692480
3C 270	14807808	4692736
M 84	4671744	4692992
NGC 7052	18257664	19168768

Table 2.4: *Spitzer* AORKEYs for ancillary data used in our analysis. M 87 photometry came from a different data set (see Table 2.5) and so that object is excluded from this table. *Due to an issue with channel 1 in 4691968, we use the channel 1 data from 21681920 for our analysis of 3C 31.

Wavelength (μm)	Flux (mJy)	Aperture (arcsec)	Limit	Reference
1.25	$227. \pm 3.$	14	Upper	Skrutskie et al. (2006)
1.25	$78. \pm 2.$	7.5	Lower	Frogel et al. (1978)
1.64	$284. \pm 4.$	14	Upper	Skrutskie et al. (2006)
1.65	$98. \pm 3.$	7.5	Lower	Frogel et al. (1978)
2.17	$237. \pm 3.$	14	Upper	Skrutskie et al. (2006)
2.20	$77. \pm 2.$	7.5	Lower	Frogel et al. (1978)
4.49	24.2	5.8	Lower	Teplitz et al. (2012)
71.3	480 ± 40	18	Upper	Temi et al. (2009)
156	580 ± 10	40	Upper	Shi et al. (2007)
250	900 ± 200	18	Upper	Baes et al. (2010)
350	1000 ± 300	25	Upper	Baes et al. (2010)
500	1400 ± 400	36	Upper	Baes et al. (2010)

Table 2.5: Ancillary photometry data for M 87.

Source	Channel	Limit	IRAC flux (mJy)	MIPS flux (mJy)	SPIRE flux (mJy)
NGC 315	1	Upper	23.20 ± 0.01	-	-
		Lower	10.02 ± 0.02	-	-
	2	Upper	14.93 ± 0.01	$342. \pm 6.$	-
		Lower	7.65 ± 0.02	-	-
	3	Upper	-	$471. \pm 3.$	-
3C 31	1	Upper	21.99	-	$954. \pm 5.$
		Lower	8.69 ± 0.01	-	-
	2	Upper	13.45	$439. \pm 2.$	$423. \pm 5.$
		Lower	5.046	-	-
	3	Upper	-	$931. \pm 5.$	$170. \pm 6.$
NGC 541	1	Upper	12.26 ± 0.01	-	80 ± 10
		Lower	5.87 ± 0.01	-	-
	2	Upper	7.437 ± 0.006	$125. \pm 3.$	40 ± 10
		Lower	3.56 ± 0.01	-	-
	3	Upper	-	$82. \pm 3.$	60 ± 60
3C 66B	1	Upper	10.72	-	-
		Lower	4.70 ± 0.05	-	-
	2	Upper	6.545 ± 0.003	-	-
		Lower	2.21 ± 0.004	-	-
NGC 3801	1	Upper	15.79	-	-
		Lower	8.40 ± 0.01	-	-
	2	Upper	9.417 ± 0.005	-	-
		Lower	4.787 ± 0.008	-	-
	3	Upper	-	$1154. \pm 3.$	-

Table 2.6: Ancillary photometry for first five sources sorted by right ascension. Continued for four out of five remaining sources in Table 2.6.

Source	Channel	Limit	IRAC (mJy)	MIPS (mJy)	SPIRE (mJy)
NGC 3862	1	Upper	14.09	-	-
		Lower	7.838 ± 0.006	-	-
	2	Upper	9.265 ± 0.003	$192. \pm 3.$	-
		Lower	5.878 ± 0.006	-	-
	3	Upper	-	$233. \pm 2.$	-
3C 270	1	Upper	43.32 ± 0.02	-	200 ± 10
		Lower	17.57 ± 0.02	-	-
	2	Upper	25.45 ± 0.01	144.4 ± 0.7	$200 \pm 20.$
		Lower	10.50 ± 0.01	-	-
	3	Upper	-	$155. \pm 2.$	200 ± 20
M 84	1	Upper	-	-	250 ± 20
	2	Upper	41.53 ± 0.02	-	150 ± 20
		Lower	21.49 ± 0.02	-	-
	3	Upper	-	-	140 ± 20
NGC 7052	1	Upper	20.12 ± 0.01	-	-
		Lower	8.38 ± 0.01	-	-
	2	Upper	12.07	$400. \pm 7.$	-
		Lower	5.23 ± 0.01	-	-
	3	Upper	-	$812. \pm 5.$	-

Table 2.7: Ancillary photometry for all remaining sources not included in Table 2.6 except for M 87. We show the ancillary photometry for M 87 in Table 2.5.

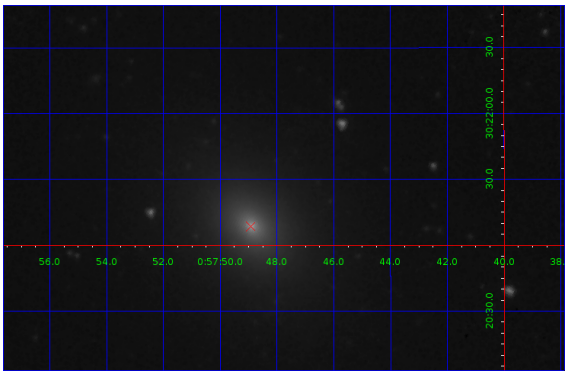

(a) NGC 315

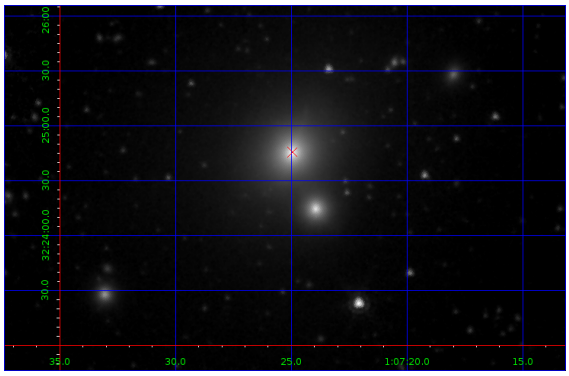

(b) 3C 31

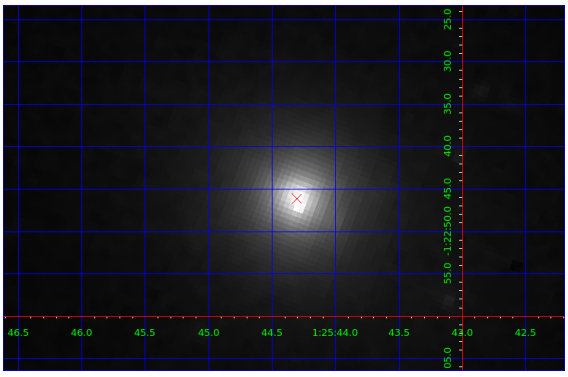

(c) NGC 541

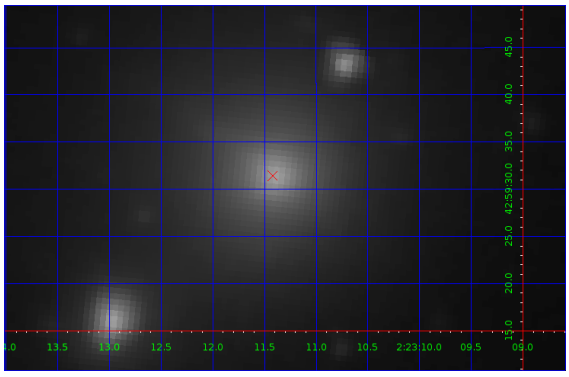

(d) 3C 66B

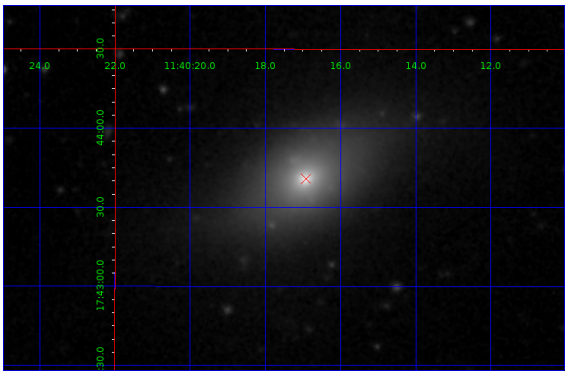

(e) NGC 3801

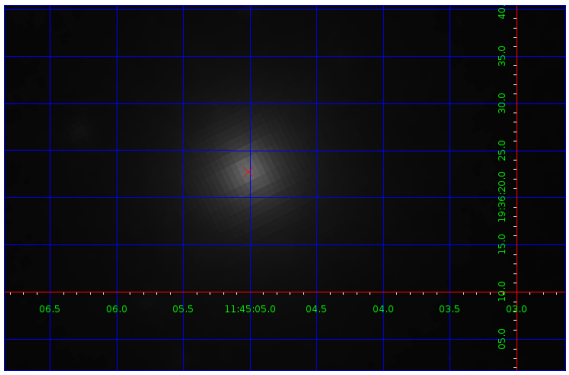

(f) NGC 3862

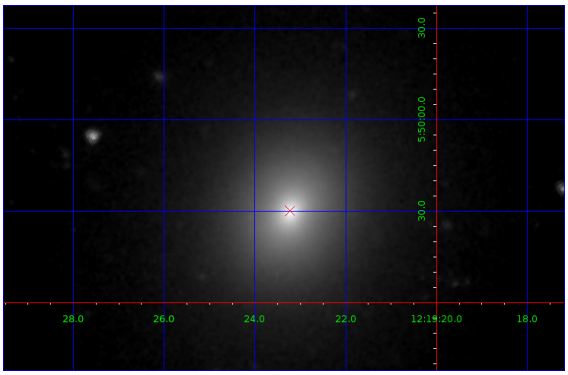

(g) 3C 270

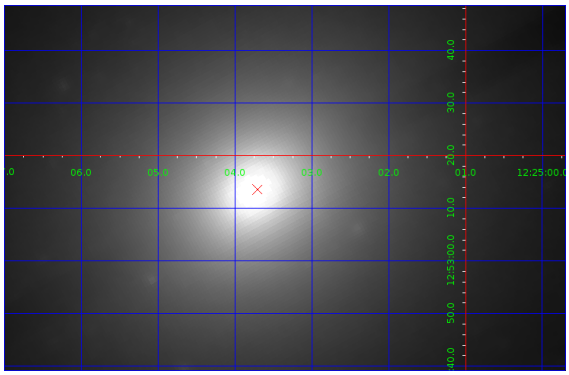

(h) M 84

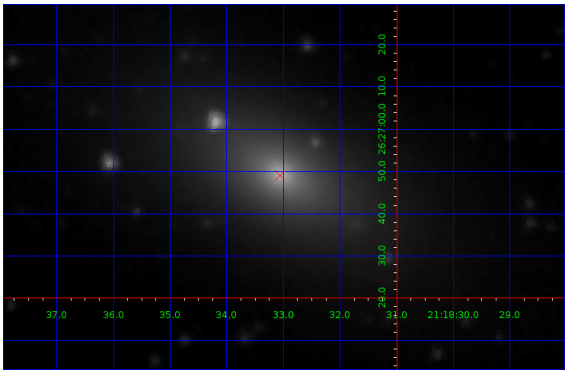

(j) NGC 7052

Figure 2.1 *Spitzer*/IRAC Channel 2 images with extraction locations overlaid on each source (red x). Overlays added in SAOImage DS9.

2.2.2 Infrared Spectrometer

Houck et al. (2004) describes the Infrared Spectrometer (IRS) aboard *Spitzer*. IRS has four spectrograph modules with total wavelength coverage from 5.3-38 μm. We use data from the Short-Low (SL) and Long-Low (LL) modules in this thesis, each of which have spectral resolution $R = \lambda/\Delta\lambda \approx 90$. We list more specific parameters in Table 2.8.

Module	Wavelength band (μm)	$\lambda/\Delta\lambda$	Pixel scale (arcsec)	Detector composition
Short-Low (SL)	5.2-14.5	64-128	1.8	Si:As
Long-Low (LL)	14.0-38.0	64-128	5.1	Si:Sb
Short-High (SH)	9.9-19.6	~ 600	2.3	Si:As
Long-High (LH)	18.7-37.2	~ 600	4.5	Si:Sb

Table 2.8: IRS instrument specifications. All information by Houck et al. (2004).

All of our IRS spectra are tapered column extractions from the Combined Atlas of Sources with *Spitzer*/IRS Spectra (CASSIS, formerly the Cornell Atlas of Spitzer/IRS Sources) by Lebouteiller et al. (2011). As of 2011 the CASSIS low-resolution catalogue contained more than 11,000 distinct sources extracted using an algorithm within *Spitzer*'s Spectroscopic Modeling Analysis and Reduction Tool (Higdon et al., 2004).

2.2.3 Multiband Imaging Photometer for *Spitzer*

Rieke et al. (2004) describes the Multiband Imaging Photometer for *Spitzer* (MIPS). MIPS provides *Spitzer*'s long-wavelength capability, with imaging bands at 24, 70, and 160 μm. These imaging bands have telescope-limited spatial resolutions of 6", 18", and 40" respectively. MIPS also is capable of performing far-infrared spectrometry between wavelengths of 52 and 100 μm with spectral resolution of about 7%. However, there are unfortunately no MIPS spectra for the sources in our sample.

Similarly to our *Spitzer*/IRAC data, our *Spitzer*/MIPS data are archival images from the *Spitzer* Heritage Archive for which we list the AORKEY in Table 2.4. The photometry

extraction pipeline for MIPS in MOPEX is also similar to that for IRAC. However, the aperture extraction module in MOPEX failed so we used the point-source flux only. The point-spread function for the 70 and 160 μ bands is wider than for IRS so the point source flux provided an upper bound on the far-infrared flux of our fits. We show the images and extraction locations for each source in Appendix D. Only M 84 had no usable MIPS photometry and NGC 3801 had no usable 70 μm data.

2.3 *Herschel* Spectral and Photometric Imaging Receiver

The Spectral and Photometric Imaging Receiver aboard *Herschel*, as described by Griffin et al. (2007), is a far-infrared/sub-mm imaging photometer with imaging bands at wavelengths of 250, 350, and 500 μm. These imagers are cryogenic ($\sim$ 0.3 K) feedhorn-coupled bolometers and have FWHM beam widths of 18", 25", and 36" respectively. SPIRE also has an imaging Fourier transform spectrometer with sensitivity from 194-672 μm and spectral resolution $\lambda/\Delta\lambda$ from 1200 (short wavelengths) to 300 (long wavelengths). As with *Spitzer*/MIPS, only photometry observations are available of any of our sample galaxies.

We used archival *Herschel*/SPIRE point source extractions from the SPIRE Point Source Catalogue by Marton et al. (2016). We list the observation identification number (obsid) for the two sources in Table 2.4. The SPIRE Point Source Catalogue reports fluxes and not magnitudes so no further processing is necessary.

Chapter 3

Sample

3.1 Sample description

Our sample, for which we list basic information in Table 3.1, is the subset for which there exists low resolution CASSIS spectra (Lebouteiller et al. (2011), see Section 2.2.2) from a list compiled by Verdoes Kleijn et al. (1999). This sample consists of all nearby ($v_r < 7000\,\mathrm{km\,s^{-1}}$) radio galaxies in Nilson (1973)'s Uppsala General Catalogue (UGC) with declination $-5^\circ < \delta < 70^\circ$ that are larger than 10" at 3σ in VLA A Array maps and brighter than 150 mJy at 1400 MHz. The Verdoes Kleijn et al. (1999) sample was extracted from a catalogue of 176 radio galaxies Condon & Broderick (1988) constructed through position coincidence between their Green Bank 1400 MHz sky maps (Condon & Broderick, 1985, 1986, 1988) and the UGC. Condon & Broderick (1988) distinguished between starburt sources and AGN-powered "monsters" based on radio morphology, infrared-radio parameter $\log(S_{60\,\mu\mathrm{m}}/S_{1400\,\mathrm{MHz}})$, and infrared spectral index. Xu et al. (1999) provides a detailed description of this sample's radio properties.

UGC Number	NGC Number	Alternate Name	RA (J2000.0)	Dec (J2000.0)	Redshift
597	315		00h 57m 48.9s	+30d 21m 09s	0.016485
689	383	3C 31	01h 07m 24.9s	+32d 24m 45s	0.017005
1004	541		01h 25m 44.3s	-01d 22m 46s	0.018086
1841		3C 66B	02h 23m 11.4s	+42d 59m 31s	0.021258
6635	3801		11h 40m 16.9s	+17d 43m 41s	0.011064
6723	3862	3C 264	11h 45m 05.0s	+19d 36m 23s	0.021718
7360	4261	3C 270	12h 19m 23.2s	+05d 49m 31s	0.007378
7494	4374	M 84, 3C 272.1	12h 25m 03.7s	+12d 53m 13s	0.003392
7654	4486	M 87, 3C 274	12h 30m 49.4s	+12d 23m 28s	0.004283
11718	7052		21h 18m 33.0s	+26d 26m 49s	0.015584

Table 3.1: Basic sample information. Redshifts, Right Ascension (RA) and Declination (Dec) by Anderson & Ulvestad (2005) and accessed from the NASA/IPAC Extragalactic Database.

Source	Redshift	Luminosity Distance (Mpc)	Scale (kpc/arcsec)
NGC 315	0.016485	71.50	0.3466
3C 31	0.017005	73.78	0.3577
NGC 541	0.018086	78.54	0.3808
3C 66B	0.021258	92.53	0.4486
NGC 3801	0.011064	47.79	0.2317
NGC 3862	0.021718	94.57	0.4585
3C 270	0.007378	31.78	0.1541
M 84	0.003392	14.56	0.07059
M 87	0.004283	18.40	0.08921
NGC 7052	0.015584	76.54	0.3711

Table 3.2: Distance information for sample. We calculated luminosity distances from redshifts using conversion software by the Astropy Collaboration et al. (2013) for a flat-Λ cold dark matter cosmology with Hubble constant $H_0 = 70\,\mathrm{km\,s^{-1}}$ and an energy density composition of 30% ordinary baryonic matter and dark matter ($\Omega_\mathrm{M} = 0.3$) and 70% dark energy ($\Omega_\Lambda = 0.7$).

3.2 Previous studies on this sample

The original paper by Verdoes Kleijn et al. (1999) looked at broad- and narrow-band images of 19 out of the 21 radio galaxies in its sample from the Wide-Field Planetary Camera 2 aboard *HST*. They found that most but not all of these galaxies have shallow cores and they detected dust in all but two (NGC 741 and NGC 2892, neither of which are in our sub-sample) of the 19. Their analysis of the dust morphologies concludes that there are intrinsic differences between dust lanes and dust disks. In the second paper in the series, Kleijn et al. (2002) searched for relations between radio and optical continua and optical Hα + [NII] emission. They confirmed a previously noted linear relation between optical and radio core emission and showed that both correlate to Hα + [NII]. The tight correlations constrain the bulk Lorentz factor of the jet to $\gamma \sim 2 - 5$ for a continuous jet or $\gamma \lesssim 2$ for a jet comprised of discrete blobs. They attribute both the radio and optical continua in the core to synchrotron emission from the inner jet.

Xu et al. (2000) used pc-scale data from the Very Large Baseline Array and kpc-scale data from the Very Large Array to look at jets in 17 radio galaxies from the UGC FR-I sample. They found that jet-counterjet brightness ratios decrease with distance from the central source, which they attribute to the jets decelerating with distance from the source resulting in decreased Doppler boosting. Additionally, they found that the jet luminosity per unit length decreased with the square of distance from the central source which they attribute to adiabatic expansion of the jet material into the surrounding medium.

Noel-Storr et al. (2003) looked at mid-resolution spectra of emission-line-emitting gas in FR-I nuclei from the Space Telescope Imaging Spectrograph aboard *HST*. They found that the gas appears to be rotating in 67% of the sample nuclei. They also found that 62% of spectral fits benefit from the inclusion of a broad component with a mean velocity dispersion of $1349 \pm 345\,\mathrm{km\,s^{-1}}$. These broad components were, on average, redshifted relative to the narrow lines by $486 \pm 443\,\mathrm{km\,s^{-1}}$. Noel-Storr et al. (2007) followed up on this with further analysis of the gas kinematics in the same spectra. They found that point-to-point variations

in the kinematics are largest perpendicular to disks and in nuclei with less organized motion. They also found that the gas velocity dispersion is not distributed as a function of inclination and that the gas velocity dispersion is closely related to the stellar velocity dispersion. Overall they note that their results digress significantly from the smooth Keplerian thin-disk model.

Verdoes Kleijn & de Zeeuw (2005) compared dust distributions and their relation to radio jet orientation in the cores of the UGC FR-I sample to two comparison samples. The first comparison sample is a "FR sample" containing 47 FR-I and FR-II galaxies and the second is a sample of 52 quiescent early-type UGC galaxies. They detected dust at a higher rate in active galaxies than in quiescent galaxies and they found that when present the dust distributions in radio galaxies are more elliptical than those in quiescent galaxies. They also found that the size and orientation of these dust ellipses is unconnected to activity but rather they are preferentially aligned with the host galaxy's major axis in all samples and conclude that the ellipses are likely thin circular disks viewed from various different angles. Dust lanes tend to be aligned with the host's minor axis on scales smaller than $\sim 1\,\mathrm{kpc}$ and show no alignment preference on larger scales. The radio jets do not seem to show any preferential alignment with the host's major axis on their own but they tend to be perpendicular to dust lanes.

Capetti et al. (2005) looked at emission line regions in the FR-I UGC sample and 33 radio galaxies in the 3C catalogue which, accounting for overlap between the two samples, is a total of 47 galaxies. They used optical narrow band imaging from *HST*. They found a strong correlation between line and continuum emission meaning that the optical cores can be directly attributed to the source of ionizing photons. They propose that the emission line region may be a pc-scale high-filling-factor structure. This "compact emission line region" could have a mass as small as $10 - 10^3\,\mathrm{M}_\odot$ and the broad line region contained within would have a total mass of $< 10^{-2}\,\mathrm{M}_\odot$ and be gas-poor.

The most recent study on the UGC FR-I sample was by Kharb et al. (2012). They looked at 1.6 and 5 GHz images of 19 out of the 21 radio galaxies from the Very Large

Baseline Array as well as archival *Chandra* X-ray images of 14 sources and new *Chandra* X-ray images of UGC 408. They detected polarized emission in the jets of seven sources and in the core of M 87. They inferred that the magnetic field in these jets is primarily aligned along the jet direction and which they proposed could be due to either magnetic field "shearing" from jet-medium interaction or the presence of helical magnetic fields. They found that the jet peak intensity decreases with distance from the central source d according to $I_\nu \propto d^a$ where $a \sim -1.5$. Assuming that the jet dimming is due to adiabatic expansion they proposed that either the jet has a constant speed on pc-scales, which would be consistent with "magnetic driving" in Poynting-flux-dominated jets or that the jet is cylindrical and accelerating on pc-scales. They could not rule out either of those possibilities but they favoured the former. Additionally, they detected X-ray jets in 9 sources suggesting that FR-I jets start out relativistic on pc-scales and then slow down on kpc-scales.

Chapter 4

Spectral Line Fitting

4.1 pahfitMCMC

The original PAHFIT software by Smith et al. (2007) is an IDL code designed to fit narrow emission and absorption features in low-resolution *Spitzer*/IRS spectra. Gallimore et al. (2010) modified PAHFIT to subtract these spectral features from the spectrum leaving the continuum to be fitted by another program and they have since ported their modified PAHFIT to Python. That port is pahfitMCMC, a Markov-chain Monte Carlo narrow-line fitting algorithm written in Python to allow access to PAHFIT's functionality for researchers at institutions without an IDL license.

According to the pahfitMCMC documentation by Gallimore (in prep), pahfitMCMC reports fitted line strengths and equivalent widths for narrow emission lines as well as PAH and silicate features. It then produces a line-subtracted spectrum for each source to which we fit continuum models in Chapter 7.

Brooks et al. (2011) describe Markov chains as a list of random elements of a set in which the conditional distribution of an element in that list is solely dependent on the previous element. Markov-chain Monte Carlo (MCMC) algorithms use Markov chains to probabilistically search through a large parameter space much more efficiently than a simple grid

search. Implementation primarily varies based on the "stepper" algorithm which increments the Markov chain through parameter space based on some probability distribution based on the current element.

4.2 Results

We show the resulting fits from pahfitMCMC in Figure 4.1 and list the fit parameters in Appendix B. We discuss the important diagnostics in Sections 4.2.1-4.2.3.

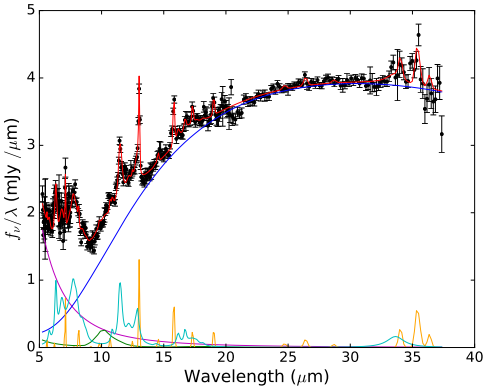

(a) NGC 315

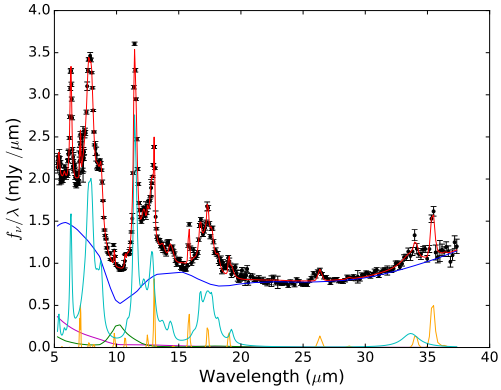

(b) 3C 31

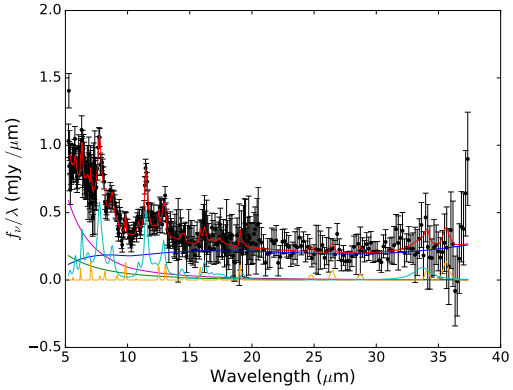

(c) NGC 541

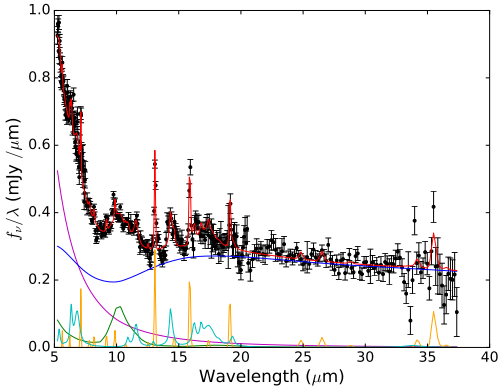

(d) 3C 66B

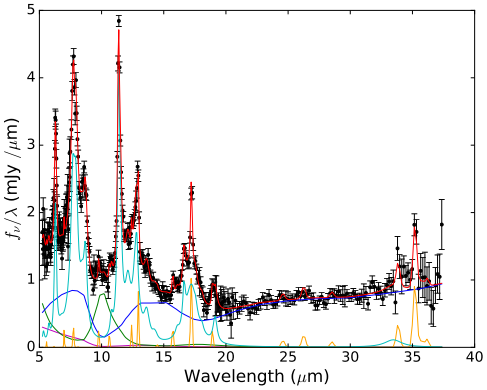

(e) NGC 3801

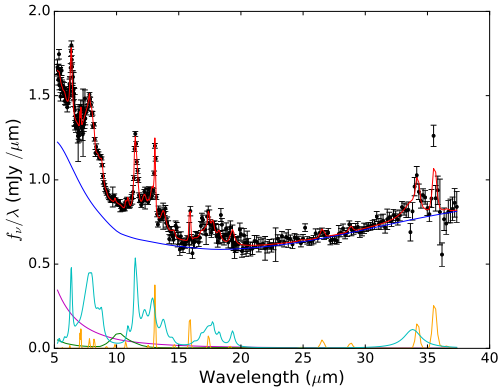

(f) NGC 3862

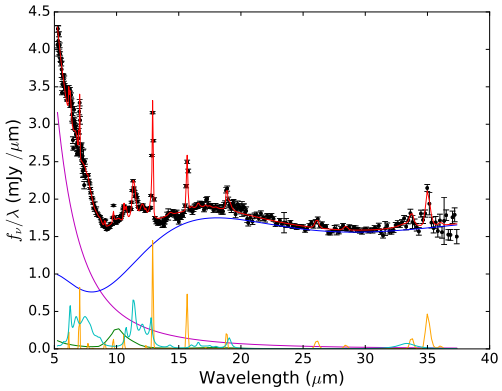

(g) 3C 270

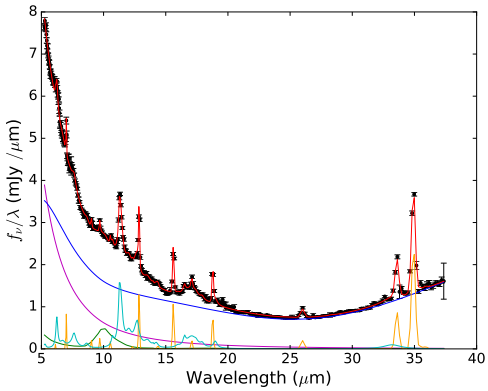

(h) M 84

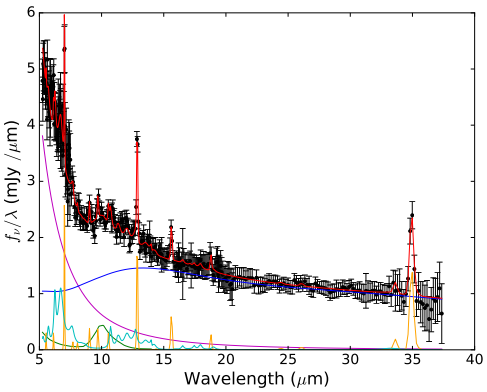

(i) M 87

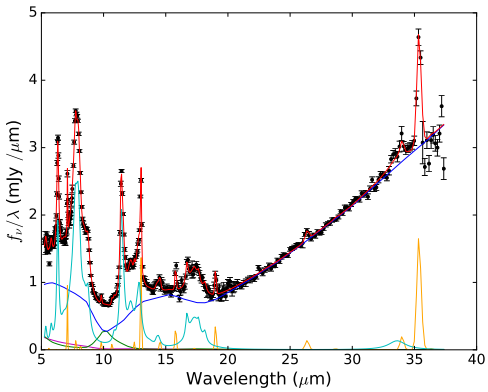

(j) NGC 7052

Figure 4.1 Spectral line fits for six of the sample galaxies. In each fit the red line is the total fit, the dark blue line is the line-subtracted spectral energy distribution minus any power law component, the purple line is the power law component, the green line represents the silicate features, light blue represents polycyclic aromatic hydrocarbon (PAH) lines, and yellow represents the narrow ionization lines.

4.2.1 Star formation rate estimates

We use $L_{[\mathrm{NeII}]}$ and $L_{[\mathrm{NeIII}]}$, the luminosities [NeII] and [NeIII] lines respectively, to estimate the star formation rate (SFR) in each sample galaxy. This estimate by Ho & Keto (2007), SFR_{Ne}, is given as

$$SFR_{\mathrm{Ne}} = 4.73 \times 10^{-41}\, M_{\odot}\,\mathrm{yr}^{-1}\mathrm{s}\ \mathrm{erg}^{-1}\ \left[L_{[\mathrm{NeII}]} + L_{[\mathrm{NeIII}]}\right]. \tag{4.1}$$

Similarly, we use the combined luminosity of the 6.2 and 11.3 μm PAH lines, L_{PAH} to get a second independent estimate of the SFR in each source. This estimate by Farrah et al. (2007), $\mathrm{SFR}_{\mathrm{PAH}}$ is given by

$$\mathrm{SFR}_{\mathrm{PAH}} = 1.18 \times 10^{-41}\, M_{\odot}\,\mathrm{yr}^{-1}\mathrm{s}\ \mathrm{erg}^{-1}\ \left[L_{\mathrm{PAH}}\right] \tag{4.2}$$

Willett et al. (2010) showed that Equations 4.1 and 4.2 are equivalent. However, Jensen et al. (2017) found that AGN activity can dominate PAH emission in Seyfert galaxies and it is currently unknown whether this finding will generalise to include FR-1 radio galaxies. In Figure 4.2, we attempt to verify Willett et al. (2010)'s findings for our sample.

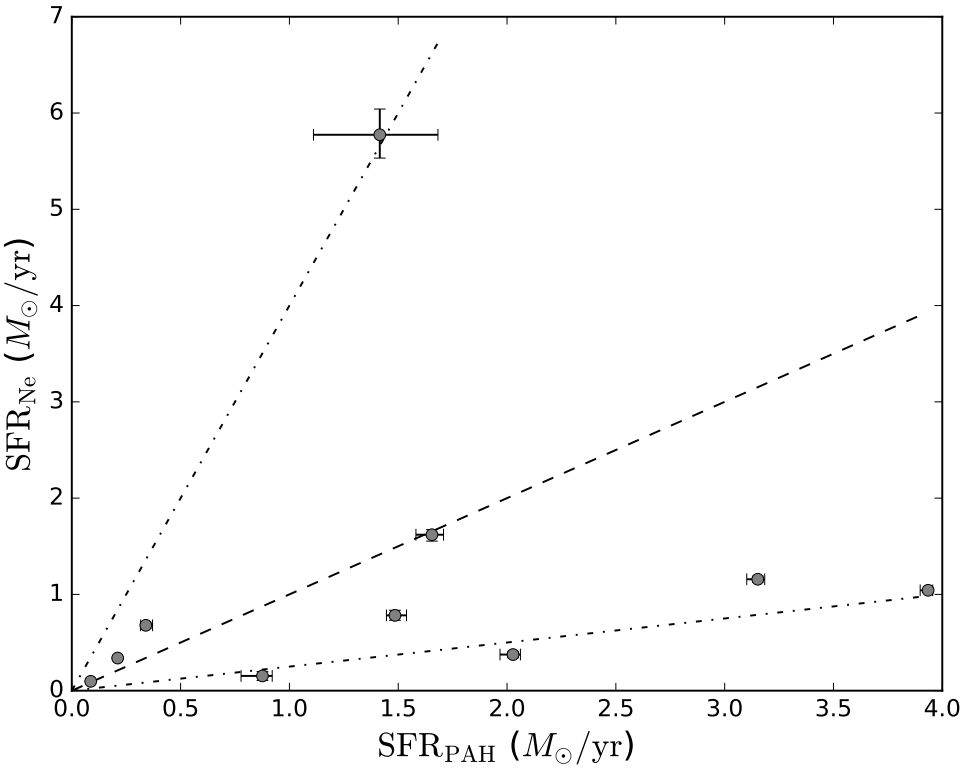

Figure 4.2 Comparison between star formation rate estimates based on PAH and Neon ([NeII] and [NeIII]) lines i.e., Equations 4.1 and 4.2. The dashed line is a visual aid showing $\mathrm{SFR_{Ne}} = \mathrm{SFR_{PAH}}$. It can be seen that estimates for most sources agree to within a factor of about four (dot-dash lines denote a factor of four each way).

Source	$\mathrm{SFR_{PAH}}$ ($\mathrm{M_\odot\,yr^{-1}}$)	$\mathrm{SFR_{Ne}}$ ($\mathrm{M_\odot\,yr^{-1}}$)
NGC 315	$1.655^{+0.108}_{-0.074}$	$1.62^{+0.053}_{-0.066}$
3C 31	$3.935^{+0.035}_{-0.037}$	$1.043^{+0.021}_{-0.023}$
NGC 541	$0.876^{+0.097}_{-0.098}$	$0.153^{+0.045}_{-0.047}$
3C 66B	$0.340^{+0.024}_{-0.024}$	$0.679^{+0.031}_{-0.03}$
NGC 3801	$2.028^{+0.059}_{-0.060}$	$0.375^{+0.034}_{-0.033}$
NGC 3862	$1.485^{+0.04}_{-0.039}$	$0.782^{+0.053}_{-0.051}$
3C 270	$0.211^{+0.006}_{-0.007}$	$0.339^{+0.004}_{-0.004}$
M 84	$0.087^{+0.003}_{-0.003}$	$0.097^{+0.001}_{-0.002}$
M 87	$1.415^{+0.306}_{-0.305}$	$5.774^{+0.267}_{-0.242}$
NGC 7052	$3.152^{+0.039}_{-0.051}$	$1.157^{+0.032}_{-0.029}$

Table 4.1: SFR estimates for each source based on narrow emission features.

4.2.2 High-ionization lines

Significant emission lines from high-ionisation states with a high ionisation potential require a large source of high energy photons. These can come from massive stars but the obvious photon source candidate in an AGN is the central engine itself. Indeed, Spinoglio & Malkan (1992) showed that you can distinguish star formation from accretion based on which lines are excited; AGN produce photons that can ionise atoms with a higher ionisation potential. However, these high-energy photons from an accretion disk should be unable to penetrate a dusty obscuring torus. We list the luminosities of 4 high-ionisation lines which are accretion tracers in Table 4.2: [NeVI] 8 μm, [NeV] 14 μm, [NeV] 24 μm, and [OIV] 26 μm.

Source	$L_{[\mathrm{NeVI}]}$ 8 μm ($10^{39}\,\mathrm{erg\,s^{-1}}$)	$L_{[\mathrm{NeV}]}$ 14 μm ($10^{39}\,\mathrm{erg\,s^{-1}}$)	$L_{[\mathrm{NeV}]}$ 24 μm ($10^{39}\,\mathrm{erg\,s^{-1}}$)	$L_{[\mathrm{OIV}]}$ 26 μm ($10^{39}\,\mathrm{erg\,s^{-1}}$)
NGC 315	< 5.87	< 4.76	< 2.98	< 4.98
3C 31	< 5.24	< 3.32	< 0.823	$3.46^{+0.72}_{-0.77}$
NGC 541	< 5.75	< 7.87	< 4.67	< 6.28
3C 66B	< 2.26	< 3.59	< 1.95	< 3.10
NGC 3801	< 11.26	< 2.45	< 3.78	< 3.20
NGC 3862	< 5.43	< 2.20	< 2.86	< 4.12
3C 270	$0.355^{+0.083}_{-0.088}$	< 0.490	< 0.268	< 0.924
M 84	< 0.130	< 0.207	< 0.0326	$0.318^{+0.038}_{-0.064}$
M 87	< 1.35	< 0.700	< 0.536	< 0.751
NGC 7052	$3.55^{+1.21}_{-1.05}$	< 12.32	< 2.00	< 7.60

Table 4.2: High-ionization line luminosities. The majority of entries are upper limits on non-detections.

4.2.3 Silicates

Baum et al. (2010) describe how cospatial silicate emission features at 10 and 18 μm were one of the main driving factors in the development of the clumpy torus model as opposed to smooth torus or shell models of AGN obscuration. In Figure 4.3 we compare the silicate line strengths S_{sil} (defined in Equation 4.3 in terms of the observed flux of the feature f_{obs} and the interpolated continuum flux f_{cont} at the peak wavelength) that we found in Chapter 4 to various clumpy torus and smooth shell models.

$$S_{\mathrm{sil}} = \log\left(\frac{f_{\mathrm{obs}}}{f_{\mathrm{cont}}}\right) \tag{4.3}$$

Nenkova et al. (2008b) model the radial distribution of the clumpy torus N_r as the power law distribution in Equation 4.4. Figures 4.3a-4.3c show the comparison to model sets, each with various numbers N of clouds along the line of sight, by Sirocky et al. (2008) with power law index q of 0-2 respectively.

$$N_r \propto r^{-q}, \tag{4.4}$$

Similarly, the mass distribution of the single continuous cloud in the smooth shell model also follows a power law, this time still described by the power law index and also by the radial extent of the cloud Y (given in units of the dust sublimation radius).

$$\rho_r \propto r^{-q}, \tag{4.5}$$

We find that the silicate line strengths are inconsistent with smooth shell models of AGN obscuration and with clumpy models with power law indices $q > 1$ and are consistent with clumpy models with $q \leq 1$ and $N \leq 5$ although a few are also consistent with the complete absence of any 18 μm silicate feature. Note that in Chapter 5 we find that only four of our ten sources show a significant thermal component in their continua, which we denote with blue and yellow markers in Figures 4.3a-4.3c.

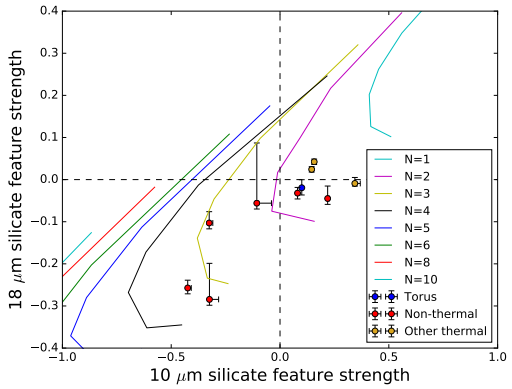

(a) Clumpy torus model, $q = 0$

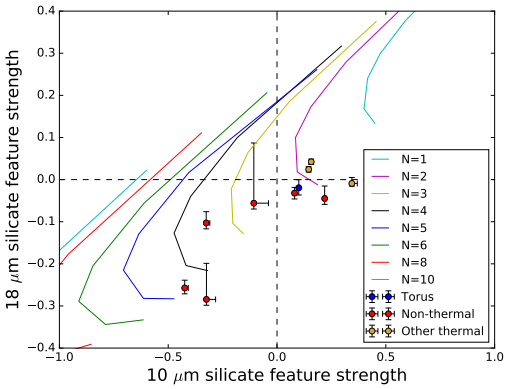

(b) Clumpy torus model, $q = 1$

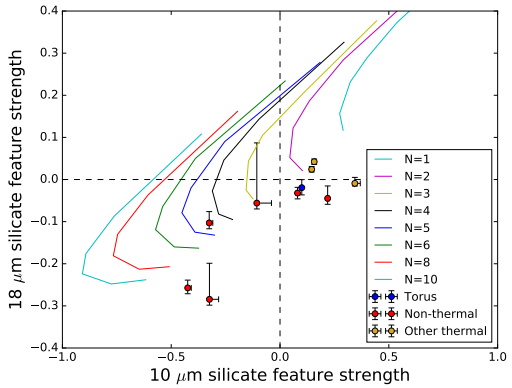

(c) Clumpy torus model, $q = 2$

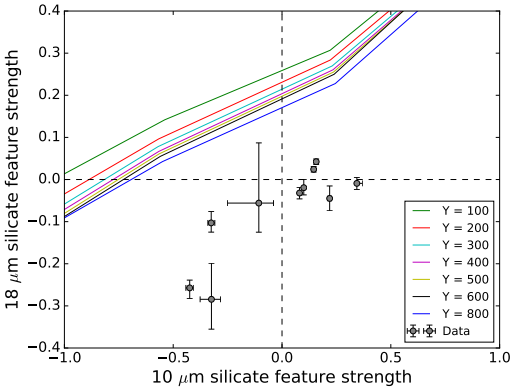

(d) Smooth shell model, $q = 0$

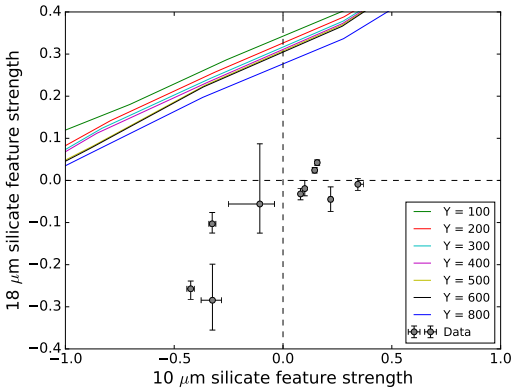

(e) Smooth shell model, $q = 1$

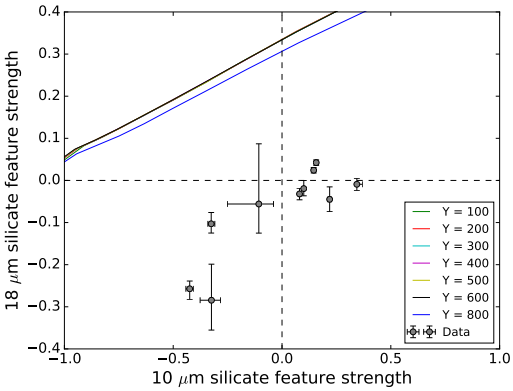

(f) Smooth shell model, $q = 2$

Figure 4.3 Comparison of silicate absorption/emission strengths to predictions of various smooth and clumpy torus models. Y is given in units of the dust sublimation radius. Note that there is significant overlap between the region occupied by the clumpy torus models with $q = 0$ and the region occupied by the data. There is less overlap between the data and the $q = 1$ clumpy torus models and no significant overlap with any other model sets. Galaxies with thermal components (torus, NLR, and/or hot dust) in our continuum fits (see Section 5.2) are flagged with different colours in the clumpy torus model plots.

Chapter 5

Continuum Fitting

5.1 clumpyDREAM

This section and Section 5.1.1 are primarily based on the clumpyDREAM documentation by Gallimore (in prep).

Our main continnum fitting program, a development version of clumpyDREAM, was first described by Sales et al. (2015). It is a Python software package which uses a Markov-chain Monte Carlo algorithm. It is designed to fit continuum models to low-resolution line-subtracted *Spitzer*/IRS spectra but can also accommodate broadband near-infrared(NIR), far-infrared, and sub-mm measurements to constrain the fits. We describe the model components in Sections 1.3.1 and 5.1.1 and list them for quick reference in Table 5.1.

Since we are testing models with different numbers of parameters, using a chi-square goodness-of-fit as in Chapter 4 would lead to overfitting. We instead use the Bayesian Information Criterion (BIC) goodness-of-fit test, proposed by Schwarz (1978) and shown in Equation 5.1, which maximizes the likelihood function $\mathcal{L}$ while penalizing extraneous parameters (i.e., the dimensionality of the model k). It is particularly beneficial for data sets with a large number of data points n.

$$\mathrm{BIC} = -2\ln[\mathcal{L}] + k\ln(n) \tag{5.1}$$

5.1.1 Model components

In this Section we describe each of the model components we try to fit with clumpyDREAM except the clumpy torus model itself which we describe in Section 1.3.1. For quick reference we list all of these and their source papers in Table 5.1.

These targets are galaxies so we force the model to include an old stellar population component for every source as well as a diffuse interstellar medium (ISM). We use the GRASIL stellar population model for elliptical galaxies developed by Silva et al. (1998) and the diffuse ISM model described by Draine & Li (2007). The clumpyDREAM documentation states that the stellar population models are not expected to contribute significantly in the IRS band but that they should dominate the NIR and so should be well constrained by our 2MASS and IRAC photometry. Our results in some cases favour models in which stars contribute significantly to the IRS band, particularly at the short-wavelength end, but this is not surprising due to the dim nucleus. In Section 5.2, however, there is significant contribution from the stellar population model through the short-wave end of the IRS band in several of our sources which is likely due to the low overall IRS band luminosity of those sources. The GRASIL models simulate a 1 Gyr burst of star formation followed by passive evolution and so are described solely by the age and scaling of the stellar population.

The diffuse ISM model by Draine & Li (2007) has three main parameters: the mass fraction of polycyclic aromatic hydrocarbons q_{PAH} relative to the total dust mass, the lower limit of the interstellar radiation field as a scaling of that in the solar neighbourhood U_{min}, and photo-dissociation regions exposed to $U_{\mathrm{max}} = 10^6 U_{\mathrm{min}}$ which are characterised by their relative contribution γ to the spectrum.

We use a narrow-line region (NLR) model, developed by Nenkova et al. (1999), together with a $800\,\mathrm{K} \leq T \leq 1600\,\mathrm{K}$ blackbody hot dust model. This approach is similar to the

one taken by Mor et al. (2009) in order to fit IRS spectra of quasi-stellar objects (QSOs). Mor et al. (2009) also attempted torus models and models with both a torus and an NLR and found that neither were adequate. Since we are extending our dataset beyond the IRS band into the far-infrared/sub-mm we consider a cold dust component as well. All three components are described in our models by two parameters each — their temperature and their luminosity. Note that the NLR clouds and hot dust are optically thin.

We also try a foreground extinction component, as described by Fischera et al. (2003), on the torus in 3C 31, NGC 3801, and M 84. These sources appear to have regions with decreased brightness compared to adjacent regions at the same radius which could be foreground dust in SDSS images by Blanton et al. (2017) although it is only obvious in NGC 3801. On a similar note we only tested power-law synchrotron spectra in sources with known optical/IR jets. These are 3C 31 (Lanz et al., 2011), 3C 66B (Tansley et al., 2000), NGC 3862 (Crane et al., 1993), and M 87 (Perlman et al., 2001). We constrain the power law indices to the widest ranges given in their reference papers.

Component	Plotting colour	Reference
Clumpy torus	Green	Nenkova et al. (2008b)
Hot dust	Pink	-
Cold dust	-	-
Diffuse ISM	Blue	Draine & Li (2007)
Single stellar population	Yellow	Silva et al. (1998)
Foreground extinction on torus	-	Fischera et al. (2003)
Power law	Purple	-
Narrow line region	Cyan	Nenkova et al. (1999)
Aperture correction	-	-

Table 5.1: Possible model components. Extinction and aperture correction aren't plotted as model components; they alter other model components. No sources require a cold dust component however our far-infrared data are only upper limits. The "hot dust" and "cold dust" components are blackbodies.

5.2 Results

In Sections 5.2.1-5.2.10 we present the best fit models for the continuum emission from each of our sample galaxies. Additionally, we present the results of forcing a torus component and suppressing all other thermal components in order to establish a firm upper limit on the contribution to the total flux from any possible torus component which may otherwise be hidden by fitting degeneracies between thermal model components. Finally, we present an overview of the results for the entire sample in Section 5.2.11.

5.2.1 NGC 315

This source favours a torus component and that torus component is a significant part of the best fit, contributing $\sim 70\%$ of the flux at 15 and 30 μm and $\sim 50\%$ at 60 μm. There is possible degeneracy between the torus component and NLR component but we doubt that this is a significant concern in this case due to the fact that the BIC will penalise the torus model more harshly due to its higher number of parameters. We therefore see no particular reason to doubt the presence of an obscuring warm torus-like structure in this AGN.

The presence of a torus component in the spectral energy distribution of NGC 315 is consistent with the discovery of broad polarised Hα emission in this source by Barth et al. (1999). Which may indicate the presence of a Thomson-scattered hidden broad line region.

Similarly, Gu et al. (2007) detected a low-luminosity compact AGN in IRAC and MIPS images of NGC 315 after removal of stellar IR emission and accounting for emission from a central dusty disk. They make no claims about the nature of this AGN however its presence is consistent with our result that the IR spectrum of NGC 315 is not entirely dominated by emission from the host galaxy.

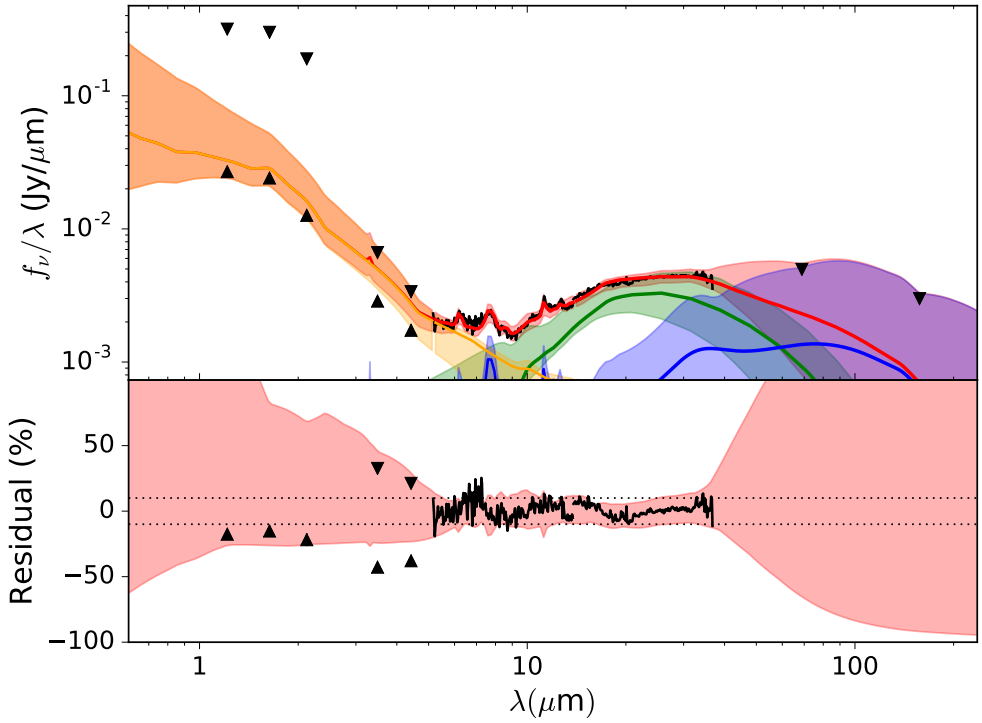

Figure 5.1 Best continuum fit for NGC 315. Model consists of an old stellar population (yellow), diffuse ISM (blue) and clumpy torus (green). The total fit is shown in red although in the NIR it appears as orange due to overlap with the stellar population.

Component	Wavelength (μm)	Best fit (%)	Minimum (%)	Maximum (%)
Torus	5.0	1.4	0.8	33.5
	15.0	69.0	59.4	97.8
	30.0	69.9	40.8	100
	60.0	47.8	13.5	91.9
Diffuse ISM	5.0	1.8	0.2	2.9
	15.0	10.4	1.7	20.1
	30.0	24.7	1.7	64.9
	60.0	50.1	4.2	100
Stars	5.0	96.8	58.8	100
	15.0	20.6	2.1	22.8
	30.0	5.4	0.2	6.0
	60.0	2.0	0.0	2.2

Table 5.2: Fractional contributions of the various model components to the overall continuum in NGC 315.

5.2.2 3C 31

This source appears to be dominated by emission from the host galaxy in the IRS band. The optical jet first noticed by Butcher et al. (1980), which Croston et al. (2003) identify as the same structure as the radio jet, does not contribute substantially to the IR core flux. It is worth noting, however, that Lanz et al. (2011) detect extended NIR emission from the jet at kpc scales in *Spitzer*/IRAC images. As shown in Figure 5.3 and in Table 5.4, when a torus component is forced it contributes a significant amount of flux at 15 μm and 30 μm with best fit fractional contributions of 34.2% and 18.7% respectively. However, as shown in Table 5.28, the BIC difference between galaxy models with a forced torus and galaxy-only models is a significant 22.2 and we notice no obviously unphysical best fit model parameters, therefore we conclude that we do not find evidence for a warm obscuring torus in the infrared spectra of 3C 31. We note, however, that Constantin et al. (2015) detected broad Hα emission with a FWHM of 2710 $\mathrm{km\,s^{-1}}$, contributing 86% of the combined narrow+broad Hα flux. This broad Hα is consistent with the presence of a broad line region and therefore possibly an accretion disk.

Component	Wavelength (μm)	Best fit (%)	Minimum (%)	Maximum (%)
Diffuse ISM	5.0	4.2	3.0	5.0
	15.0	57.0	43.2	64.4
	30.0	83.6	65.7	100
	60.0	99.1	18.7	100
Stars	5.0	95.8	83.0	100
	15.0	43.0	27.2	64.6
	30.0	16.4	5.6	25.0
	60.0	0.9	0.2	1.2

Table 5.3: Fractional contributions of the various best fit model components to the overall continuum in 3C 31.

Component	Wavelength (μm)	Best fit (%)	Minimum (%)	Maximum (%)
Torus	5.0	8.0	0.0	13.6
	15.0	34.2	0.0	48.7
	30.0	18.7	0.0	54.2
	60.0	0.4	0.0	11.2
Diffuse ISM	5.0	3.6	2.8	4.4
	15.0	51.1	39.6	59.3
	30.0	77.9	45.2	98.4
	60.0	99.4	19.9	100
Stars	5.0	88.4	73.5	98.9
	15.0	14.8	8.0	59.3
	30.0	3.4	1.2	24.7
	60.0	0.2	0.0	1.3

Table 5.4: Fractional contributions of the various model components to the overall continuum in 3C 31 with a forced torus component.

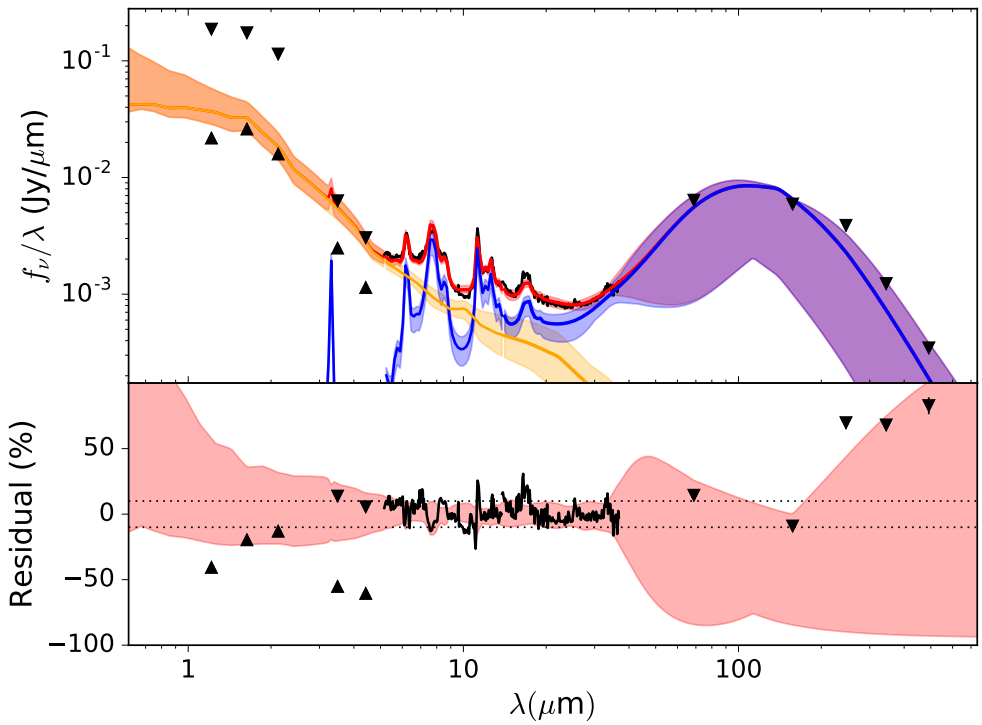

Figure 5.2 Best continuum fit for 3C 31. Model consists of an old stellar population (yellow) and diffuse ISM (blue). The total fit is shown in red although in the NIR it appears as orange due to overlap with the stellar population. This is the only source with a complete data set.

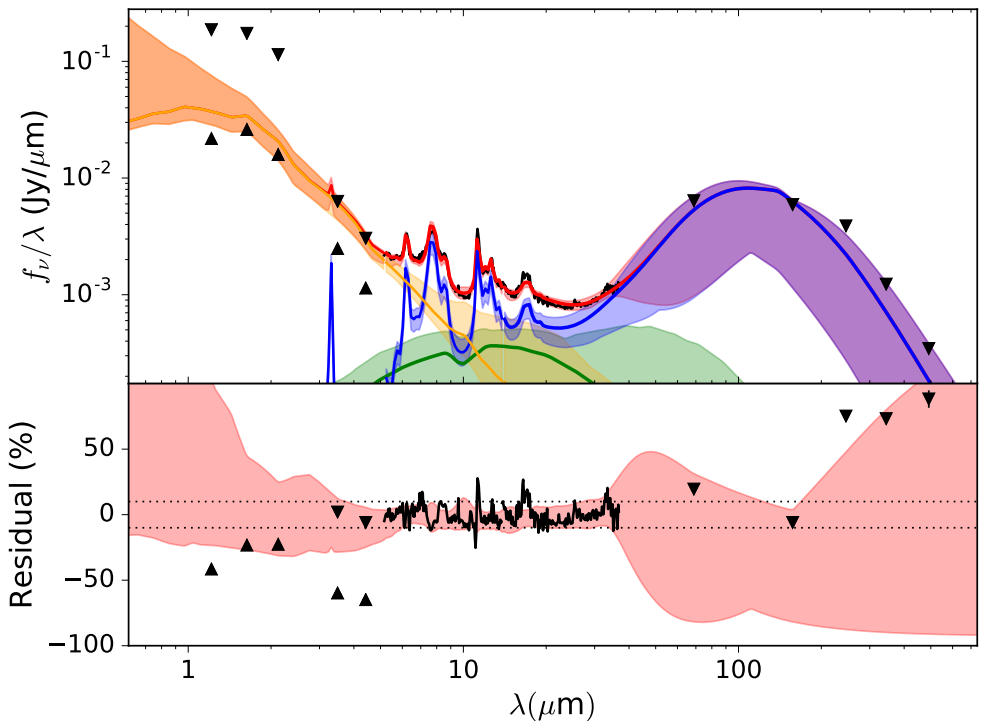

Figure 5.3 Continuum fit for 3C 31 forcing a torus component (green). Model is otherwise the same as in Figure 5.2.

5.2.3 NGC 541

Not only does the best fit to the continuum emission in this source not contain a torus component but the best fit contribution from a forced torus component is not significant, contributing only $\sim 20\%$ at its brightest. The largest difference between the best fit model and the data is the 70 μm but that point is an upper limit and it is within the uncertainty. We therefore conclude that we can explain all the emission with only contributions from the host galaxy and none from the nucleus and so rule out any significant MIR-bright obscuration.

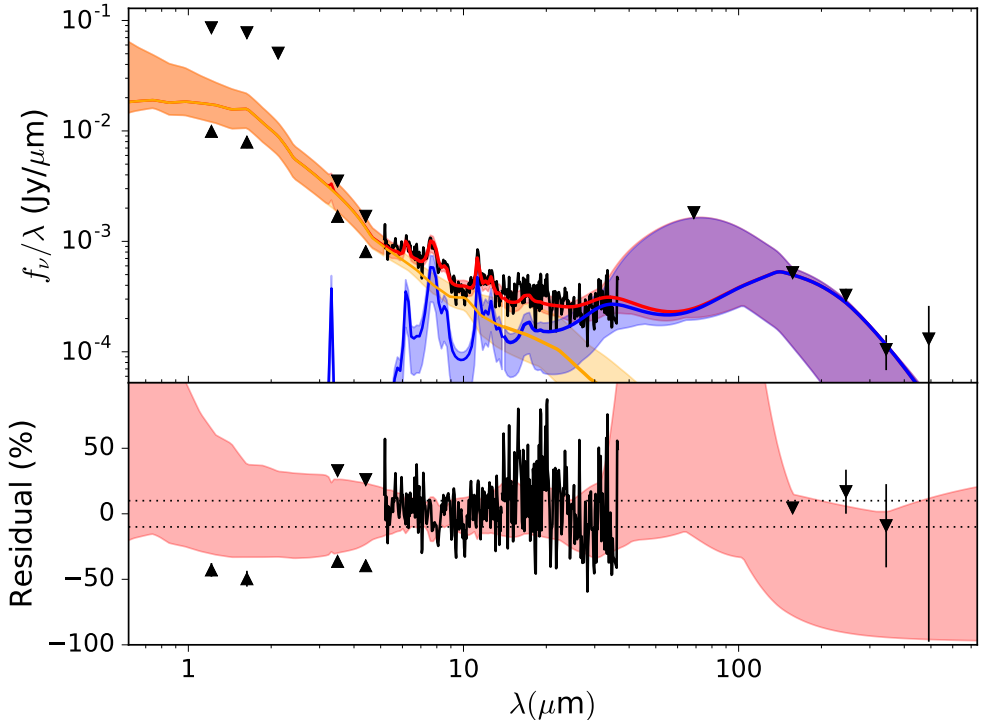

Figure 5.4 Best continuum fit for NGC 541. Model consists of an old stellar population (yellow) and diffuse ISM (blue). The total fit is shown in red although in the NIR it appears as orange due to overlap with the stellar population. Upright triangles represent lower limits from photometry and inverted triangles represent upper limits.

Component	Wavelength (μm)	Best fit (%)	Minimum (%)	Maximum (%)
Diffuse ISM	5.0	2.0	0.9	2.5
	15.0	43.8	21.1	52.1
	30.0	82.1	36.3	100
	60.0	94.7	79.0	100
Stars	5.0	98.0	80.3	100
	15.0	56.2	33.0	100
	30.0	17.9	6.2	35.4
	60.0	5.3	1.3	10.1

Table 5.5: Fractional contributions of the various model components to the overall continuum in the best fit model of NGC 541.

Component	Wavelength (μm)	Best fit (%)	Minimum (%)	Maximum (%)
Torus	5.0	0.0	0.0	13.9
	15.0	4.3	0.0	78.8
	30.0	20.7	0.0	81.4
	60.0	15.7	0.0	100
Diffuse ISM	5.0	1.8	0.8	2.4
	15.0	36.8	20.2	51.4
	30.0	57.4	23.3	100
	60.0	78.6	39.9	100
Stars	5.0	98.1	74.6	100
	15.0	58.9	11.9	99.6
	30.0	21.9	1.7	40.1
	60.0	5.7	0.2	10.1

Table 5.6: Fractional contributions of the various model components to the overall continuum in NGC 541 with a forced torus component.

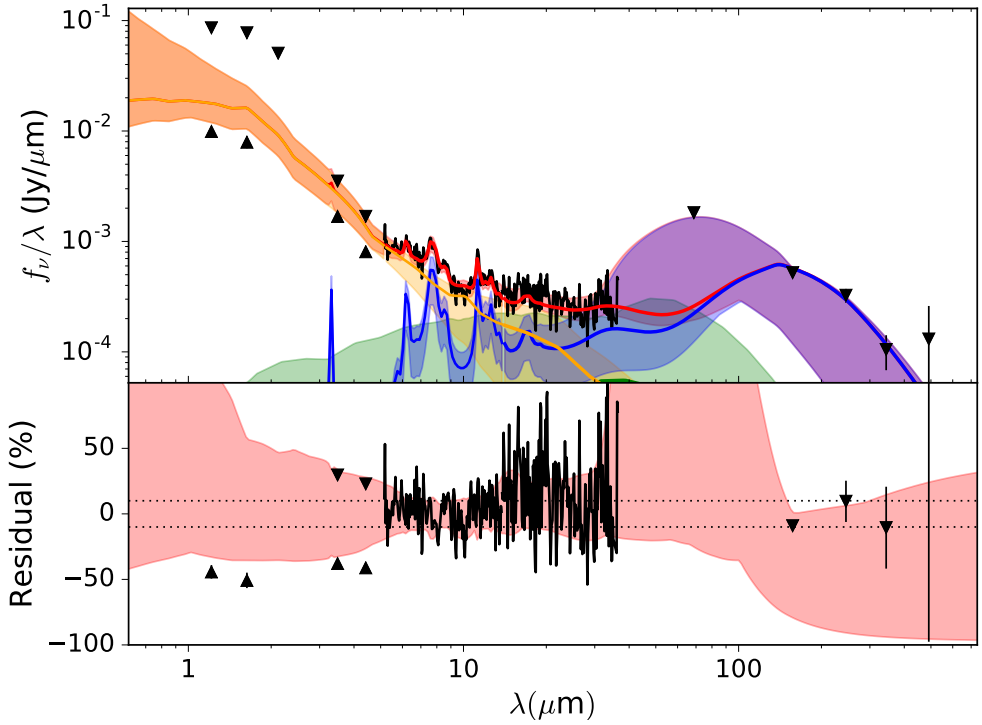

Figure 5.5 Continuum fit for NGC 541 forcing a torus component (green). Model is otherwise the same as in Figure 5.4.

5.2.4 3C 66B

The best fit for this source contains a prominent hot dust component and a significant NLR model component. The best fit to the diffuse ISM component is unusually dim but the uncertainties are wide.

The upper limit provided by the fit with a forced torus component is a significant fraction of the total flux but the forced torus is unusually cold, suppresses the diffuse ISM component, and those two fits have a large BIC difference (best: 472.3, forced torus: 506.8) of 34.5. We note that the BIC difference may be primarily due to the removal of the hot dust component since we expect the most degeneracy between the NLR and torus components as they are both MIR thermal components. Overall, we cannot rule out the possibility of a torus, especially given the presence of another MIR thermal component, but we also don't favour the presence of a torus so we consider our results inconclusive with regard to the presence of a clumpy torus but our results quite strongly indicate the presence of some MIR thermal

component.

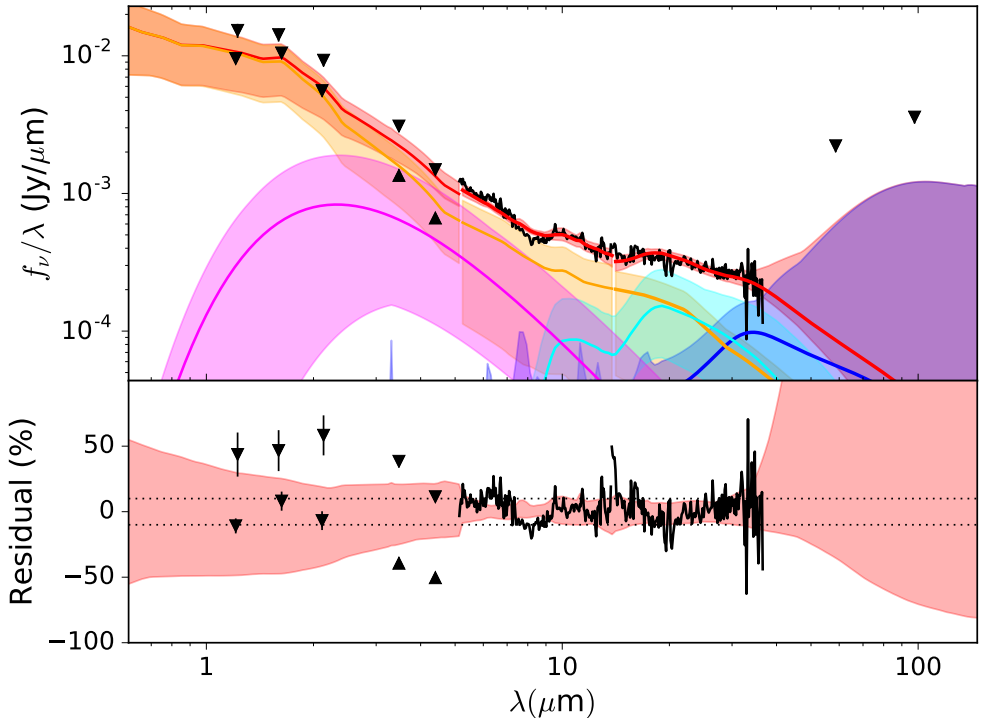

Figure 5.6 Best continuum fit for 3C 66B. Model consists of an old stellar population (yellow), hot dust (pink), NLR (cyan), and diffuse ISM (blue). The total fit is shown in red although in the NIR it appears as orange due to overlap with the stellar population. We have applied aperture correction between the SL and LL regions. Upright triangles represent lower limits from photometry and inverted triangles represent upper limits.

Component	Wavelength (μm)	Best fit (%)	Minimum (%)	Maximum (%)
Diffuse ISM	5.0	0.1	0.0	0.5
	15.0	5.9	0.1	11.8
	30.0	35.1	0.5	58.9
	60.0	66.7	1.1	100
Stars	5.0	64.0	31.4	83.2
	15.0	59.5	13.2	80.3
	30.0	28.7	3.1	38.6
	60.0	19.6	1.6	26.1
NLR	5.0	0.0	0.0	0.1
	15.0	26.1	11.6	49.2
	30.0	34.6	13.0	70.6
	60.0	12.9	4.4	48.2
Hot dust	5.0	35.9	8.8	84.5
	15.0	8.5	2.3	24.1
	30.0	1.7	0.4	5.1
	60.0	0.7	0.2	2.2

Table 5.7: Fractional contributions of the various model components to the overall continuum in the best fit model for 3C 66B.

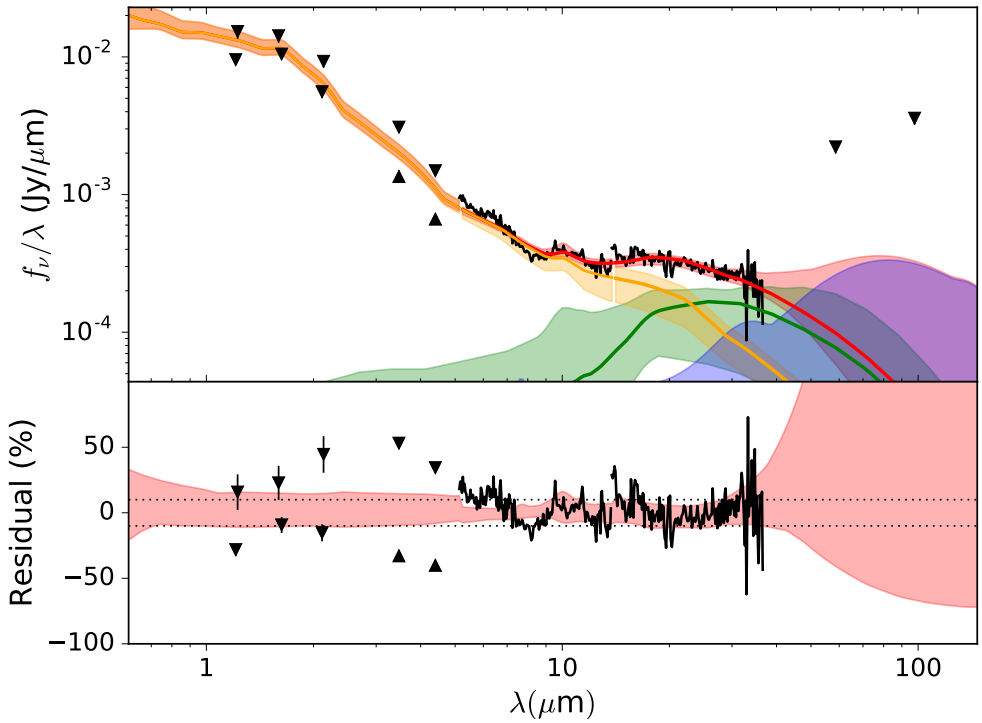

Figure 5.7 Continuum fit for 3C 66B forcing a torus component (green). To ensure maximal torus component we excluded the NLR and hot dust components seen in Figure 5.6.

Component	Wavelength (μm)	Best fit (%)	Minimum (%)	Maximum (%)
Torus	5.0	0.2	0.0	7.2
	15.0	26.7	11.4	50.0
	30.0	65.1	20.7	81.9
	60.0	78.7	17.2	100
Diffuse ISM	5.0	0.0	0.0	0.3
	15.0	0.0	0.0	7.7
	30.0	0.0	0.0	42.6
	60.0	0.1	0.0	100
Stars	5.0	99.8	90.9	100
	15.0	73.2	48.2	88.3
	30.0	34.9	22.5	41.8
	60.0	21.3	14.3	25.1

Table 5.8: Fractional contributions of the various model components to the overall continuum in 3C 66B with a forced torus component.

5.2.5 NGC 3801

The best fit for NGC 3801 contains a NLR component, however it is very dim and narrow so we suspect it is likely either a fitting artifact or possibly associated with a large-scale structure in the host galaxy. A likely candidate for this component from the host is the large dust lane visible near the AGN in *HST* images by Verdoes Kleijn et al. (1999). The forced-torus fit is significantly worse, with a BIC of 453.7 compared to the best-fit BIC of 423.5. We also show an extincted galaxy-only fit with a BIC of 437.3 in Figure 5.9 as a comparison since the dust lane which is a candidate thermal source would also provide foreground extinction on the core. Overall, we do not find evidence for nucleus obscuration in the form of a clumpy torus and our results are ambiguous for any other warm thermal component in the nucleus itself due to likely emission from the host galaxy.

Das et al. (2005) detected a flat-spectrum non-thermal core in NGC 3801 in 3 mm images from the Berkeley-Illinois-Maryland Association millimeter-wave array. This does not appear to contribute significantly to the IRS band and we have too little far-infrared photometry to properly compare. They also detected carbon monoxide CO(1-0) emission from the dust disk seen in *HST* images (Verdoes Kleijn et al., 1999) with a velocity gradient indicating a ~ 2 kpc rotating disk of molecular gas and dust with an inferred $3 \times 10^8\,M_\odot$ of molecular hydrogen. They also detected a $\sim 10^8\,M_\odot$ infalling molecular gas clump which they attribute to a recent merger.

Hota et al. (2012) found evidence in *GALEX* images of a kinematically decoupled core in NGC 3801 in which star formation has recently declined following a post-merger burst but the jet-driven shock has not yet triggered a burst of star formation in the outer regions to the galaxy. In comparison, our SFR estimates based on PAH fit results in Section 4.2.1 are higher than average for our sample and our SFR estimates based on narrow Neon lines are typical for the sample. Our continuum models have a bright diffuse ISM which may be associated with the large-scale gas Hota et al. (2012) predict will begin to form stars within the next 10 Myr. Our stellar population models show a high stellar age of 9.4 Gyr but as

mentioned in Section 1.3.1 our model only accounts for one burst of star formation followed by passive evolution so our results only suggest that the population of low-mass stars is still dominated by the older sub-population.

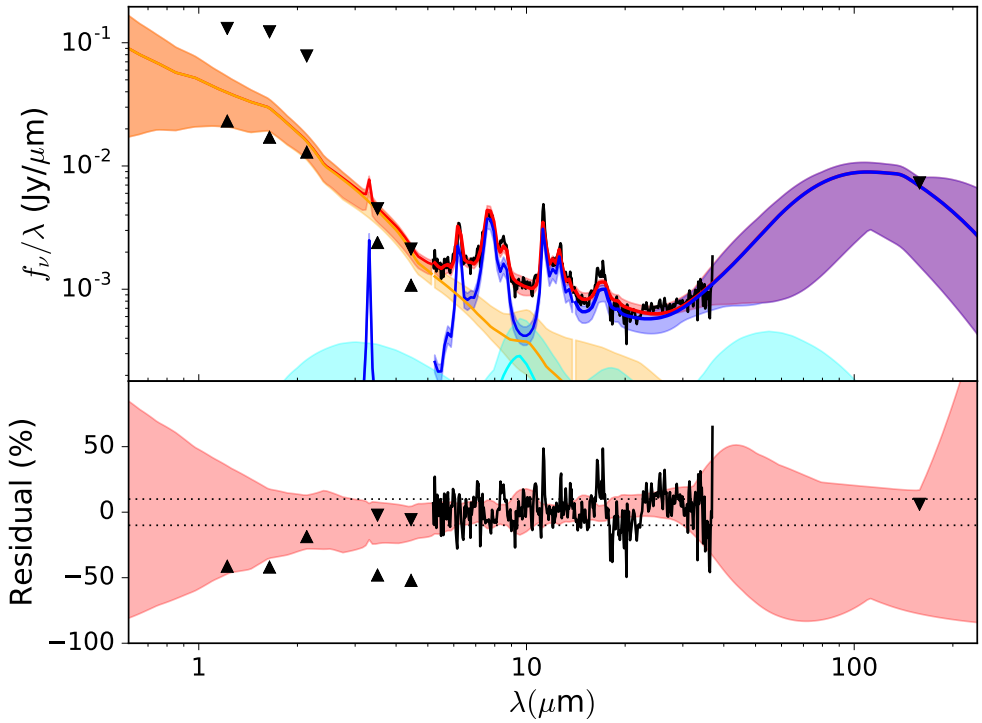

Figure 5.8 Best continuum fit for NGC 3801. Model consists of an old stellar population (yellow), NLR (cyan) and diffuse ISM (blue). The total fit is shown in red although in the NIR it appears as orange due to overlap with the stellar population.Upright triangles represent lower limits from photometry and inverted triangles represent upper limits.

Component	Wavelength (μm)	Best fit (%)	Minimum (%)	Maximum (%)
Diffuse ISM	5.0	7.0	5.7	8.0
	15.0	79.6	64.2	88.2
	30.0	96.4	74.9	100
	60.0	99.9	19.7	100
Stars	5.0	85.9	69.5	99.6
	15.0	16.1	6.7	44.6
	30.0	2.8	1.0	17.8
	60.0	0.1	0.0	0.7
NLR	5.0	7.1	0.0	14.3
	15.0	4.3	0.0	21.3
	30.0	0.8	0.0	14.8
	60.0	0.0	0.0	10.5

Table 5.9: Fractional contributions of the various model components to the overall continuum in the best fit model for NGC 3801.

Component	Wavelength (μm)	Best fit (%)	Minimum (%)	Maximum (%)
Torus	5.0	23.0	0.0	30.0
	15.0	13.0	0.0	34.2
	30.0	3.8	0.0	34.3
	60.0	0.0	0.0	13.1
Diffuse ISM	5.0	6.6	5.5	8.1
	15.0	76.7	61.2	87.2
	30.0	93.7	61.5	100
	60.0	99.9	18.2	100
Stars	5.0	70.4	58.6	100
	15.0	10.3	5.3	45.3
	30.0	2.5	0.8	18.7
	60.0	0.1	0.0	0.9

Table 5.10: Fractional contributions of the various model components to the overall continuum in NGC 3801 with a forced torus component.

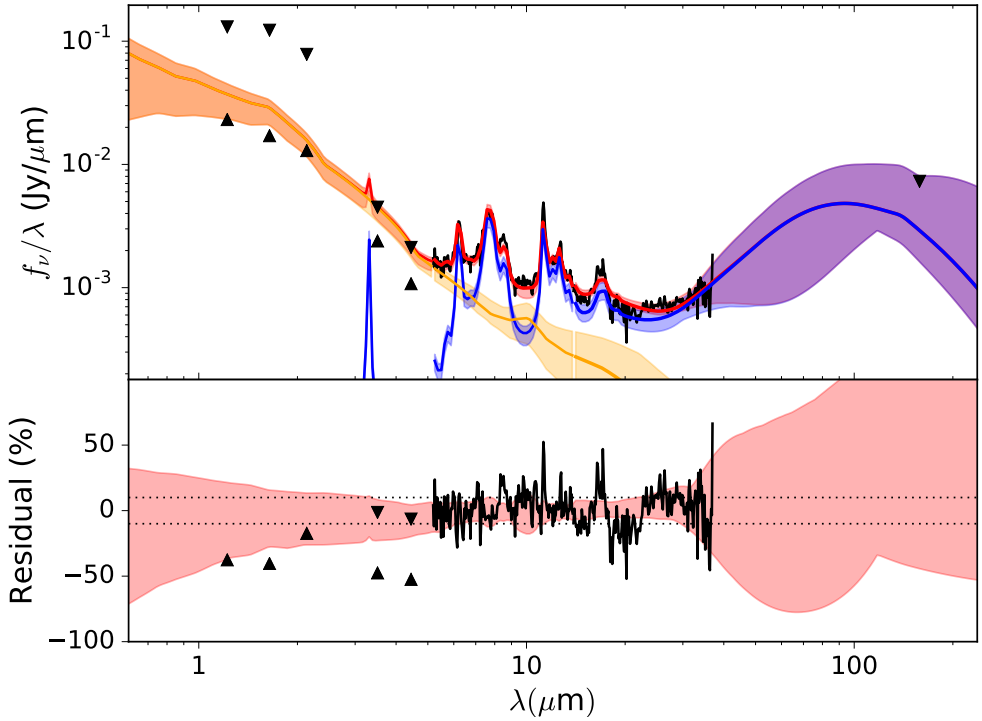

Figure 5.9 Galaxy-only continuum fit for NGC 3801. Model consists of an old stellar population (yellow) and diffuse ISM (blue). The total fit is shown in red although in the NIR it appears as orange due to overlap with the stellar population. This is a somewhat poorer fit than that in Figure 5.8 and still better than the forced-torus fit in Figure 5.10. This model also contains a foreground extinction component. Upright triangles represent lower limits from photometry and inverted triangles represent upper limits.

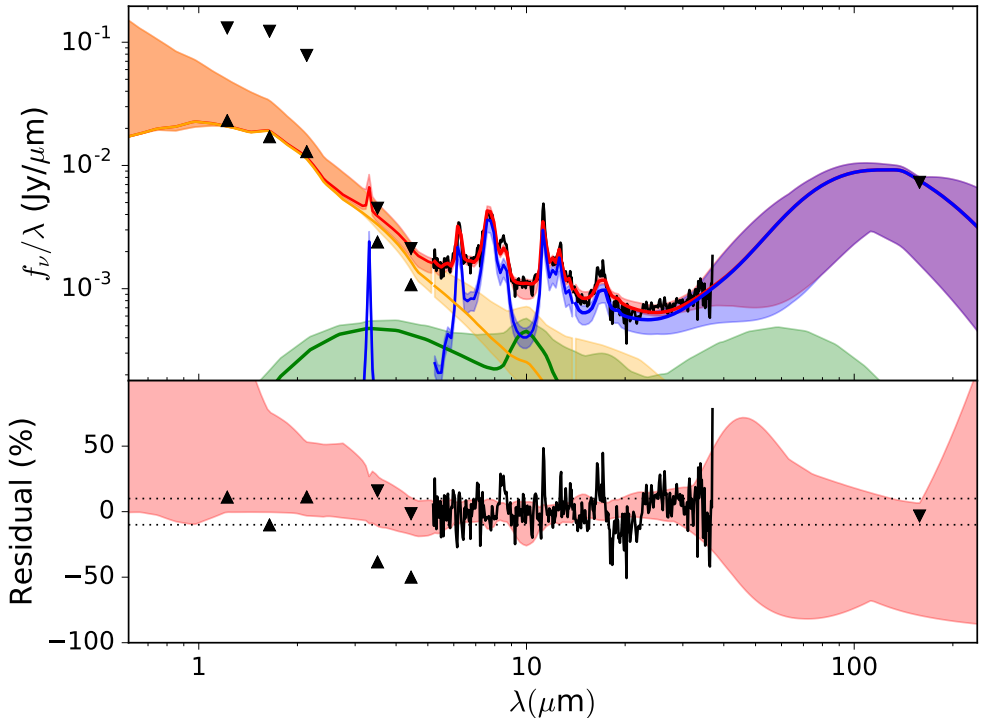

Figure 5.10 Continuum fit for NGC 3801 forcing a torus component (green). To ensure maximal torus component we excluded an NLR component seen in Figure 5.8 from the fit.

5.2.6 NGC 3862

The best fit model for this source contains only components from the host galaxy suggesting that the AGN does not contribute significantly to the IR flux. The largest difference between the best fit model and the data is the 70 μm but that point is an upper limit and it is within the uncertainty.

The forced torus model in this source is quite reasonable albeit rather warm with a peak around 10 μm, providing a firm upper limit on any possible torus component of $\sim$ 17% of the flux at 5 μm, $\sim$ 50% of the flux at 15 μm, and $\sim$ 13% of the flux at 30 μm. However, it is also unnecessary to explain the infrared spectrum as the best fit has a BIC of 391.9 and the forced-torus fit has a BIC of 420.3. Therefore, we see no evidence for a warm IR-bright obscuring structure in NGC 3862.

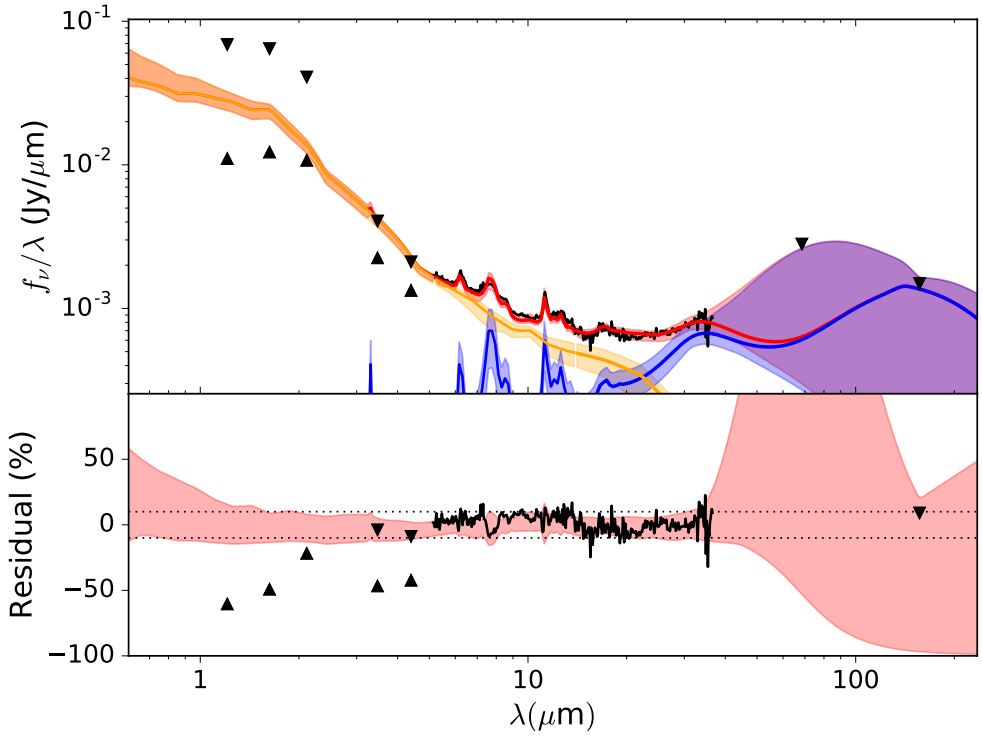

Figure 5.11 Best continuum fit for NGC 3862. Model consists of an old stellar population (yellow) and diffuse ISM (blue). The total fit is shown in red although in the NIR it appears as orange due to overlap with the stellar population. Upright triangles represent lower limits from photometry and inverted triangles represent upper limits.

Component	Wavelength (μm)	Best fit (%)	Minimum (%)	Maximum (%)
Diffuse ISM	5.0	1.5	0.8	2.0
	15.0	30.1	21.2	37.6
	30.0	77.4	63.5	95.7
	60.0	93.3	54.8	100
Stars	5.0	98.5	89.2	100
	15.0	69.9	54.9	81.6
	30.0	22.6	10.2	26.1
	60.0	6.7	2.5	7.6

Table 5.11: Fractional contributions of the various model components to the overall continuum in the best fit model for NGC 3862.

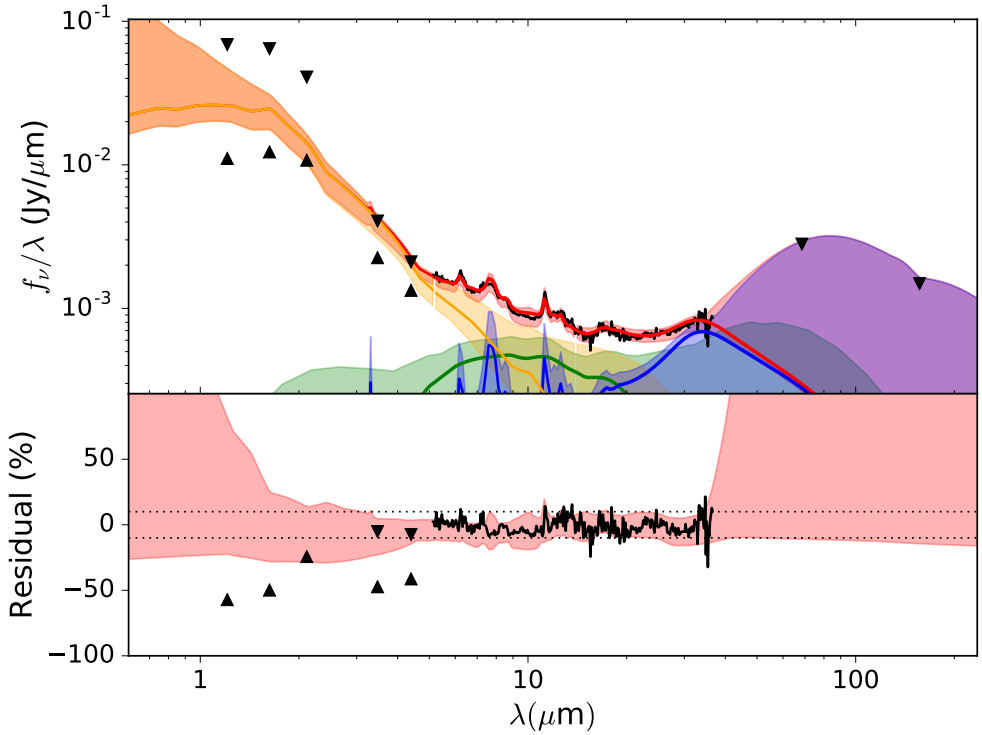

Figure 5.12 Continuum fit for NGC 3862 forcing a torus component (green). Model is otherwise the same as in Figure 5.11.

Component	Wavelength (μm)	Best fit (%)	Minimum (%)	Maximum (%)
Torus	5.0	16.7	0.0	27.3
	15.0	49.7	0.0	69.6
	30.0	13.0	0.0	68.5
	60.0	1.9	0.0	100
Diffuse ISM	5.0	1.3	0.5	2.0
	15.0	27.1	13.4	36.1
	30.0	78.1	12.4	87.6
	60.0	92.6	37.9	100
Stars	5.0	82.0	63.6	100
	15.0	23.2	8.1	82.4
	30.0	9.0	0.9	25.1
	60.0	5.5	0.2	12.1

Table 5.12: Fractional contributions of the various model components to the overall continuum in NGC 3862 with a forced torus component.

5.2.7 3C 270

We show our best fit for 3C 270 in Figure 5.13, the best fit with a forced torus component in Figure 5.14, and the fractional contributions to the flux in each of the two models in Tables 5.13 and 5.14 respectively. We suspect that the preference for a narrow-line region model in this source is due to a bias in our analysis since BIC favours models with fewer parameters and the NLR model has fewer parameters than a clumpy torus model. Therefore we cannot rule out a torus in this source. The presence of a torus in 3C 270 would be consistent with results by Antonucci (private communication) of broad polarized Hα emission indicative of a Thomson-scattered hidden broad line region such as that expected in a high-excitation AGN. Additionally, although van der Wolk et al. (2010a) ultimately do not conclude the existence of a warm MIR thermal component in any of the eight FR-I radio galaxies in their sample they list 3C 270 as a possible exception due to a weak MIR consistent with 200 K dust. Jaffe et al. (1993) note a $\sim 60\,\mathrm{pc}$ disk of cold dust in *HST* images of 3C 270 surrounding its unresolved nucleus, the inner regions of which may be heated by the AGN (or star formation but our SFR estimates are too low for that) to produce the MIR excess detected.

Component	Wavelength (μm)	Best fit (%)	Minimum (%)	Maximum (%)
Diffuse ISM	5.0	0.2	0.1	0.9
	15.0	5.0	2.9	17.2
	30.0	23.5	5.7	80.4
	60.0	90.3	7.7	94.5
Stars	5.0	99.8	93.1	100
	15.0	72.4	46.7	90.2
	30.0	29.8	18.1	37.0
	60.0	4.5	2.5	5.6
NLR	5.0	0.0	0.0	0.1
	15.0	22.6	3.1	37.4
	30.0	46.7	1.8	78.0
	60.0	5.2	0.1	15.6

Table 5.13: Fractional contributions of the various model components to the overall continuum in the best fit model for 3C 270.

Component	Wavelength (μm)	Best fit (%)	Minimum (%)	Maximum (%)
Torus	5.0	1.5	0.1	15.6
	15.0	73.6	10.6	86.7
	30.0	63.8	8.6	100.0
	60.0	13.0	1.6	44.0
Diffuse ISM	5.0	0.3	0.0	0.7
	15.0	6.5	0.9	13.9
	30.0	25.8	1.4	63.7
	60.0	84.0	4.5	100
Stars	5.0	98.2	75.7	100
	15.0	20.0	9.2	74.7
	30.0	10.4	1.3	30.7
	60.0	3.0	0.2	6.6

Table 5.14: Fractional contributions of the various model components to the overall continuum in 3C 270 with a forced torus component.

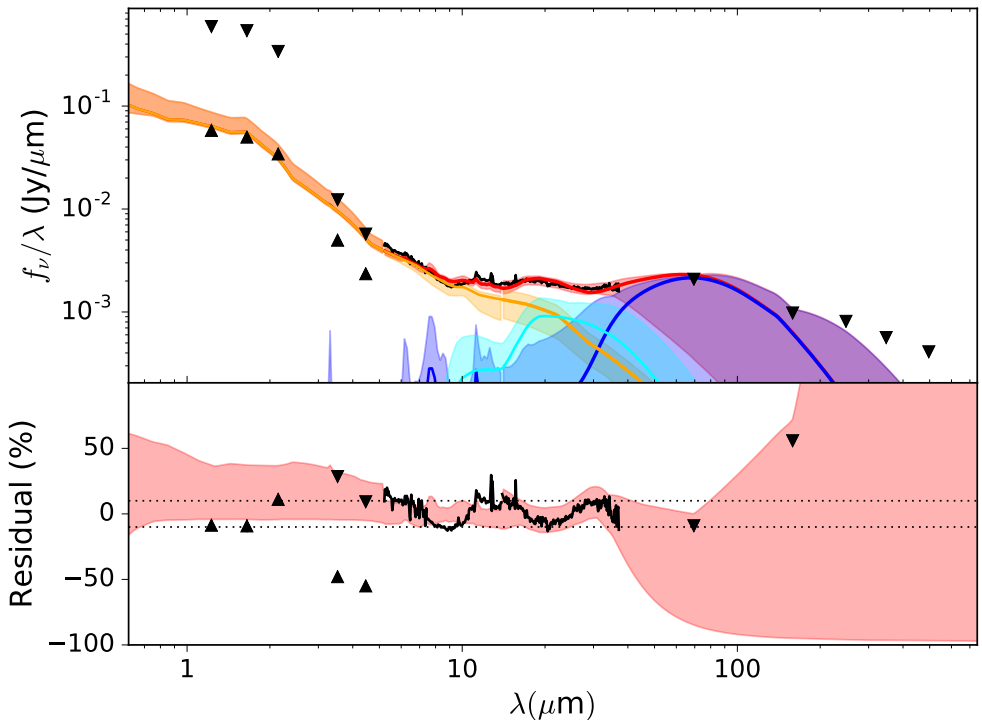

Figure 5.13 Best continuum fit for 3C 270. Model consists of an old stellar population (yellow), NLR (cyan) and diffuse ISM (blue). The total fit is shown in red although in the NIR it appears as orange due to overlap with the stellar population. We have applied aperture correction between the SL and LL regions.Upright triangles represent lower limits from photometry and inverted triangles represent upper limits.

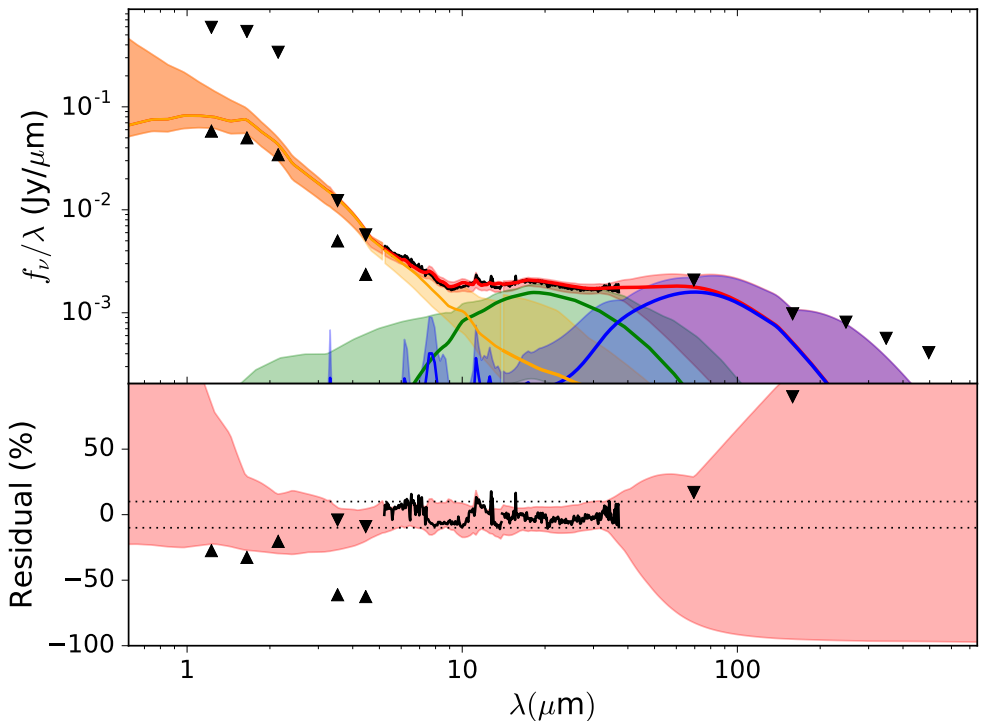

Figure 5.14 Continuum fit for 3C 270 forcing a torus component (green). To ensure maximal contribution from the torus component we excluded the NLR component from Figure 5.13.

5.2.8 M 84

The best fit model for this source contains two AGN components: a hot dust component and an NLR. Unfortunately, we have no MIPS photometry and only one IRAC channel for M 84.

The forced torus component in the forced-torus fit to M 84 is quite reasonable albeit unusually dim with a best-fit AGN luminosity of $1.2 \times 10^{41}\,\mathrm{erg\,s^{-1}}$ (see Table 5.26 and discussion in Section 6.1). However, it has the largest difference in goodness-of-fit out of any of our pairs of models with the best fit having a BIC of 386.9 compared to 444.4 for the forced-torus fit. At least part of that is likely due to forced suppression of the hot dust component. Recall that the purpose of the forced-torus fits was to provide an upper limit on any potential torus contribution. Overall, we conclude that there is likely an optically thin thermal hot dust component and that the bumps in the spectrum toward the MIR are probably a thermal component although likely not in the form of a Nenkova et al. (2002) clumpy torus.

Component	Wavelength (μm)	Best fit (%)	Minimum (%)	Maximum (%)
Diffuse ISM	5.0	0.5	0.1	1.3
	15.0	19.9	8.8	35.7
	30.0	71.5	51.2	94.5
	60.0	99.3	40.3	100
Stars	5.0	37.6	27.4	77.4
	15.0	37.7	9.3	86.9
	30.0	11.3	1.8	35.0
	60.0	0.4	0.0	1.4
NLR	5.0	0.1	0.0	2.8
	15.0	13.2	0.0	27.6
	30.0	10.7	0.0	26.6
	60.0	0.2	0.0	8.4
Hot dust	5.0	61.8	17.0	73.1
	15.0	29.2	5.8	43.5
	30.0	6.6	1.2	10.7
	60.0	0.2	0.0	0.3

Table 5.15: Fractional contributions of the various model components to the overall continuum in the best fit model for M 84.

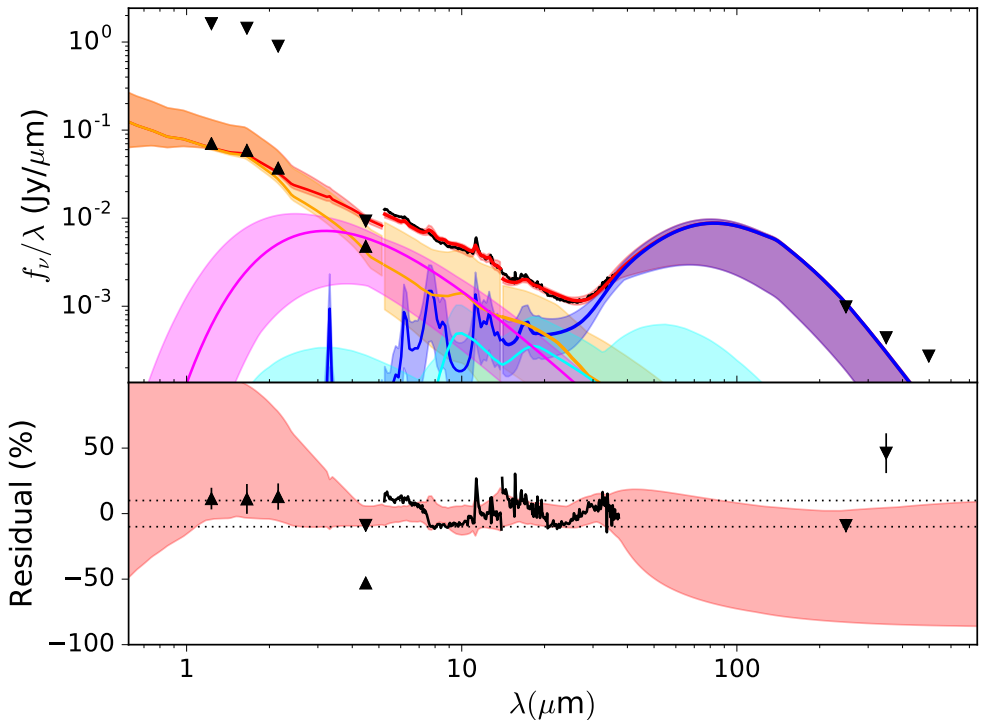

Figure 5.15 Best continuum fit for M 84. Model consists of an old stellar population (yellow), hot dust (pink), NLR (cyan), and diffuse ISM (blue). The total fit is shown in red although in the NIR it appears as orange due to overlap with the stellar population. We have applied aperture correction between the SL and LL regions but this aperture correction was a fitting parameter and it seems to have not been fit well. Upright triangles represent lower limits from photometry and inverted triangles represent upper limits.

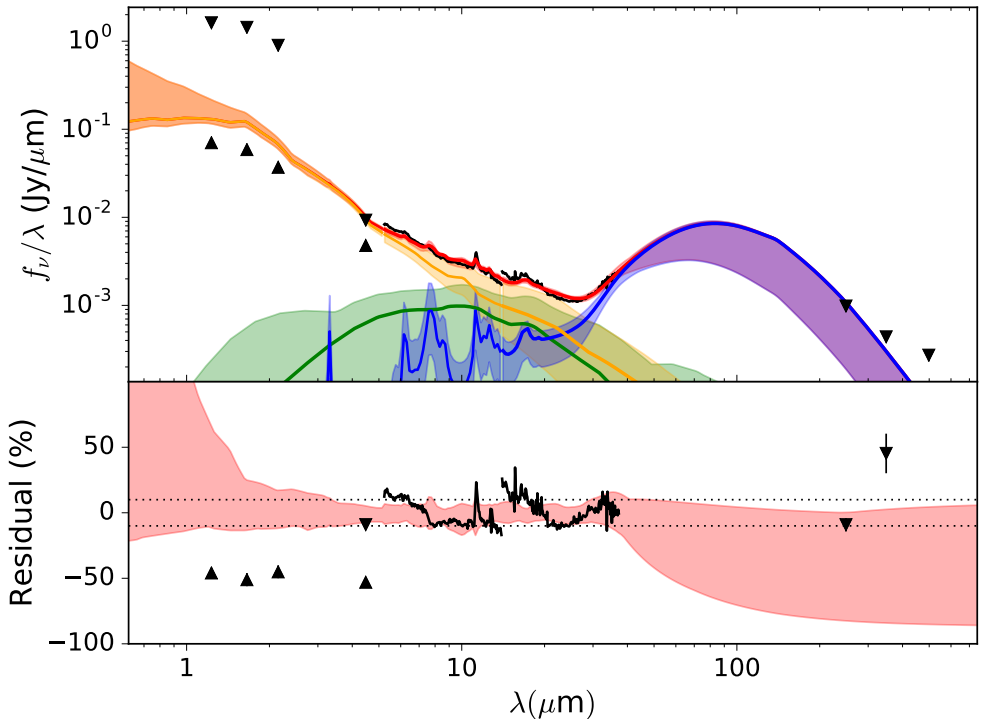

Figure 5.16 Continuum fit for M 84 forcing a torus component (green). To ensure maximal torus component we excluded the NLR and hot dust components seen in Figure 5.15.

Component	Wavelength (μm)	Best fit (%)	Minimum (%)	Maximum (%)
Torus	5.0	9.5	0.0	17.2
	15.0	33.6	0.0	67.4
	30.0	14.1	0.0	46.5
	60.0	0.2	0.0	3.0
Diffuse ISM	5.0	0.3	0.1	0.8
	15.0	16.0	7.0	21.4
	30.0	65.7	45.1	80.8
	60.0	98.9	46.1	100
Stars	5.0	90.2	82.5	100
	15.0	50.4	21.0	95.1
	30.0	20.3	3.7	46.6
	60.0	0.9	0.1	2.2

Table 5.16: Fractional contributions of the various model components to the overall continuum in M 84 with a forced torus component.

5.2.9 M 87

Although every source in our sample has a radio jet and a couple have large scale optical jets, M 87 is the only source in which the power-law spectrum of the inner jet provides a significant contribution to the IR flux. This power law has a best-fit index of $\alpha = 1.2$ (recall that we use the $L_\nu \propto \nu^{-\alpha}$ convention) which is consistent with the optical spectral indices of $\alpha_o \sim 1.0 - 1.2$ Perlman et al. (2001) found for inter-knot regions of the inner jet. The model with a "forced" torus component, shown in Figure 5.18, actually has a marginally lower BIC (392.0) than the otherwise "best" fit (398.7), shown in Figure 5.17, but this must be a fitting artifact as it contributes no flux. This lack of a torus and strong power law spectrum is consistent with findings by Whysong & Antonucci (2004), previously mentioned in Section 1.4.2, that M 87 is weak in IR and that its nuclear IR emission is consistent with a synchrotron spectrum from the base of its jet. Similarly, the absence of a torus is consistent with the upper limits on MIR thermal emission established by Perlman et al. (2007).

Component	Wavelength (μm)	Best fit (%)	Minimum (%)	Maximum (%)
Diffuse ISM	5.0	0.0	0.0	0.4
	15.0	1.3	0.0	8.2
	30.0	4.5	0.0	45.1
	60.0	26.1	0.0	89.5
Stars	5.0	90.3	41.5	98.4
	15.0	65.1	12.8	84.2
	30.0	36.4	7.2	46.5
	60.0	8.1	1.6	10.0

Table 5.17: Fractional contributions of the various model components to the overall continuum in the best fit model of M 87.

Component	Wavelength (μm)	Best fit (%)	Minimum (%)	Maximum (%)
Torus	5.0	0.0	0.0	1.0
	15.0	0.0	0.0	5.7
	30.0	0.2	0.0	31.8
	60.0	0.4	0.0	46.2
Diffuse ISM	5.0	0.0	0.0	0.4
	15.0	0.9	0.6	7.4
	30.0	3.2	2.0	23.4
	60.0	7.3	4.2	25.6
Stars	5.0	89.0	63.0	100
	15.0	64.4	37.8	83.3
	30.0	36.7	19.9	47.0
	60.0	10.3	4.8	12.9

Table 5.18: Fractional contributions of the various model components to the overall continuum in M 87 with a forced torus component.

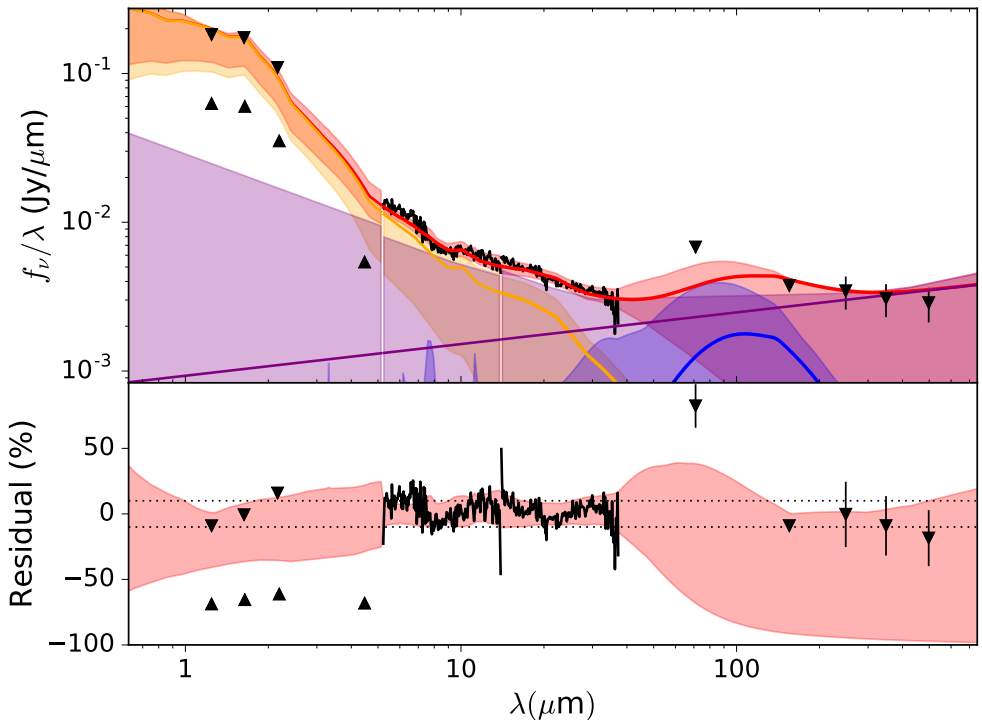

Figure 5.17 Best continuum fit for M 87. Model consists of a power law (purple), an old stellar population (yellow), and diffuse ISM (blue). The total fit is shown in red although in the NIR it appears as orange due to overlap with the stellar population. We have applied aperture correction between the SL and LL regions. Upright triangles represent lower limits from photometry and inverted triangles represent upper limits.

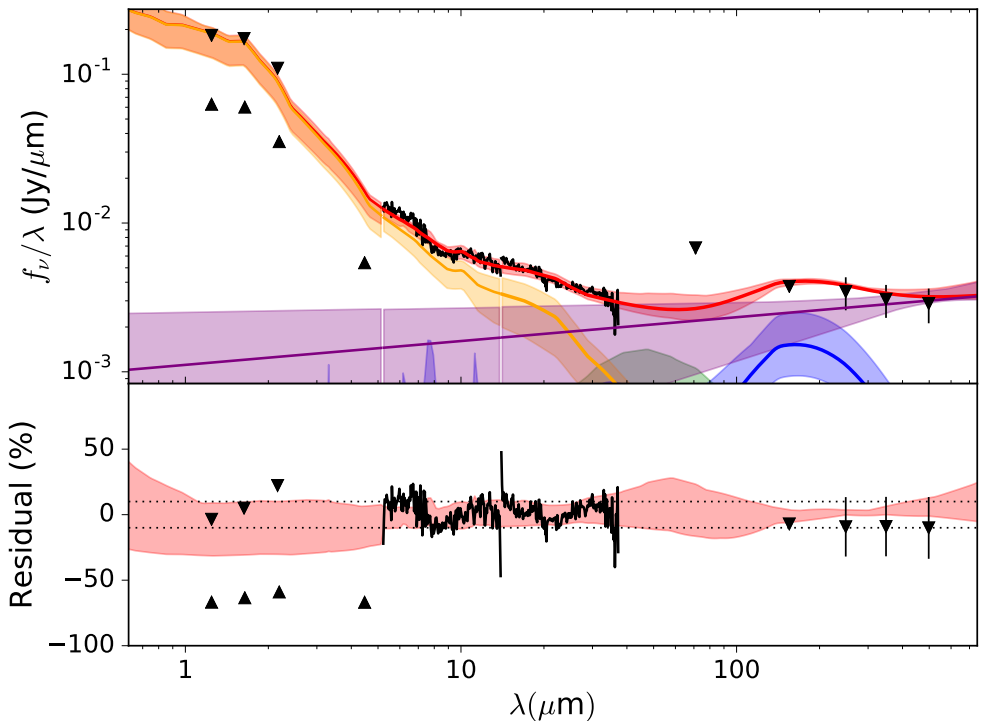

Figure 5.18 Continuum fit for M 87 forcing a torus component (green). To ensure maximal torus component we excluded the NLR component seen in Figure 5.17.

5.2.10 NGC 7052

The model of NGC 7052 with the lowest BIC and the model with a forced torus have very similar goodness-of-fit with the best fit having a BIC of 425.7 and the forced-torus fit having a BIC of 429.8. However, inspection of the forced torus fit shows that it is unusually cold for a circumnuclear torus. Indeed, *HST* images of NGC 7052 by Verdoes Kleijn et al. (1999) show a promising candidate for such a cold thermal source in the form of a kpc-scale dust disk which crosses the core region just off to the side of our line-of-sight into the nucleus. Overall, we conclude that a warm thermal component, such as a torus, is unnecessary to explain the IRS flux.

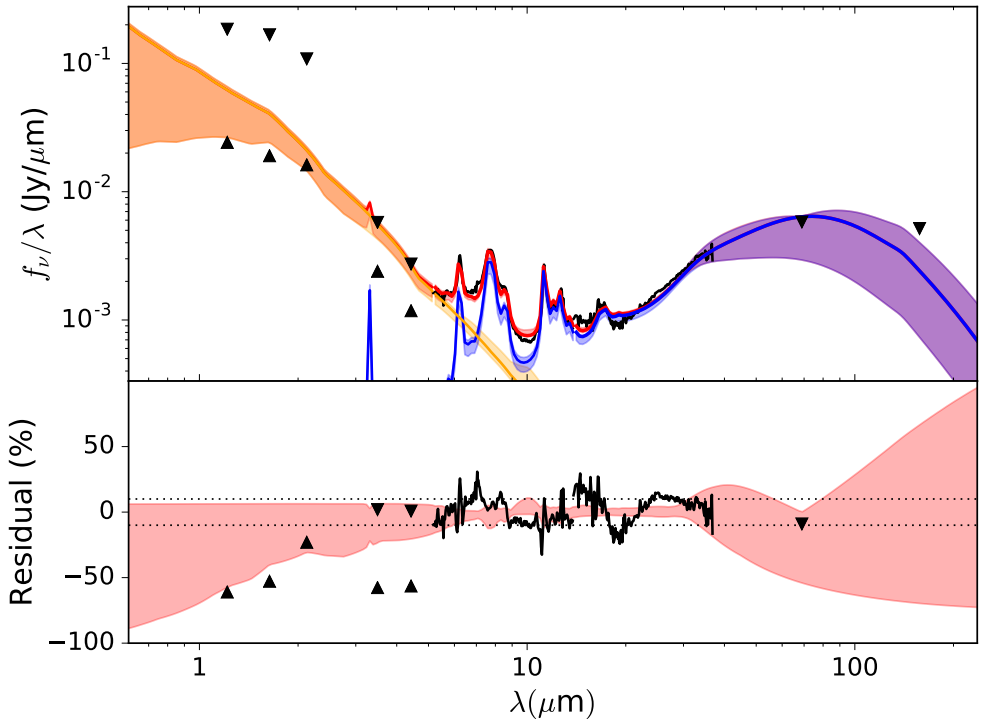

Figure 5.19 Best continuum fit for NGC 7052. Model consists of an old stellar population (yellow) and diffuse ISM (blue). The total fit is shown in red although in the NIR it appears as orange due to overlap with the stellar population. Upright triangles represent lower limits from photometry and inverted triangles represent upper limits.

Component	Wavelength (μm)	Best fit (%)	Minimum (%)	Maximum (%)
Diffuse ISM	5.0	5.3	4.3	5.7
	15.0	90.8	79.3	92.6
	30.0	99.6	92.4	100
	60.0	100.0	50.8	100
Stars	5.0	94.7	77.6	100
	15.0	9.2	8.5	21.9
	30.0	0.4	0.4	3.9
	60.0	0.0	0.0	0.5

Table 5.19: Fractional contributions of the various model components to the overall continuum in the best fit model for NGC 7052.

Component	Wavelength (μm)	Best fit (%)	Minimum (%)	Maximum (%)
Torus	5.0	3.9	0.0	9.5
	15.0	33.0	5.1	52.3
	30.0	60.9	14.8	92.4
	60.0	32.3	3.0	79.2
Diffuse ISM	5.0	5.3	4.1	6.3
	15.0	52.4	42.5	73.6
	30.0	35.8	14.6	83.8
	60.0	67.2	8.9	100
Stars	5.0	90.9	87.2	100
	15.0	14.6	7.2	26.1
	30.0	3.3	0.4	4.2
	60.0	0.5	0.0	0.6

Table 5.20: Fractional contributions of the various model components to the overall continuum in NGC 7052 with a forced torus component.

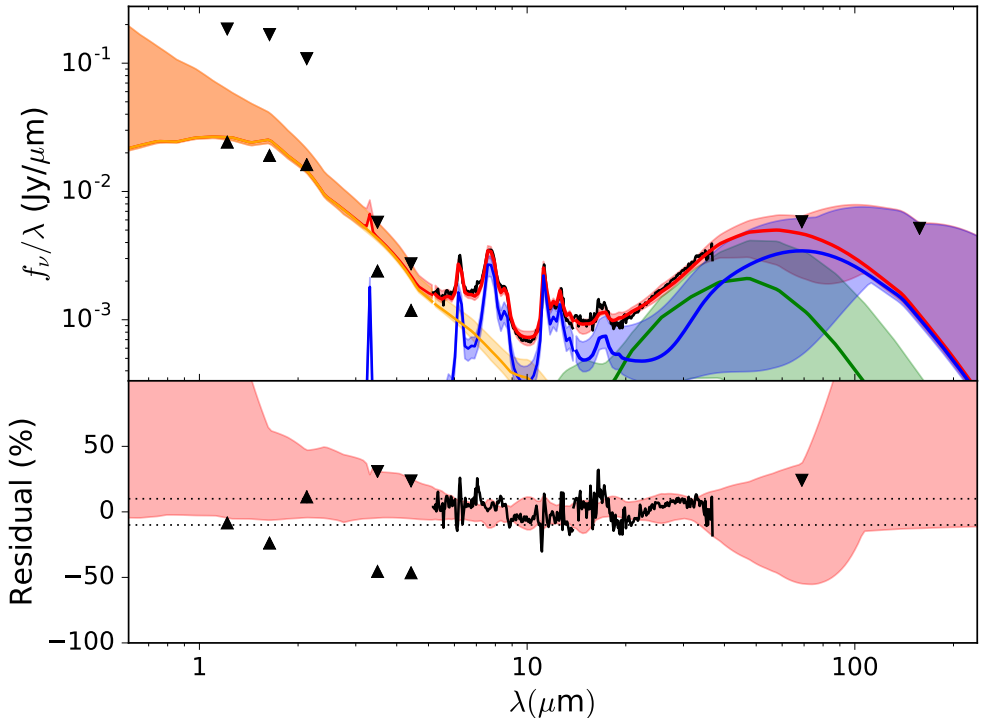

Figure 5.20 Continuum fit for NGC 7052 forcing a torus component (green). Model is otherwise the same as in Figure 5.20.

5.2.11 Results summary

Some of the stellar age parameters for the best fits, shown in Table 5.21, are unusually low for the various SFR estimates. This could be explained by those sources having recently quieted after a starburst, indeed Das et al. (2005) claim something similar for NGC 3801, but it seems improbable that so many of such a small sample would be within 2 Gyr of the end of a starburst and NGC 3801 is not one of the sources with these low stellar ages. The fits with a forced torus, shown in Table 5.22, are better in this regard with only 3C 66B and M 87 having this unusual combination. We do not put much stock in this result because stellar ages are generally poorly constrained by infrared data since young stars are brightest at shorter wavelengths and as mentioned in Section 5.1.1 the GRASIL stellar population model assumes a single Gyr-long starburst followed by passive evolution which may not be a good approximation in these galaxies. This would likely be clearer with more NIR spectrometry such as that which will be possible with the instruments aboard the *James*

Source	Stellar Age (Gyr)	SFR ($M_\odot\,yr^{-1}$)
NGC 315	$7.7^{+3.0}_{-4.9}$	$0.24^{+0.15}_{-0.081}$
3C 31	$1.7^{+0.4}_{-0.7}$	$0.88^{+0.14}_{-0.28}$
NGC 541	$2.3^{+0.4}_{-0.4}$	$0.12^{+0.034}_{-0.017}$
3C 66B	$1.0^{+0.3}_{-0.2}$	$0.017^{+0.0038}_{-0.0035}$
NGC 3801	$9.4^{+3.0}_{-5.0}$	$0.35^{+0.087}_{-0.074}$
NGC 3862	$0.9^{+0.2}_{-0.3}$	$0.20^{+0.084}_{-0.038}$
3C 270	$1.0^{+0.2}_{-0.2}$	$0.044^{+0.0058}_{-0.014}$
M 84	$0.4^{+0.1}_{-0.0}$	$0.034^{+0.0057}_{-0.0099}$
M 87	$1.0^{+0.3}_{-0.2}$	$0.0026^{+0.0031}_{-0.0021}$
NGC 7052	$0.1^{+0.0}_{-0.0}$	$0.67^{+0.052}_{-0.061}$

Table 5.21: Best fit parameters for the stellar population component.

Webb Space Telescope and optical spectroscopy (especially in blue) would help characterise the population of young stars.

The diffuse ISM components of the two model sets, the best fit models shown in Table 5.23 and the forced-torus models shown in Table 5.24, show lower limits on their interstellar radiation fields, PAH fractions, and ISM luminosities which are generally consistent between the two sets with the exception of M 87 which shows an improbably weak radiation field and significantly higher ISM luminosity in the forced-torus model.

The fit parameters for the torus, when present (forced-torus models and NGC 315) are shown in Tables 5.25 and 5.26. Of particular interest is the low inclination of NGC 3801, the large half-opening angle and high escape probability of NGC 3801, NGC 3862, and M 84. These are unusual for sources in which we can't see broad lines from the central engine. The masses of obscuring material in the forced-torus fits to NGC 3801 and M 84 are remarkably small compared to the others with both being $\sim 10^{-3}\,M_\odot$. And finally the power law indices of the cloud distributions in the forced-torus models are inconsistent with the silicate line ratios in several sources, especially three previously mentioned in this paragraph: NGC 3801, NGC 3862, and M 84. When considered together these issues suggest that the upper limits

Source	Stellar Age (Gyr)	SFR ($M_\odot\,yr^{-1}$)
3C 31	$7.9^{+3.5}_{-3.5}$	$0.73^{+0.22}_{-0.21}$
NGC 541	$7.4^{+4.1}_{-3.6}$	$0.12^{+0.026}_{-0.013}$
3C 66B	$1.0^{+0.2}_{-0.2}$	$0.00054^{+0.0022}_{-0.00053}$
NGC 3801	$6.7^{+5.6}_{-6.4}$	$0.3^{+0.087}_{-0.041}$
NGC 3862	$2.5^{+6.8}_{-1.5}$	$0.21^{+0.081}_{-0.042}$
3C 270	$8.2^{+3.6}_{-3.8}$	$0.029^{+0.013}_{-0.011}$
M 84	$3.2^{+1.5}_{-0.9}$	$0.022^{+0.0045}_{-0.0028}$
M 87	$1.1^{+0.2}_{-0.3}$	$0.011^{+0.0011}_{-0.00081}$
NGC 7052	$9.8^{+2.2}_{-2.9}$	$0.47^{+0.095}_{-0.062}$

Table 5.22: Best fit parameters for the stellar population component in fits forcing a torus.

Source	$u_{\rm min}$	$q_{\rm PAH}$ (%)	ISM Luminosity ($10^{41}\,erg\,s^{-1}$)
NGC 315	$8.1^{+9.7}_{-5.2}$	$2.46^{+1.24}_{-0.9}$	$52.0^{+34.0}_{-18.0}$
3C 31	$2.7^{+2.4}_{-1.1}$	$2.59^{+1.05}_{-0.3}$	$200.0^{+31.0}_{-63.0}$
NGC 541	$10.6^{+6.5}_{-5.4}$	$3.82^{+0.55}_{-0.8}$	$26.0^{+7.7}_{-3.7}$
3C 66B	$6.3^{+5.4}_{-3.1}$	$1.13^{+0.85}_{-0.4}$	$3.8^{+0.85}_{-0.77}$
NGC 3801	$1.9^{+2.4}_{-0.8}$	$3.40^{+0.83}_{-0.6}$	$78.0^{+19.0}_{-17.0}$
NGC 3862	$9.1^{+10.0}_{-6.4}$	$3.54^{+0.70}_{-0.9}$	$44.0^{+19.0}_{-8.4}$
3C 270	$14.7^{+6.4}_{-7.8}$	$1.28^{+0.71}_{-0.4}$	$9.8^{+1.3}_{-3.2}$
M 84	$9.8^{+7.7}_{-2.8}$	$1.55^{+0.62}_{-0.3}$	$7.5^{+1.3}_{-2.2}$
M 87	$15.1^{+6.8}_{-12.5}$	$2.38^{+1.49}_{-1.3}$	$0.57^{+0.69}_{-0.46}$
NGC 7052	$16.4^{+4.8}_{-4.1}$	$2.45^{+0.23}_{-0.2}$	$150.0^{+11.0}_{-14.0}$

Table 5.23: ISM component best fit parameters. Recall from Section 5.1.1 that $q_{\rm PAH}$ is the mass fraction of polycyclic aromatic hydrocarbons relative to the total dust mass and $U_{\rm min}$ is the lower limit of the interstellar radiation field as a scaling of that in the solar neighbourhood.

Source	$u_{\rm min}$	$q_{\rm PAH}$ (%)	ISM Luminosity ($10^{41}\,{\rm erg\,s^{-1}}$)
3C 31	$3.4^{+3.7}_{-1.4}$	$3.11^{+1.07}_{-0.6}$	$160.0^{+50.0}_{-46.0}$
NGC 541	$14.7^{+4.1}_{-7.6}$	$3.95^{+0.44}_{-0.6}$	$26.0^{+5.8}_{-2.9}$
3C 66B	$7.7^{+7.0}_{-4.3}$	$2.24^{+1.55}_{-1.2}$	$0.12^{+0.49}_{-0.12}$
NGC 3801	$3.5^{+2.5}_{-2.1}$	$3.89^{+0.52}_{-0.8}$	$67.0^{+19.0}_{-9.2}$
NGC 3862	$10.0^{+8.9}_{-6.0}$	$3.53^{+0.69}_{-0.9}$	$46.0^{+18.0}_{-9.4}$
3C 270	$13.9^{+7.7}_{-7.7}$	$2.14^{+1.22}_{-0.9}$	$6.4^{+2.8}_{-2.3}$
M 84	$17.9^{+4.5}_{-5.1}$	$1.34^{+0.38}_{-0.3}$	$4.9^{+1.0}_{-0.62}$
M 87	$0.1^{+0.0}_{-0.0}$	$1.62^{+1.09}_{-0.8}$	$2.5^{+0.24}_{-0.18}$
NGC 7052	$17.4^{+4.5}_{-7.5}$	$3.75^{+0.55}_{-0.6}$	$100.0^{+21.0}_{-14.0}$

Table 5.24: ISM component best fit parameters with a forced torus component.

the forced-torus fits place on any possible torus component in NGC 3801, NGC 3862, and M 84 are inconsistent with independent observations.

Overall, we find no evidence for a warm obscuring torus in six of our ten sources and we find convincing evidence for a torus in one of the ten (NGC 315). We have three more sources in which we find strong evidence for some warm MIR structure but cannot conclude that said structure is consistent with the Nenkova et al. (2002) clumpy torus model. We summarise our conclusions as to the presence or absence of each of our model components for each source in Table 5.27 and we compare the BIC of the best-fit models to those with a forced torus component in Table 5.28. The main reason for inconclusive results is the fitting degeneracy between torus, NLR, and hot dust.

Source	σ (deg)	Y	N_0	τ_V	q	Inclination (deg)
NGC 315*	$59.6^{+7.6}_{-12.2}$	$21.4^{+24.9}_{-6.9}$	$11.9^{+2.2}_{-3.0}$	$131.2^{+47.4}_{-29.6}$	$1.34^{+0.60}_{-0.89}$	$63.4^{+18.6}_{-25.9}$
3C 31	$53.9^{+11.3}_{-16.5}$	$34.3^{+42.4}_{-22.0}$	$10.6^{+3.1}_{-3.8}$	$70.5^{+122.2}_{-40.8}$	$1.88^{+0.64}_{-1.00}$	$50.5^{+27.6}_{-33.3}$
NGC 541	$49.8^{+14.1}_{-17.3}$	$39.5^{+39.4}_{-24.8}$	$10.2^{+3.3}_{-4.3}$	$147.5^{+104.5}_{-93.3}$	$1.73^{+0.75}_{-1.03}$	$52.9^{+25.8}_{-34.8}$
3C 66B	$55.1^{+10.6}_{-13.4}$	$24.3^{+21.5}_{-5.8}$	$11.4^{+2.6}_{-3.6}$	$223.7^{+53.8}_{-66.7}$	$1.00^{+0.70}_{-0.68}$	$70.0^{+14.0}_{-21.1}$
NGC 3801	$39.1^{+19.3}_{-16.0}$	$45.9^{+36.8}_{-32.7}$	$3.9^{+5.3}_{-2.1}$	$27.0^{+137.0}_{-14.5}$	$2.38^{+0.46}_{-1.08}$	$31.2^{+29.5}_{-21.4}$
NGC 3862	$39.8^{+19.7}_{-17.2}$	$47.0^{+36.1}_{-32.9}$	$6.6^{+5.3}_{-3.7}$	$103.6^{+125.3}_{-69.9}$	$2.25^{+0.54}_{-1.16}$	$41.1^{+31.6}_{-28.3}$
3C 270	$58.3^{+8.3}_{-12.8}$	$15.5^{+36.4}_{-5.4}$	$11.9^{+2.3}_{-3.3}$	$136.5^{+84.0}_{-44.5}$	$1.58^{+0.72}_{-1.02}$	$63.7^{+18.6}_{-29.1}$
M 84	$42.9^{+18.2}_{-18.7}$	$34.3^{+43.5}_{-24.3}$	$6.9^{+4.8}_{-3.7}$	$43.2^{+118.3}_{-26.4}$	$2.50^{+0.35}_{-0.74}$	$44.1^{+31.5}_{-30.4}$
M 87	$55.4^{+10.5}_{-17.1}$	$78.3^{+15.4}_{-20.6}$	$11.5^{+2.5}_{-3.6}$	$200.9^{+67.1}_{-74.6}$	$0.48^{+0.42}_{-0.34}$	$66.4^{+16.7}_{-27.5}$
NGC 7052	$64.4^{+4.1}_{-6.7}$	$90.4^{+7.0}_{-10.5}$	$12.5^{+1.8}_{-2.5}$	$56.8^{+25.0}_{-16.2}$	$0.27^{+0.26}_{-0.20}$	$56.2^{+21.6}_{-18.5}$

Table 5.25: Best fit parameters for forced torus components. σ is the angular scale height of the torus, Y is the radial extent of the torus in units of the dust sublimation radius, N_0 is the number of clouds along an equatorial line-of-sight, τ_V is the optical depth of a single cloud and q is the power law index of the radial distribution of clouds (see Section 4.2.3 for more). The inclination is defined such that 0° is pole-on and 90° is edge-on. *Recall that NGC 315 favours a torus component; it is not forced.

Source	Half-Opening Angle (deg)	Escape Probability (%)	Mass ($M_\odot$)	Radius (pc)	AGN Luminosity (10^{41} erg s^{-1})
NGC 315*	$10.5^{+6.2}_{-2.8}$	$0.02^{+0.60}_{-0.0}$	$2.2^{+1.4}_{-0.92}$	$0.93^{+1.2}_{-0.34}$	$110.0^{+34.0}_{-21.0}$
3C 31	$14.7^{+15.7}_{-5.7}$	$0.77^{+24.51}_{-0.7}$	$0.044^{+0.088}_{-0.027}$	$0.4^{+0.54}_{-0.26}$	$9.1^{+4.9}_{-2.8}$
NGC 541	$18.4^{+20.7}_{-8.7}$	$1.35^{+40.28}_{-1.3}$	$0.045^{+0.11}_{-0.029}$	$0.32^{+0.35}_{-0.21}$	$4.5^{+2.8}_{-1.5}$
3C 66B	$13.0^{+10.4}_{-4.7}$	$0.02^{+0.55}_{-0.0}$	$0.42^{+0.26}_{-0.15}$	$0.31^{+0.27}_{-0.09}$	$9.1^{+3.3}_{-1.6}$
NGC 3801	$44.6^{+15.6}_{-19.2}$	$67.28^{+32.26}_{-54.6}$	$0.0013^{+0.0048}_{-0.0008}$	$0.3^{+0.38}_{-0.22}$	$4.0^{+3.2}_{-2.7}$
NGC 3862	$36.3^{+21.1}_{-19.7}$	$29.65^{+67.43}_{-28.9}$	$0.03^{+0.11}_{-0.023}$	$0.62^{+0.93}_{-0.48}$	$20.0^{+20.0}_{-18.0}$
3C 270	$11.0^{+7.8}_{-3.2}$	$0.03^{+1.37}_{-0.0}$	$0.087^{+0.064}_{-0.038}$	$0.19^{+0.47}_{-0.075}$	$9.0^{+2.9}_{-1.8}$
M 84	$31.4^{+23.5}_{-16.5}$	$16.36^{+77.09}_{-16.0}$	$0.00079^{+0.0012}_{-0.00048}$	$0.13^{+0.21}_{-0.094}$	$1.2^{+0.82}_{-0.56}$
M 87	$12.6^{+15.7}_{-4.4}$	$0.04^{+1.44}_{-0.0}$	$0.098^{+0.27}_{-0.096}$	$0.13^{+0.14}_{-0.11}$	$0.21^{+0.58}_{-0.21}$
NGC 7052	$8.4^{+2.2}_{-1.4}$	$0.02^{+0.15}_{-0.0}$	$14^{+9.1}_{-5.1}$	$2.3^{+0.34}_{-0.34}$	$41.0^{+8.2}_{-6.6}$

Table 5.26: More best fit parameters for forced torus components. *Recall that NGC 315 favours a torus component; it is not forced.

Source	Evidence for torus	Evidence for power law	Evidence for NLR	Evidence for hot dust	Warm Component?
NGC 315	Y	N	N	N	Y
3C 31	N	N*	N	N	N
NGC 541	N	N	N	N	N
3C 66B	I	N*	I	I	Y
NGC 3801	N	N	I	N	I
NGC 3862	N	N*	N	N	N
3C 270	I/Y	N	I/N	N	Y
M 84	I	N	I	I	Y
M 87	N	Y*	N	N	N
NGC 7052	N	N	N	N	N

Table 5.27: Summary of best fit results. Results in which we are reasonably confident are marked with "Y" (for yes) if present or "N" (for no) if not. Results which are more ambiguous are denoted with "I" (for inconclusive), although we follow the 3C 270 results with a marker describing the model which we favour. The NLR and torus are both considered a warm component. *These sources have known optical or IR jets so were checked for a power-law component.

Source	Best fit BIC	Forced torus BIC
NGC 315	420.3	-
3C 31	403.5	425.7
NGC 541	380.5	408.7
3C 66B	472.3	506.8
NGC 3801	423.5	453.7
NGC 3862	391.9	420.3
3C 270	410.7	424.9
M 84	386.9	444.4
M 87	398.7	392.0
NGC 7052	425.7	429.8

Table 5.28: BIC for the the best fit and forced torus fit in each source. As stated in Section 5.2.9, we do not favour the presence of a torus in M 87 despite the lower BIC because the torus component does not contribute to the flux when forced.

Chapter 6

Discussion

6.1 Comparison to previous work

Leipski et al. (2009) found an IRS band thermal excess in four of the fifteen FR-I radio galaxies in their sample. Six of our ten sources — 3C 31, 3C 66B, NGC 3862, 3C 270, M 84, and M 87 — overlap with their sample. Of those, they found thermal MIR excess in the nucleus of only 3C 270 which they tentatively attribute to an obscuring torus. We find that this thermal MIR excess in 3C 270 is better described by a NLR component. However, due to the bias noted in Section 5.2.7, in which the relative simplicity of the NLR component compared to the torus component biases the BIC against a torus component, this disagreement is quite minor. They also found a MIR excess in the other sources in which we find a warm thermal component, 3C 66B and M 84, however they attribute these excesses to other effects. They attribute the MIR excess in 3C 66B to non-thermal emission and they attribute the excess in M 84 to starburst activity. We can rule out a starburst origin in M 84 because all our estimates of the SFR in M 84 agree that SFR $\lesssim 0.1\,\mathrm{M}_\odot$.

Recall that Elitzur & Shlosman (2006) found that hydromagnetic disk winds off sources with bolometric luminosities $L_{\mathrm{bol}} \lesssim 10^{42}\,\mathrm{erg\,s^{-1}}$ could not sustain a clumpy obscuring torus. In the torus model parameters continuum fits with a forced torus component, shown in Table

5.26, NGC 315, NGC 3862, and NGC 7052 have best-fit AGN luminosities $> 10^{42}\,\mathrm{erg\,s^{-1}}$ and 3C 31, 3C 66B, and 3C 270 come in just under that at $\sim 9 \times 10^{41}\,\mathrm{erg\,s^{-1}}$. This suggests that the other four sources which all have bolometric luminosities significantly below $10^{42}\,\mathrm{erg\,s^{-1}}$, including M 84 which we previously considered inconclusive, are not likely to host a clumpy AGN-wind-driven torus. Note, however, that this does not prohibit other obscuring structures.

Buttiglione et al. (2010) proposed various line ratios with which to distinguish between low-excitation and high-excitation sources. The measure with the clearest distinction betwen the two populations was the Excitation Index (EI), the formula for which we show in Equation 6.1. For low-excitation sources EI $\lesssim 0.95$ and for high excitation sources EI $\gtrsim 0.95$. Hu et al. (2016) calculated excitation indices for the 3C catalogue using line fluxes measured by Buttiglione et al. (2009) and we include those 3C sources which are also in our sample in Table 6.1 and find that all but NGC 315 and NGC 541 are low-excitation sources. We classify those remaining two as extremely low excitation radio galaxies (ELERGs) based on their unusually low [OIII]/Hβ of 0.57 and 0.67, respectively, which is consistent with the [OIII]/H$\beta \sim 0.5$ indicative of extremely low-excitation sources. Capetti et al. (2011) describe extremely low-excitation galaxies as "radio relics". They define radio relics as sources which recently experienced a drop in nuclear activity — perhaps this is the case in NGC 315 and NGC 541. We see no issues with this interpretation for NGC 541 but NGC 315 shows a warm thermal MIR component. This warm thermal componenet in NGC 315 is well fit by a clumpy torus, and is thus indicative of a high-excitation galaxy, yet its optical emission line ratios are those of an extremely low-excitation galaxy. It is unclear how to reconcile these; we hypothesise that the warm dust cooling is occurring on a longer time-scale than [OIII] recombination, perhaps because the warm dust structure is much larger than the emission-line nucleus. It may be related to the kpc-scale dust disk seen in *HST* images by Verdoes Kleijn et al. (1999). This will require further research.

$$\mathrm{EI} = \log \frac{[\mathrm{OIII}]}{\mathrm{H}\beta} - \frac{1}{3}\left(\log \frac{[\mathrm{NII}]}{\mathrm{H}\alpha} + \log \frac{[\mathrm{SII}]}{\mathrm{H}\alpha} + \log \frac{[\mathrm{OI}]}{\mathrm{H}\alpha} \right) \tag{6.1}$$

Source	$L_{\mathrm{H}\alpha}$	$L_{\mathrm{H}\beta}$	$L_{[\mathrm{NII}]}$	$L_{[\mathrm{SII}]}$	$L_{[\mathrm{OI}]}$	EI	Class
NGC 315*	4.19	4.80	7.70	2.12	2.46	-0.154	ELERG
3C 31	6.76	1.01	6.69	4.66	0.946	0.797	LERG
NGC 541	4.58	1.32	2.97	0.57	1.10	-0.484	ELERG
3C 66B	12.88	1.54	31.16	7.21	3.35	0.746	LERG
NGC 3801	0.98	0.06	0.96	0.57	0.17	0.721	LERG
NGC 3862	4.79	1.29	6.94	3.16	1.05	0.313	LERG
3C 270†	0.14	< 0.15	0.10	< 0.12	0.07	0.048	LERG
M 84	0.83	0.08	1.06	0.72	0.19	0.478	LERG
M 87	3.16	0.54	7.34	4.58	1.14	0.233	LERG
NGC 7052	7.62	1.65	8.86	3.62	0.93	0.612	LERG

Table 6.1: Classification based on excitation indices. All luminosities in units of $10^{39}\,\mathrm{erg\,s^{-1}}$. $L_{[\mathrm{OIII}]}$ given in Table 6.3. Line luminosities and excitation indices for galaxies in 3C (3C 31, 3C 66B, NGC 3862, 3C 270, M 84, and M 87) by Hu et al. (2016). Line luminosities for NGC 541, NGC 3801, and NGC 7052 by Constantin et al. (2015). Hα and [OI] line luminosities for NGC 315 by Cid Fernandes et al. (2004), Hβ by Richings et al. (2011), and [NII] and [SII] by Balmaverde et al. (2016). Classification cutoff given by Buttiglione et al. (2010) as EI $\lesssim 0.95$ for low excitation galaxies. Hu et al. (2016) calculated EI using line fluxes by Buttiglione et al. (2009). *Cid Fernandes et al. (2004) and Richings et al. (2011) use a different cosmology than us, so we have corrected their luminosities for our distance. Additionally, since the luminosities are from different instruments, systematic errors in our calculations are likely significant and difficult to quantify. †Buttiglione et al. (2010) removed this source from their data due to a misplaced SDSS fiber and so it is unreliable.

We compare our continuum fitting results to 1.4 GHz radio luminosity density $L_{\nu,\,1.4\,\mathrm{GHz}}$, estimated black hole mass M_{BH}, and core-extended brightness ratio R_c in Table 6.2. R_c is a indicator for AGN orientation in torus models. The presence or absence of a MIR thermal component appears to be independent of $L_{\nu,\,1.4\,\mathrm{GHz}}$, R_c as well as redshift but there may be some dependence on black hole mass. No source in the sample with an estimated black hole mass below $7 \times 10^8\,\mathrm{M}_\odot$ has a MIR thermal component and only two sources (3C 31 and M 87) without a MIR thermal component have black hole masses above that. It is likely that this apparent dependence is spurious (i.e., an effect of the small sample size) but it may not

be.

Source	$L_{\nu,\,1.4\,\mathrm{GHz}}$ ($10^{31}\,\mathrm{erg\,s^{-1}\,Hz^{-1}}$)	M_{BH} ($10^{8}\,\mathrm{M_{\odot}}$)	$\log_{10} R_c$
NGC 315	1.26	14.6	-0.39
3C 66B	8.71	18.6	-1.29
M 84	0.224	7.30	-1.18
3C 270	2.51	7.75	-1.44
3C 31	3.24	9.24	-1.34
NGC 541	0.871	2.03	-
NGC 3801	0.309	1.53	-
NGC 3862	5.62	4.66	-1.00
M 87	7.94	22.5	-1.24
NGC 7052	0.110	3.62	-0.22

Table 6.2: 1.4 GHz radio luminosity density, black hole mass estimate, and logarithm of core-extended brightness ratio (an indicator for AGN orientation in torus models) for FR-I AGN in our sample. Sources divided based on the presence (top) or abscence (bottom) of a MIR thermal component in the best fit for that source. $L_{\nu,\,1.4\,\mathrm{GHz}}$ by Condon & Broderick (1988), M_{BH} by Noel-Storr et al. (2007) based on a relation by Merritt & Ferrarese (2001), and $\log_{10} R_c$ by Kharb & Shastri (2004). We notice no dependence of the presence of a thermal MIR component on $L_{\nu,\,1.4\,\mathrm{GHz}}$, R_c, or redshift (see Table 3.1). Sources with a thermal MIR component seem to have larger M_{BH} as a group however 3C 31 and M 87 do not fit with that distinction and we can think of no clear reason why this should be the case.

Since the luminosity of a given high-ionisation line will be dependent on both the degree of ionisation and the overall abundance of the element in question (see Spinoglio & Malkan (1992) for more), we show the line ratio of our fitted [OIV] luminosities to archival [OIII] luminosities for each of our sample galaxies in Table 6.3. We also include for comparison a collection of [OIV]/[OIII] line ratios for high-luminosity radio galaxies and Seyfert galaxies in Tables 6.4-6.7. This ratio is independent of the oxygen abundance in the line-emitting gas and as such provides a better indication of the ionisation state of the gas. However, most of the ratios for our sample are upper limits because no [OIV] was detected in those sources. The two FR-I sources in which we detected [OIV] emission, 3C 31 and M 84, are inconsistent with broad-line radio galaxies and quasars in the Haas et al. (2005) sample and consistent with obscured sources (e.g., Seyfert 2) in the Baum et al. (2010) Seyfert sample. However,

Source	$L_{[\mathrm{OIV}]}$ 26 μm ($10^{39}\,\mathrm{erg\,s^{-1}}$)	$L_{[\mathrm{O\,III}]}$ ($10^{39}\,\mathrm{erg\,s^{-1}}$)	$\frac{L_{[\mathrm{O\,IV}]}}{L_{[\mathrm{O\,III}]}}$	[O III] reference
NGC 315	< 4.98	2.75	< 1.81	Balmaverde et al. (2016)
3C 31	$3.46^{+0.72}_{-0.77}$	2.88	$1.20^{+0.25}_{-0.27}$	Buttiglione et al. (2010)
NGC 541	< 6.28	0.886	< 7.09	Constantin et al. (2015)
3C 66B	< 3.10	11.2	< 0.28	Buttiglione et al. (2010)
NGC 3801	< 3.20	0.146	< 22.0	Sikora et al. (2013)
NGC 3862	< 4.12	1.58	< 2.60	Buttiglione et al. (2010)
3C 270	< 0.924	0.794	< 1.16	van der Wolk et al. (2010b)
M 84*	$0.318^{+0.038}_{-0.064}$	0.88	$0.36^{+0.04}_{-0.07}$	Richings et al. (2011)
M 87	< 0.751	1.17	< 0.64	Balmaverde et al. (2016)
NGC 7052	< 7.60	2.75	< 2.76	Baldi & Capetti (2009)

Table 6.3: Oxygen line ratios in our sample of FR-I sources for comparison to a set of high-power radio AGN by Haas et al. (2005) in Table 6.4 and a set of Seyfert galaxies and LINERs by Baum et al. (2010) in Tables 6.5-6.7. *Richings et al. (2011) uses a different cosmology from ours so we have corrected their $L_{[\mathrm{OIII}]}$ to our distance.

there is considerable overlap between the source classes (see Figure 6.1).

Source	Class	$L_{[\mathrm{OIV}]}$ 26 μm ($10^{39}\,\mathrm{erg\,s^{-1}}$)	$L_{[\mathrm{O\,III}]}$ ($10^{39}\,\mathrm{erg\,s^{-1}}$)	$\frac{L_{[\mathrm{O\,IV}]}}{L_{[\mathrm{O\,III}]}}$
3C 79	N	1380	3890	0.3548
3C 303.1	N	204.2	512.9	0.3981
3C 321	N	436.5	1778	0.2454
3C 381	N	154.9	251.2	0.6166
3C 459	N	295.1	1380	0.2138
3C 109	B	812.8	20890	0.03890
3C 249.1	Q	724.4	24550	0.02951
3C 323.1	Q	363.1	10470	0.03467
3C 445	B	42.66	1288	0.03311

Table 6.4: Oxygen line ratios in a set of high-power radio AGN by Haas et al. (2005) for comparison to Table 6.3. N refers to narrow-line radio galaxies, B refers to broad-line radio galaxies, and Q refers to quasars.

Source	Class	$L_{[\mathrm{OIV}]}$ 26 μm ($10^{39}\,\mathrm{erg\,s^{-1}}$)	$L_{[\mathrm{O\,III}]}$ ($10^{39}\,\mathrm{erg\,s^{-1}}$)	$\frac{L_{[\mathrm{O\,IV}]}}{L_{[\mathrm{O\,III}]}}$
CGCG 381-051	HII	35.481	37.014	0.959
M+0-29-23	HII	251.189	321.581	0.287
MRK 938	HII	37.154	267.337	2.875
NGC 1056	HII	47.863	16.649	2.533
NGC 3511	HII	20.893	33.289	0.103
NGC 6810	HII	9.333	16.494	4.941
NGC 1097	LINER	3.467	1.369	3.247
NGC 2639	LINER	46.774	4.065	1.570
NGC 3079	LINER	151.356	5.787	154.192
NGC 4579	LINER	5.129	1.901	1.577
NGC 4594	LINER	16.218	39.842	1.474
NGC 5005	LINER	6.310	3.249	1.664
NGC 7496	LINER	23.988	0.946	3.561
NGC 7582	LINER	125.893	332.316	54.971

Table 6.5: Oxygen line ratios in HII (star-forming) and LINER galaxies by Baum et al. (2010) for comparison to Tables 6.3, 6.6 and 6.7. Classifications compiled from the literature by Gallimore et al. (2010) using naming convention by Véron-Cetty & Véron (2006).

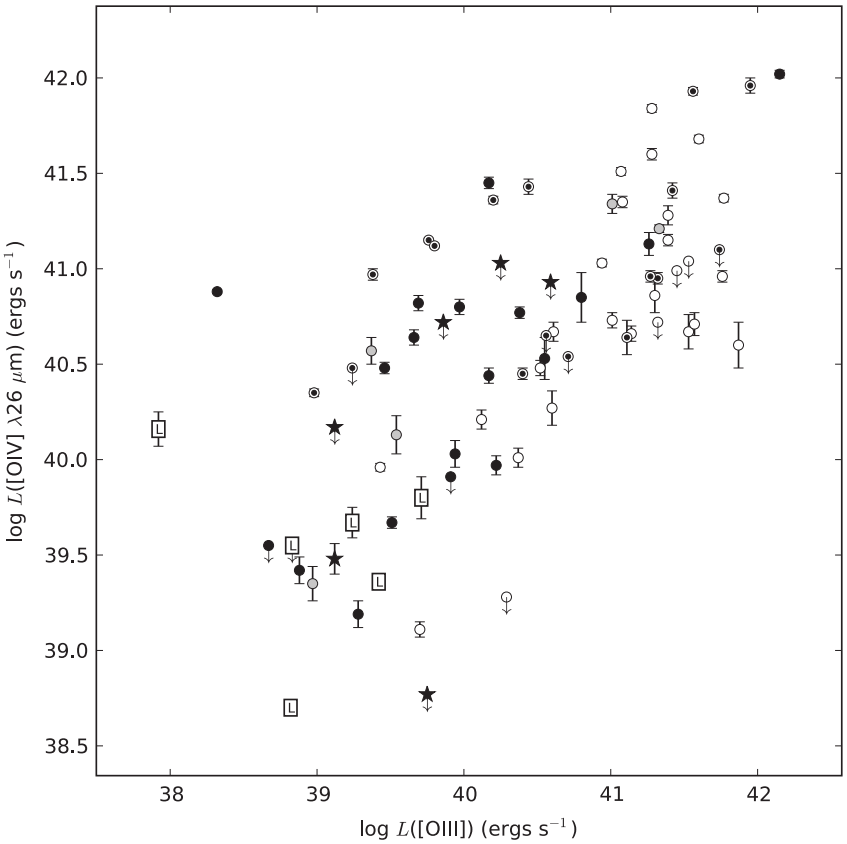

Figure 6.1 Figure by Baum et al. (2010) demonstrating the trend of higher [OIV]/[OIII] ratios in obscured objects. Data shown contains the same sources as in Tables 6.5-6.7 as well as some more for which the classification was uncertain. Filled circles represent Seyfert 2 sources, open circles represent Seyfert 1.0-1.5 and Seyfert 1n, filled stars represent HII-dominated sources, boxes with L represent LINERS, partially filled circles represent Seyfert 2 sources with a hidden broad line region (Seyfert 1i and 1h in Tables 6.5-6.7) and grey circles represent Seyfert 1.8 and 1.9 sources.

Source	Class	$L_{[\mathrm{OIV}]}$ 26 μm ($10^{39}\,\mathrm{erg\,s^{-1}}$)	$L_{[\mathrm{O\,III}]}$ ($10^{39}\,\mathrm{erg\,s^{-1}}$)	$\frac{L_{[\mathrm{O\,IV}]}}{L_{[\mathrm{O\,III}]}}$
E12-G21	S1n	380.189	170.486	2.230
F03450+0055	S1n	12.303	33.609	0.260
M-2-33-34-NGC4748	S1n	58.884	205.193	2.950
MRK 1239	S1n	14.454	10.697	0.465
MRK 335	S1n	81.283	174.806	0.145
MRK 766	S1n	194.984	219.157	0.611
NGC 4051	S1n	1.230	0.936	0.161
MRK 704	S1.2	208.930	560.049	0.890
MRK 79	S1.2	138.038	226.034	1.175
M-5-13-17	S1.5	131.826	509.104	0.350
M-6-30-15	S1.5	38.905	111.126	1.351
MRK 6	S1.5	81.283	205.193	0.373
MRK 817	S1.5	436.516	371.453	0.139
NGC 1566	S1.5	19.055	25.223	0.829
NGC 5548	S1.5	1.995	8.058	0.171
NGC 6860	S1.5	19.953	2.895	0.552
NGC 7213	S1.5	81.283	58.980	0.075
NGC 7603	S1.5	131.826	2.398	0.046

Table 6.6: Oxygen line ratios in Seyfert galaxies by Baum et al. (2010) for comparison to Table 6.3. S1n refer to narrow-line Seyfert 1 sources, S1.2 refers to sources intermediate between Seyfert 1 and 2 which are more similar to Seyfert 1, and S1.5 refers to refers to sources intermediate between Seyfert 1 and 2 with no clear bias either way. Continued in Table 6.7. Classifications compiled from the literature by Gallimore et al. (2010) using naming convention by Véron-Cetty & Véron (2006).

Source	Class	$L_{[\mathrm{OIV}]}$ 26 μm ($10^{39}\,\mathrm{erg\,s^{-1}}$)	$L_{[\mathrm{O\,III}]}$ ($10^{39}\,\mathrm{erg\,s^{-1}}$)	$\frac{L_{[\mathrm{O\,IV}]}}{L_{[\mathrm{O\,III}]}}$
F04385-0828	S1h	50.119	192.679	11.006
F15480-0344	S1h	16.982	1.543	2.537
IC 5063	S1h	676.083	174.806	0.781
M-2-8-39	S1h	213.796	94.664	10.259
M-3-58-7	S1h	257.040	25.055	0.259
MRK 348	S1h	46.774	321.581	0.396
NGC 424	S1h	44.668	571.954	0.360
NGC 4388	S1h	41.687	115.677	79.191
NGC 513	S1h	2.884	1.733	1.442
NGC 7314	S1h	97.724	0.210	25.348
NGC 7674	S1h	2.754	0.755	0.995
TOL 1238-364	S1h	851.138	855.541	0.249
NGC 1386	S1i	61.660	2.326	0.755
NGC 2992	S1i	7.586	4.831	26.156
NGC 1365	S1.8	56.234	23.808	26.504
NGC 6890	S1.9	6.457	1.307	1.620
NGC 1125	S2	2.188	0.674	14.118
NGC 1143-4	S2	61.660	4.367	0.767
NGC 1241	S2	53.703	37.121	2.788
NGC 1320	S2	25.119	9.008	2.362
NGC 1667	S2	4.169	5.028	11.507
NGC 4501	S2	501.187	6.329	2.698
NGC 4941	S2	0.977	0.663	1.942
NGC 5135	S2	3.802	2.692	6.461
NGC 5256	S2	257.040	178.293	0.760
NGC 5347	S2	1047.129	1377.450	0.248
NGC 5929	S2	208.930	15.907	0.566
NGC 5953	S2	60.256	351.802	6.892
NGC 7172	S2	14.125	8.720	464.514
NGC 7590	S2	1.660	0.466	3.649
UGC 11680	S2	208.930	61.147	1.046

Table 6.7: More oxygen line ratios in Seyfert galaxies by Baum et al. (2010) for comparison to Table 6.3. S1h refers to Seyfert 1 sources with hidden broad line region revealed by spectropolarimetry, S1i refers to Seyfert 1 sources with hidden broad line region revealed by non-polarimetric methods, S2 refer to Seyfert 2 sources, and S1.8-S1.9 refer to sources intermediate between Seyfert classes 1 & 2 which are more similar to Seyfert 2. Classifications compiled from the literature by Gallimore et al. (2010) using naming convention by Véron-Cetty & Véron (2006).

To put together all our lines of evidence we summarise in Table 6.8 all our results and those we found in the literature. We note that most sources which show at least one test with an inconclusive or positive result also show inconclusive or positive results on other tests. In particular, all sources which show evidence of a warm component are backed up by at least one line of evidence.

Source	Warm component (ours)	Warm component (others)	Broad polarised Hα	High [OIV]/[OIII]
NGC 315	Y	-	Y	N
3C 31	N	N	Y	Y
NGC 541	N	-	N	N
3C 66B	Y	I	Y	N
NGC 3801	I	-	N	N
NGC 3862	N	N	N	N
3C 270	Y	Y	Y	N
M 84	Y	Y	N	Y
M 87	N	N	N	N
NGC 7052	N	-	N	N

Table 6.8: Summary of evidence for a warm obscuring structure in each source.

6.2 Possibilites for future work

AGN are unresolved point sources but they are by definition embedded in galaxies which have a much greater angular size. While contributions from the host galaxy can likely never be eliminated completely, higher spatial resolution can reduce that contribution substantially as well as allow us to investigate the possibility of larger-scale dust obscuration such as that we hypothesise for NGC 315 in Section 6.1. The *James Webb* Space Telescope (*JWST*) will have two spectrographs that will be able to improve upon the spatial resolution of *Spitzer*. In the NIR *JWST* has its NIR spectrometer NIRSpec (Bagnasco et al., 2007) and in the the wavelength band $4.9 - 28.8\,\mu$m *JWST*'s Mid-infrared Instrument has the Medium Resolution Spectrometer (Rieke et al., 2015). These two instruments also have integral field unit capabilities which will allow for much better characterisation of the extended source background. Similarly, the Thirty Meter Telescope will have its Infrared Imaging Spectrograph and the *Euclid* Space Telescope will have its Near-Infrared Spectrometer and Photometer although the $2.0 - 2.5\,\mu$m long-wavelength cut-off (Larkin et al., 2010; Maciaszek et al., 2016) of these instruments severely limits their utility for our purposes. Additionally, any of the aforementioned instruments should allow us to extend our sample — possibly

allowing us to examine the full UGC FR-I sample by Verdoes Kleijn et al. (1999) of which our sample is a subset (see Chapter 3 for details).

As for the long-wavelength region not covered by *JWST*, although *Herschel* has run out of cryogen and so is no longer functioning other sub-mm observatories such as the Atacama Large Millimetre/sub-millimetre Array (ALMA) may be able to fill in the missing sub-mm data from NGC 315, 3C 66B, NGC 3801, NGC 3862, M 84, and NGC 7052.

Since the beginning of this project CASSIS has released its high-resolution catalogue however since we are primarily interested in wide continuum features we do not expect the increased spectral resolution to substantially improve our results. This could be tested and there is one object which we excluded because it only has a high-resolution spectrum which could be included, however that would require a complete overhaul of our software.

As for future directions for our data analysis we have five main leads. First off, due to time constraints we have not calculated the Eddington ratios for each of the torus fits. Second, the separation Baum et al. (2010) found between obscured and unobscured sources in [OIV]/[OIII] ratios is clearer when plotted against silicate strengths such as those we calculated in Section 4.2.3. We show their plot demonstrating this in Figure 6.2. Third, we can look more closely at the *HST* images by Verdoes Kleijn et al. (1999) to attempt to more precisely consider the effects of the large-scale cold dust features in said images. This also ties in with our earlier mention of getting integral field spectroscopy from *JWST*. Fourth, a possible check on our results is to see if the AGN luminosities in NGC 315 and the forced-torus fits are sufficient to ionise enough oxygen to explain the [OIII] line luminosities. Finally, and most ambitiously, we are considering the possibility of trying alternate stellar population models, particularly for NGC 3801, which can accommodate multiple starbursts.

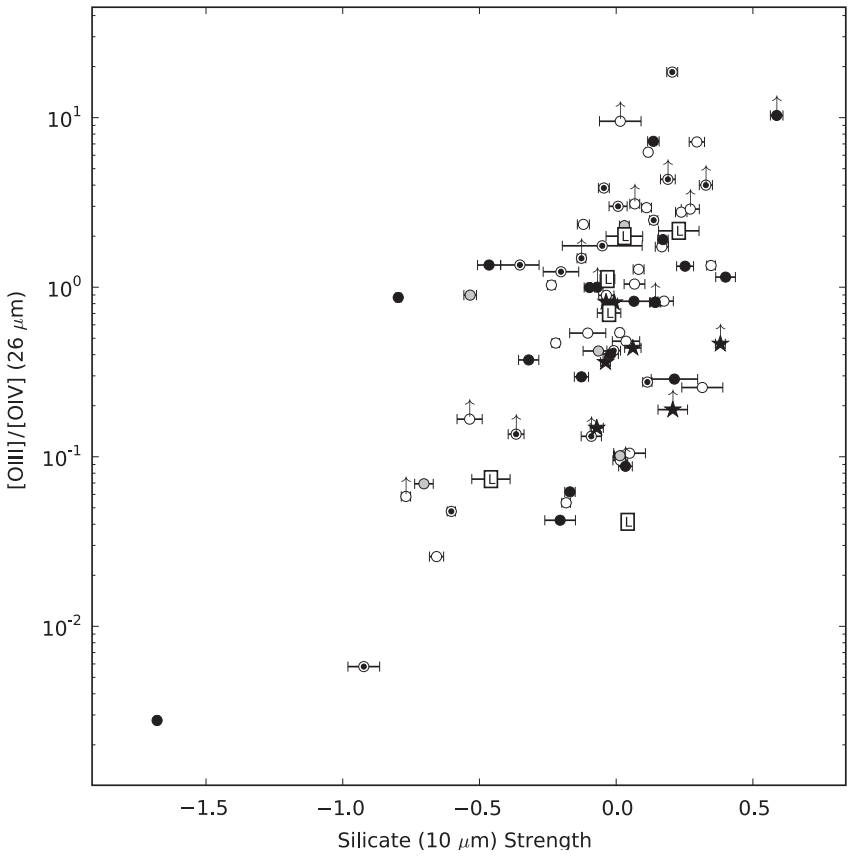

Figure 6.2 Figure by Baum et al. (2010) demonstrating the trend of higher [OIII]/[OIV] ratios in Seyferts with a brighter 10 μm silicate feature. Data shown contains the same sources as Figure 6.1 with the same symbols. Recall that filled circles represent Seyfert 2 sources, open circles represent Seyfert 1.0-1.5 and Seyfert 1n, filled stars represent HII-dominated sources, boxes with L represent LINERS, partially filled circles represent Seyfert 2 sources with a hidden broad line region, (Seyfert 1i and 1h in Tables 6.5-6.7) and grey circles represent Seyfert 1.8 and 1.9 sources.

Chapter 7

Conclusion

How do FR-I radio galaxies fit into the broader picture of AGN? Are they intrinsically dim or is the optical emission from a bright accretion disk blocked along our line of sight? If these sources contain obscured accretion disks then the leading model suggests that the obscuration takes the form of a warm dusty torus which would appear as a thermal emission feature with a peak at around $10 - 20\,\mu$m. If such a torus and obscured accretion disk are present then FR-I radio galaxies would likely be the off-axis counterparts of BL Lacertae objects (a type of blazar).

We used fitting codes based on MCMC algorithms to examine the IR spectra, primarily from *Spitzer*/IRS, of ten nearby FR-I radio galaxies (NGC 315, 3C 31, NGC 541, 3C 66B, NGC 3801, NGC 3862, 3C 270, M 84, M 87, and NGC 7052) in order to determine whether there is significant contribution in the MIR from warm dust. This dust would serve to obscure the central engine and thus explain why AGN with high radio luminosities can resemble quiescent galaxies in optical wavelengths. The leading alternative model for a FR-I is powered by a ADAF which puts the vast majority of its output power into a radio jet.

We find that the IR spectra of six of our ten sources are clearly dominated by emission from either their host or jet. Our results clearly support the existence of a warm dusty structure in NGC 315, 3C 66B, 3C 270, and M 84. Of those, only NGC 315 is clearly

consistent with the model of a clumpy obscuring torus. One more source, NGC 3801, benefits from the inclusion of a warm component however the best fit to that component is unusually dim.

Overall, our results are consistent with the two-mode model described in Section 1.3.2 with 30-40% of sources having warm components indicative of high-excitation sources. Our results, however, point to a different dust geometry in some of these sources. Curiously, when we calculated the excitation index (Buttiglione et al., 2010) for each source using photometry from the literature we found that none of our sources are consistent with being HERGs and two, NGC 315 and NGC 541, are extremely low excitation sources. Curiously, one of these extremely low excitation sources is one with an infrared spectral energy distribution consistent with a high excitation source. Perhaps this apparent incongruity may be related to the unknown dust geometry we previously mentioned. The remaining AGN in this sample show too little nuclear emission to draw any conclusions about the accretion mode aside from that which can be inferred from the low IR luminosity itself; our observations are inconsistent with high accretion rates in modes with high radiative efficiency. Given how this class of sources seems to contain both thermal and non-thermal sources and straddles the theoretical minimum proposed by Elitzur & Shlosman (2006) it is possible that there are transitional or hybrid sources between thermal and non-thermal AGN in the broader FR-I umbrella.

Bibliography

Allen, S. W., Dunn, R. J. H., Fabian, A. C., Taylor, G. B., & Reynolds, C. S. 2006, MNRAS, 372, 21

Anderson, J. M., & Ulvestad, J. S. 2005, ApJ, 627, 674

Antonucci, R. 1993, ARA&A, 31, 473

—. 2012, Astronomical and Astrophysical Transactions, 27, 557

Astropy Collaboration, Robitaille, T. P., Tollerud, E. J., et al. 2013, A&A, 558, A33

Baes, M., Clemens, M., Xilouris, E. M., et al. 2010, A&A, 518, L53

Bagnasco, G., Kolm, M., Ferruit, P., et al. 2007, in Proc. SPIE, Vol. 6692, Cryogenic Optical Systems and Instruments XII, 66920M

Baldi, R. D., & Capetti, A. 2009, A&A, 508, 603

Balmaverde, B., Capetti, A., Moisio, D., Baldi, R. D., & Marconi, A. 2016, A&A, 586, A48

Barth, A. J., Filippenko, A. V., & Moran, E. C. 1999, ApJ, 525, 673

Baum, S. A., Zirbel, E. L., & O'Dea, C. P. 1995, ApJ, 451, 88

Baum, S. A., Gallimore, J. F., O'Dea, C. P., et al. 2010, ApJ, 710, 289

Best, P. N., & Heckman, T. M. 2012, MNRAS, 421, 1569

Blanton, M. R., Bershady, M. A., Abolfathi, B., et al. 2017, AJ, 154, 28

Bondi, H. 1952, MNRAS, 112, 195

Bridle, A. H. 1984, AJ, 89, 979

Brooks, S., Gelman, A., Jones, G. L., & Meng, X. 2011, Handbook of Markov chain Monte Carlo (Boca Raton: CRC Press/Taylor & Francis)

Butcher, H. R., van Breugel, W., & Miley, G. K. 1980, ApJ, 235, 749

Buttiglione, S., Capetti, A., Celotti, A., et al. 2009, A&A, 495, 1033

—. 2010, A&A, 509, A6

Capetti, A., Verdoes Kleijn, G., & Chiaberge, M. 2005, A&A, 439, 935

Capetti, A., Buttiglione, S., Axon, D. J., et al. 2011, A&A, 527, L2

Carroll, B. W., & Ostlie, D. A. 1996, An Introduction to Modern Astrophysics

Chiaberge, M., Capetti, A., & Celotti, A. 1999, A&A, 349, 77

Cid Fernandes, R., González Delgado, R. M., Schmitt, H., et al. 2004, ApJ, 605, 105

Cohen, M., Wheaton, W. A., & Megeath, S. T. 2003, AJ, 126, 1090

Condon, J. J., & Broderick, J. J. 1985, AJ, 90, 2540

—. 1986, AJ, 91, 1051

—. 1988, AJ, 96, 30

Constantin, A., Shields, J. C., Ho, L. C., et al. 2015, ApJ, 814, 149

Crane, P., Peletier, R., Baxter, D., et al. 1993, ApJ, 402, L37

Croston, J. H., Birkinshaw, M., Conway, E., & Davies, R. L. 2003, MNRAS, 339, 82

Cutri, R. M., Skrutskie, M. F., van Dyk, S., et al. 2003, 2MASS All Sky Catalog of point sources.

Das, M., Vogel, S. N., Verdoes Kleijn, G. A., O'Dea, C. P., & Baum, S. A. 2005, ApJ, 629, 757

Draine, B. T., & Li, A. 2007, ApJ, 657, 810

Elitzur, M., & Shlosman, I. 2006, ApJ, 648, L101

Fanaroff, B. L., & Riley, J. M. 1974, MNRAS, 167, 31P

Farrah, D., Bernard-Salas, J., Spoon, H. W. W., et al. 2007, ApJ, 667, 149

Fazio, G. G., Hora, J. L., Allen, L. E., et al. 2004, ApJS, 154, 10

Fischera, J., Dopita, M. A., & Sutherland, R. S. 2003, ApJ, 599, L21

Frogel, J. A., Persson, S. E., Matthews, K., & Aaronson, M. 1978, ApJ, 220, 75

Gallimore, J. F., Yzaguirre, A., Jakoboski, J., et al. 2010, ApJS, 187, 172

Gendre, M. A., Best, P. N., Wall, J. V., & Ker, L. M. 2013, MNRAS, 430, 3086

González-Martín, O., Masegosa, J., Márquez, I., et al. 2015, A&A, 578, A74

Granato, G. L., & Danese, L. 1994, MNRAS, 268, 235

Granato, G. L., Danese, L., & Franceschini, A. 1997, ApJ, 486, 147

Griffin, M., Abergel, A., Ade, P., et al. 2007, Advances in Space Research, 40, 612

Gu, Q.-S., Huang, J.-S., Wilson, G., & Fazio, G. G. 2007, ApJ, 671, L105

Haas, M., Siebenmorgen, R., Schulz, B., Krügel, E., & Chini, R. 2005, A&A, 442, L39

Hardcastle, M. J., Evans, D. A., & Croston, J. H. 2007, MNRAS, 376, 1849

Higdon, S. J. U., Devost, D., Higdon, J. L., et al. 2004, PASP, 116, 975

Ho, L. C., & Keto, E. 2007, ApJ, 658, 314

Hota, A., Rey, S.-C., Kang, Y., et al. 2012, MNRAS, 422, L38

Houck, J. R., Roellig, T. L., van Cleve, J., et al. 2004, ApJS, 154, 18

Hu, J.-F., Cao, X.-W., Chen, L., & You, B. 2016, Research in Astronomy and Astrophysics, 16, 136

Ichimaru, S. 1977, ApJ, 214, 840

Ineson, J., Croston, J. H., Hardcastle, M. J., et al. 2015, MNRAS, 453, 2682

Jaffe, W., Ford, H. C., Ferrarese, L., van den Bosch, F., & O'Connell, R. W. 1993, Nature, 364, 213

Jensen, J. J., Hönig, S. F., Rakshit, S., et al. 2017, ArXiv e-prints, arXiv:1706.04811

Katz, J. I. 1977, ApJ, 215, 265

Kharb, P., O'Dea, C. P., Tilak, A., et al. 2012, ApJ, 754, 1

Kharb, P., & Shastri, P. 2004, A&A, 425, 825

Kleijn, G. A. V., Baum, S. A., de Zeeuw, P. T., & ODea, C. P. 2002, The Astronomical Journal, 123, 1334

Laing, R. A., Bridle, A. H., Parma, P., & Murgia, M. 2008, MNRAS, 391, 521

Lanz, L., Bliss, A., Kraft, R. P., et al. 2011, ApJ, 731, 52

Larkin, J. E., Moore, A. F., Barton, E. J., Wright, S. A., & IRIS Team. 2010, in Bulletin of the American Astronomical Society, Vol. 42, American Astronomical Society Meeting Abstracts #215, 405

Lebouteiller, V., Barry, D. J., Spoon, H. W. W., et al. 2011, ApJS, 196, 8

Ledlow, M. J., & Owen, F. N. 1996, AJ, 112, 9

Leipski, C., Antonucci, R., Ogle, P., & Whysong, D. 2009, ApJ, 701, 891

Lilly, S. J., Longair, M. S., & Miller, L. 1985, MNRAS, 214, 109

Lynden-Bell, D., & Pringle, J. E. 1974, MNRAS, 168, 603

Maciaszek, T., Ealet, A., Jahnke, K., et al. 2016, in Proc. SPIE, Vol. 9904, Space Telescopes and Instrumentation 2016: Optical, Infrared, and Millimeter Wave, 99040T

Makovoz, D., & Marleau, F. R. 2005, PASP, 117, 1113

Marton, G., Schulz, B., Altieri, B., et al. 2016, in IAU Symposium, Vol. 315, From Interstellar Clouds to Star-Forming Galaxies: Universal Processes?, ed. P. Jablonka, P. André, & F. van der Tak, E53

Merritt, D., & Ferrarese, L. 2001, ApJ, 547, 140

Mor, R., Netzer, H., & Elitzur, M. 2009, ApJ, 705, 298

Narayan, R., Mahadevan, R., & Quataert, E. 1998, in Theory of Black Hole Accretion Disks, ed. M. A. Abramowicz, G. Björnsson, & J. E. Pringle, 148–182

Nemmen, R. S., Storchi-Bergmann, T., & Eracleous, M. 2014, MNRAS, 438, 2804

Nenkova, M., Ivezic, Z., & Elitzur, M. 1999, in LPI Contributions, Vol. 969, Thermal Emission Spectroscopy and Analysis of Dust, Disks, and Regoliths, ed. A. Sprague, D. K. Lynch, & M. Sitko, 20

Nenkova, M., Ivezić, Ž., & Elitzur, M. 2002, ApJ, 570, L9

Nenkova, M., Sirocky, M. M., Ivezić, Ž., & Elitzur, M. 2008a, ApJ, 685, 147

Nenkova, M., Sirocky, M. M., Nikutta, R., Ivezić, Ž., & Elitzur, M. 2008b, ApJ, 685, 160

Netzer, H. 2015, ARA&A, 53, 365

Nilson, P. 1973, Uppsala general catalogue of galaxies

Noel-Storr, J., Baum, S. A., & O'Dea, C. P. 2007, ApJ, 663, 71

Noel-Storr, J., Baum, S. A., Verdoes Kleijn, G., et al. 2003, ApJS, 148, 419

Padovani, P. 2016, A&A Rev., 24, 13

Padovani, P., Alexander, D. M., Assef, R. J., et al. 2017, A&A Rev., 25, 2

Perley, R. A., Dreher, J. W., & Cowan, J. J. 1984, ApJ, 285, L35

Perlman, E. S., Biretta, J. A., Sparks, W. B., Macchetto, F. D., & Leahy, J. P. 2001, ApJ, 551, 206

Perlman, E. S., Mason, R. E., Packham, C., et al. 2007, ApJ, 663, 808

Peterson, B. M. 1997, An Introduction to Active Galactic Nuclei

Pier, E. A., & Krolik, J. H. 1992, ApJ, 401, 99

—. 1993, ApJ, 418, 673

Quataert, E., Di Matteo, T., Narayan, R., & Ho, L. C. 1999, ApJ, 525, L89

Rees, M. J., Begelman, M. C., Blandford, R. D., & Phinney, E. S. 1982, Nature, 295, 17

Richings, A. J., Uttley, P., & Körding, E. 2011, MNRAS, 415, 2158

Rieke, G. H., Young, E. T., Engelbracht, C. W., et al. 2004, ApJS, 154, 25

Rieke, G. H., Ressler, M. E., Morrison, J. E., et al. 2015, PASP, 127, 665

Rowan-Robinson, M. 1995, MNRAS, 272, 737

Sales, D. A., Robinson, A., Axon, D. J., et al. 2015, ApJ, 799, 25

Schartmann, M., Meisenheimer, K., Camenzind, M., Wolf, S., & Henning, T. 2005, A&A, 437, 861

Schwarz, G. 1978, Ann. Statist., 6, 461

Shakura, N. I., & Sunyaev, R. A. 1973, A&A, 24, 337

Shapiro, S. L., Lightman, A. P., & Eardley, D. M. 1976, ApJ, 204, 187

Shi, Y., Rieke, G. H., Hines, D. C., Gordon, K. D., & Egami, E. 2007, ApJ, 655, 781

Sikora, M., Stasińska, G., Kozieł-Wierzbowska, D., Madejski, G. M., & Asari, N. V. 2013, ApJ, 765, 62

Silva, L., Granato, G. L., Bressan, A., & Danese, L. 1998, ApJ, 509, 103

Sirocky, M. M., Levenson, N. A., Elitzur, M., Spoon, H. W. W., & Armus, L. 2008, ApJ, 678, 729

Skrutskie, M. F., Cutri, R. M., Stiening, R., et al. 2006, AJ, 131, 1163

Smith, J. D. T., Draine, B. T., Dale, D. A., et al. 2007, ApJ, 656, 770

Sparke, L. S., & Gallagher, III, J. S. 2007, Galaxies in the Universe: An Introduction (Cambridge University Press)

Spinoglio, L., & Malkan, M. A. 1992, ApJ, 399, 504

Tansley, D., Birkinshaw, M., Hardcastle, M. J., & Worrall, D. M. 2000, MNRAS, 317, 623

Temi, P., Brighenti, F., & Mathews, W. G. 2009, ApJ, 707, 890

Teplitz, H. I., Capak, P., Hanish, D., et al. 2012, in American Astronomical Society Meeting Abstracts, Vol. 219, American Astronomical Society Meeting Abstracts #219, 428.06

Urry, C. M., & Padovani, P. 1995, PASP, 107, 803

van der Wolk, G., Barthel, P. D., Peletier, R. F., & Pel, J. W. 2010a, A&A, 511, A64

—. 2010b, A&A, 511, A64

Verdoes Kleijn, G. A., Baum, S. A., de Zeeuw, P. T., & O'Dea, C. P. 1999, AJ, 118, 2592

Verdoes Kleijn, G. A., & de Zeeuw, P. T. 2005, A&A, 435, 43

Véron-Cetty, M.-P., & Véron, P. 2006, A&A, 455, 773

Werner, M. W., Roellig, T. L., Low, F. J., et al. 2004, ApJS, 154, 1

Whysong, D., & Antonucci, R. 2004, ApJ, 602, 116

Willett, K. W., Stocke, J. T., Darling, J., & Perlman, E. S. 2010, ApJ, 713, 1393

Xu, C., Baum, S. A., O'Dea, C. P., Wrobel, J. M., & Condon, J. J. 2000, AJ, 120, 2950

Xu, C., Livio, M., & Baum, S. 1999, AJ, 118, 1169

Xu, Y.-D., & Cao, X.-W. 2009, Research in Astronomy and Astrophysics, 9, 401

Zirbel, E. L., & Baum, S. A. 2003, AJ, 125, 1795

Appendix A

Glossary

A.1 Initialisms

2MASS
Two Micron All-Sky Survey

3C(R)
Third Cambridge Catalogue of Radio Sources (Revised)

ADAF
Advection-dominated accretion flow

AGN
Active galactic nucleus (singular) or active galactic nuclei (plural)

ALMA
Atacama Large Millimeter/submillimeter Array

AOR
Astronomical observation request

APEX
Aperture extraction package for MOPEX

BIC
Bayesian Information Criterion

CASSIS
Combined Atlas of Sources with *Spitzer*/IRS Spectra

ELERG
Extremely low-excitation radio galaxy

EI
Excitation index

FR-I/FR-II
Fanaroff & Riley class I/II

FWHM
Full width at half maximum

HERG
High-excitation radio galaxy

HST
Hubble Space Telescope

IDL
Interactive Data Language

IRAC
Infrared Array Camera

IRS
Infrared Spectrometer

ISM
Interstellar medium

JWST
James Webb Space Telescope

LERG
Low-excitation radio galaxy

LINER
Low-ionisation nuclear emission line region

M
Messier (catalogue)

MCMC
Markov chain Monte Carlo

MIPS
Multiband Imaging Photometer for *Spitzer*

MIR
Mid-infrared

MOPEX
Mosaicking and Point-source Extraction

NGC
New General Catalogue

NIR
Near infrared

NLR
Narrow line region

PAH
: Polycyclic aromatic hydrocarbon

PSF
: Point spread function

RA
: Right ascension

SDSS
: Sloan Digital Sky Survey

SFR
: Star formation rate

SMBH
: Supermassive Black Hole

SPIRE
: Spectral and Photometric Imaging Receiver

UGC
: Uppsala General Catalogue

VLT
: Very Large Telescope

Appendix B

Full line fit results

Line	Central Wavelength (μm)	Luminosity ($10^{39}\,\mathrm{erg\,s^{-1}}$)
H2 S(7)	5.52	< 7.16
H2 S(6)	6.11	< 7.35
H2 S(5)	6.91	< 3.9
H2 S(4)	8.03	< 7.38
H2 S(3)	9.66	< 3.76
H2 S(2)	12.28	< 2.98
H2 S(1)	17.03	$3.79^{1.28}_{1.19}$
H2 S(0)	28.22	< 2.74
[ArII]	6.99	$11.31^{1.88}_{1.29}$
[ArIII]	8.99	< 1.54
[NeII]	12.81	$19.98^{0.72}_{1.1}$
[NeIII] 15	15.55	$14.26^{0.86}_{0.86}$
[NeIII] 36	35.01	< 13.61
[NeV] 14	14.32	< 4.76
[NeV] 24	24.32	< 2.98
[NeVI]	7.65	< 5.87
[OIV]	25.91	< 4.98
[SIII] 18	18.71	$4.45^{1.2}_{0.88}$
[SIII] 33	33.48	< 10.62
[SIV]	10.51	$3.41^{0.81}_{0.62}$
[SiII]	34.82	< 13.73
[FeI]	34.71	< 12.54
[FeII] 25	25.99	< 4.97
[FeII] 35a	35.35	< 5.13
[FeII] 35b	35.78	< 10.56

Table B.1: Ionization narrow-line luminosities in NGC 315.

Line	Central Wavelength (μm)	Luminosity ($10^{39}\,\mathrm{erg\,s^{-1}}$)
PAH	5.27	< 6.2
PAH	5.7	< 40.56
PAH	6.22	$71.01^{4.86}_{3.63}$
PAH	6.69	$94.5^{11.77}_{11.94}$
PAH	7.42	$240.92^{29.52}_{20.96}$
PAH	7.6	< 54.52
PAH	7.85	$66.61^{7.47}_{6.23}$
PAH	8.33	$25.24^{5.87}_{6.61}$
PAH	8.61	< 17.51
PAH	10.68	$11.59^{1.92}_{1.4}$
PAH	11.23	$8.87^{2.41}_{2.81}$
PAH	11.33	$69.24^{7.16}_{3.98}$
PAH	11.99	$35.03^{6.49}_{2.92}$
PAH	12.62	$34.56^{6.65}_{4.52}$
PAH	12.69	$10.73^{2.66}_{2.52}$
PAH	13.48	< 6.71
PAH	14.04	< 5.75
PAH	14.19	< 7.84
PAH	14.19	< 7.98
PAH	15.9	< 14.99
PAH	16.45	$8.34^{1.87}_{2.05}$
PAH	17.04	$30.79^{6.65}_{7.08}$
PAH	17.38	< 6.12
PAH	17.87	< 8.71
PAH	18.92	< 6.89
PAH	33.1	$25.43^{6.0}_{5.33}$

Table B.2: PAH narrow-line luminosities in NGC 315.

Line	Central Wavelength (μm)	Luminosity ($10^{39}\,\mathrm{erg\,s^{-1}}$)
H2 S(7)	5.52	< 1.33
H2 S(6)	6.11	< 0.44
H2 S(5)	6.91	$6.36^{0.81}_{0.86}$
H2 S(4)	8.03	$1.34^{0.32}_{0.4}$
H2 S(3)	9.66	$4.07^{0.22}_{0.22}$
H2 S(2)	12.28	$2.69^{0.2}_{0.27}$
H2 S(1)	17.03	$4.72^{0.68}_{0.76}$
H2 S(0)	28.22	< 2.66
[ArII]	6.99	$8.48^{0.49}_{0.5}$
[ArIII]	8.99	< 0.34
[NeII]	12.81	$13.74^{0.24}_{0.27}$
[NeIII] 15	15.55	$8.3^{0.37}_{0.41}$
[NeIII] 36	35.01	< 5.94
[NeV] 14	14.32	< 3.32
[NeV] 24	24.32	< 0.82
[NeVI]	7.65	< 5.24
[OIV]	25.91	$3.46^{0.72}_{0.77}$
[SIII] 18	18.71	$3.34^{0.68}_{0.57}$
[SIII] 33	33.48	< 6.39
[SIV]	10.51	$2.79^{0.3}_{0.42}$
[SiII]	34.82	$9.69^{1.12}_{1.34}$
[FeI]	34.71	< 3.01
[FeII] 25	25.99	< 3.03
[FeII] 35a	35.35	< 4.07
[FeII] 35b	35.78	< 4.02

Table B.3: Ionization narrow-line luminosities in 3C 31.

Line	Central Wavelength (μm)	Luminosity ($10^{39}\,\mathrm{erg\,s^{-1}}$)
PAH	5.27	$29.83^{3.06}_{2.89}$
PAH	5.7	$7.79^{1.85}_{1.66}$
PAH	6.22	$134.83^{1.43}_{1.24}$
PAH	6.69	$9.26^{2.49}_{3.04}$
PAH	7.42	$213.45^{12.21}_{15.65}$
PAH	7.6	$109.43^{5.82}_{5.34}$
PAH	7.85	$212.6^{2.59}_{3.81}$
PAH	8.33	$55.31^{3.3}_{3.0}$
PAH	8.61	$80.7^{1.83}_{2.52}$
PAH	10.68	$6.98^{0.56}_{0.59}$
PAH	11.23	$41.18^{1.03}_{1.08}$
PAH	11.33	$190.84^{1.41}_{1.95}$
PAH	11.99	$70.15^{1.05}_{1.1}$
PAH	12.62	$119.26^{1.88}_{1.92}$
PAH	12.69	$4.23^{0.83}_{0.76}$
PAH	13.48	$21.96^{1.54}_{1.52}$
PAH	14.04	$6.81^{1.9}_{2.01}$
PAH	14.19	< 12.92
PAH	14.19	< 13.37
PAH	15.9	$4.29^{1.09}_{1.2}$
PAH	16.45	$16.49^{0.89}_{0.9}$
PAH	17.04	$128.12^{5.28}_{4.76}$
PAH	17.38	$6.26^{1.1}_{0.95}$
PAH	17.87	$7.87^{1.31}_{1.25}$
PAH	18.92	$10.19^{1.9}_{1.84}$
PAH	33.1	$22.04^{3.78}_{3.67}$

Table B.4: PAH narrow-line luminosities in 3C 31.

Line	Central Wavelength (μm)	Luminosity ($10^{39}\,\mathrm{erg\,s^{-1}}$)
H2 S(7)	5.52	< 7.12
H2 S(6)	6.11	< 6.67
H2 S(5)	6.91	< 8.49
H2 S(4)	8.03	< 3.84
H2 S(3)	9.66	$3.32^{0.92}_{0.93}$
H2 S(2)	12.28	< 4.42
H2 S(1)	17.03	< 8.18
H2 S(0)	28.22	< 9.83
[ArII]	6.99	< 7.31
[ArIII]	8.99	< 5.59
[NeII]	12.81	$3.24^{0.95}_{1.0}$
[NeIII] 15	15.55	< 5.7
[NeIII] 36	35.01	< 13.9
[NeV] 14	14.32	< 7.87
[NeV] 24	24.32	< 4.67
[NeVI]	7.65	< 5.75
[OIV]	25.91	< 6.28
[SIII] 18	18.71	< 5.59
[SIII] 33	33.48	< 17.91
[SIV]	10.51	< 3.91
[SiII]	34.82	< 10.25
[FeI]	34.71	< 7.63
[FeII] 25	25.99	< 5.18
[FeII] 35a	35.35	< 13.83
[FeII] 35b	35.78	< 11.57

Table B.5: Ionization narrow-line luminosities in NGC 541.

Line	Central Wavelength (μm)	Luminosity ($10^{39}\,\mathrm{erg\,s^{-1}}$)
PAH	5.27	< 24.02
PAH	5.7	< 40.8
PAH	6.22	$34.87^{5.37}_{5.1}$
PAH	6.69	< 76.01
PAH	7.42	< 107.3
PAH	7.6	$62.02^{8.26}_{8.44}$
PAH	7.85	$28.08^{7.06}_{6.59}$
PAH	8.33	< 28.52
PAH	8.61	$29.95^{4.6}_{4.93}$
PAH	10.68	$8.75^{2.18}_{2.22}$
PAH	11.23	$10.84^{2.52}_{2.58}$
PAH	11.33	$39.38^{5.25}_{5.66}$
PAH	11.99	$17.53^{4.63}_{4.72}$
PAH	12.62	$23.72^{5.92}_{6.68}$
PAH	12.69	< 14.44
PAH	13.48	< 21.96
PAH	14.04	< 15.46
PAH	14.19	< 21.12
PAH	14.19	< 14.2
PAH	15.9	< 35.83
PAH	16.45	< 13.73
PAH	17.04	< 45.14
PAH	17.38	< 13.29
PAH	17.87	< 20.89
PAH	18.92	< 31.34
PAH	33.1	< 49.45

Table B.6: PAH narrow-line luminosities in NGC 541.

Line	Central Wavelength (μm)	Luminosity ($10^{39}\,\mathrm{erg\,s^{-1}}$)
H2 S(7)	5.52	< 2.56
H2 S(6)	6.11	< 2.02
H2 S(5)	6.91	< 2.79
H2 S(4)	8.03	$1.79^{0.31}_{0.34}$
H2 S(3)	9.66	$1.8^{0.3}_{0.3}$
H2 S(2)	12.28	< 1.53
H2 S(1)	17.03	< 4.61
H2 S(0)	28.22	< 3.08
[ArII]	6.99	$5.3^{0.46}_{0.46}$
[ArIII]	8.99	$1.95^{0.29}_{0.32}$
[NeII]	12.81	$7.17^{0.31}_{0.31}$
[NeIII] 15	15.55	$7.19^{0.58}_{0.56}$
[NeIII] 36	35.01	< 5.38
[NeV] 14	14.32	< 3.59
[NeV] 24	24.32	< 1.95
[NeVI]	7.65	< 2.26
[OIV]	25.91	< 3.1
[SIII] 18	18.71	$3.41^{0.87}_{0.89}$
[SIII] 33	33.48	< 5.49
[SIV]	10.51	< 2.81
[SiII]	34.82	< 8.02
[FeI]	34.71	< 7.45
[FeII] 25	25.99	< 3.03
[FeII] 35a	35.35	< 6.18
[FeII] 35b	35.78	< 4.07

Table B.7: Ionization narrow-line luminosities in 3C 66B.

Line	Central Wavelength (μm)	Luminosity ($10^{39}\,\mathrm{erg\,s^{-1}}$)
PAH	5.27	< 13.88
PAH	5.7	< 6.18
PAH	6.22	$18.21^{1.52}_{1.55}$
PAH	6.69	$39.17^{3.11}_{3.34}$
PAH	7.42	< 40.51
PAH	7.6	< 10.49
PAH	7.85	< 2.97
PAH	8.33	< 2.95
PAH	8.61	< 4.79
PAH	10.68	$2.72^{0.76}_{0.71}$
PAH	11.23	< 2.32
PAH	11.33	$10.6^{1.08}_{1.09}$
PAH	11.99	< 5.21
PAH	12.62	< 8.82
PAH	12.69	< 4.38
PAH	13.48	< 4.62
PAH	14.04	$7.16^{1.52}_{1.79}$
PAH	14.19	< 10.09
PAH	14.19	< 6.93
PAH	15.9	$5.38^{1.56}_{1.55}$
PAH	16.45	< 11.51
PAH	17.04	< 23.01
PAH	17.38	< 5.8
PAH	17.87	< 4.08
PAH	18.92	< 11.03
PAH	33.1	< 14.22

Table B.8: PAH narrow-line luminosities in 3C 66B.

Line	Central Wavelength (μm)	Luminosity ($10^{39}\,\mathrm{erg\,s^{-1}}$)
H2 S(7)	5.52	< 3.7
H2 S(6)	6.11	< 4.82
H2 S(5)	6.91	< 5.94
H2 S(4)	8.03	< 4.58
H2 S(3)	9.66	$2.48^{0.82}_{0.78}$
H2 S(2)	12.28	$2.36^{0.53}_{0.49}$
H2 S(1)	17.03	$7.69^{0.71}_{0.71}$
H2 S(0)	28.22	< 3.02
[ArII]	6.99	< 4.19
[ArIII]	8.99	< 2.27
[NeII]	12.81	$6.24^{0.57}_{0.55}$
[NeIII] 15	15.55	$1.69^{0.44}_{0.44}$
[NeIII] 36	35.01	< 8.69
[NeV] 14	14.32	< 2.45
[NeV] 24	24.32	< 3.78
[NeVI]	7.65	< 11.26
[OIV]	25.91	< 3.2
[SIII] 18	18.71	< 4.1
[SIII] 33	33.48	< 8.34
[SIV]	10.51	$1.95^{0.55}_{0.56}$
[SiII]	34.82	< 11.47
[FeI]	34.71	< 7.21
[FeII] 25	25.99	< 2.65
[FeII] 35a	35.35	< 7.7
[FeII] 35b	35.78	< 6.85

Table B.9: Ionization narrow-line luminosities in NGC 3801.

Line	Central Wavelength (μm)	Luminosity ($10^{39}\,\mathrm{erg\,s^{-1}}$)
PAH	5.27	< 28.75
PAH	5.7	< 20.74
PAH	6.22	$77.41^{3.33}_{3.33}$
PAH	6.69	< 32.08
PAH	7.42	$83.56^{18.88}_{23.16}$
PAH	7.6	$86.4^{9.32}_{9.35}$
PAH	7.85	$116.65^{5.8}_{6.43}$
PAH	8.33	$28.83^{4.87}_{4.5}$
PAH	8.61	$56.81^{3.78}_{3.72}$
PAH	10.68	$6.9^{1.34}_{1.36}$
PAH	11.23	$36.73^{1.59}_{1.8}$
PAH	11.33	$94.41^{3.07}_{3.09}$
PAH	11.99	$41.7^{3.1}_{2.51}$
PAH	12.62	$62.0^{4.16}_{3.97}$
PAH	12.69	$7.63^{2.58}_{2.4}$
PAH	13.48	$22.11^{2.79}_{2.64}$
PAH	14.04	< 6.15
PAH	14.19	< 6.57
PAH	14.19	< 5.51
PAH	15.9	$4.41^{1.53}_{1.39}$
PAH	16.45	$9.7^{1.16}_{1.1}$
PAH	17.04	$72.63^{4.72}_{5.86}$
PAH	17.38	< 6.28
PAH	17.87	< 6.44
PAH	18.92	$8.12^{2.3}_{2.23}$
PAH	33.1	< 20.7

Table B.10: PAH narrow-line luminosities in NGC 3801.

Line	Central Wavelength (μm)	Luminosity ($10^{39}\,\mathrm{erg\,s^{-1}}$)
H2 S(7)	5.52	< 3.91
H2 S(6)	6.11	< 4.07
H2 S(5)	6.91	< 4.87
H2 S(4)	8.03	$2.43^{0.47}_{0.45}$
H2 S(3)	9.66	< 1.61
H2 S(2)	12.28	$1.15^{0.32}_{0.38}$
H2 S(1)	17.03	< 7.06
H2 S(0)	28.22	< 4.6
[ArII]	6.99	$3.66^{0.81}_{0.86}$
[ArIII]	8.99	< 1.39
[NeII]	12.81	$10.72^{0.36}_{0.38}$
[NeIII] 15	15.55	$5.81^{1.06}_{1.01}$
[NeIII] 36	35.01	< 8.01
[NeV] 14	14.32	< 2.4
[NeV] 24	24.32	< 2.86
[NeVI]	7.65	< 5.43
[OIV]	25.91	< 4.12
[SIII] 18	18.71	< 5.1
[SIII] 33	33.48	$5.52^{1.86}_{1.79}$
[SIV]	10.51	$1.15^{0.36}_{0.36}$
[SiII]	34.82	< 17.46
[FeI]	34.71	< 14.72
[FeII] 25	25.99	< 3.14
[FeII] 35a	35.35	< 3.14
[FeII] 35b	35.78	< 5.39

Table B.11: Ionization narrow-line luminosities in NGC 3862.

Line	Central Wavelength (μm)	Luminosity ($10^{39}\,\mathrm{erg\,s^{-1}}$)
PAH	5.27	< 19.79
PAH	5.7	< 30.03
PAH	6.22	$65.52^{2.21}_{2.21}$
PAH	6.69	< 26.75
PAH	7.42	$144.02^{17.28}_{10.79}$
PAH	7.6	$25.4^{4.61}_{5.68}$
PAH	7.85	$63.85^{2.44}_{3.46}$
PAH	8.33	$27.65^{2.39}_{2.03}$
PAH	8.61	$26.76^{1.87}_{1.76}$
PAH	10.68	$7.19^{1.0}_{1.08}$
PAH	11.23	$12.81^{1.13}_{0.93}$
PAH	11.33	$60.34^{2.12}_{2.03}$
PAH	11.99	$36.97^{3.08}_{2.91}$
PAH	12.62	$50.61^{2.6}_{2.56}$
PAH	12.69	< 4.35
PAH	13.48	$29.78^{2.9}_{2.53}$
PAH	14.04	< 5.98
PAH	14.19	< 8.04
PAH	14.19	< 4.57
PAH	15.9	< 3.85
PAH	16.45	$5.38^{1.75}_{1.73}$
PAH	17.04	$32.92^{7.11}_{8.08}$
PAH	17.38	< 8.02
PAH	17.87	< 13.87
PAH	18.92	< 12.1
PAH	33.1	$24.39^{7.78}_{6.73}$

Table B.12: PAH narrow-line luminosities in NGC 3862.

Line	Central Wavelength (μm)	Luminosity ($10^{39}\,\mathrm{erg\,s^{-1}}$)
H2 S(7)	5.52	< 0.09
H2 S(6)	6.11	< 0.21
H2 S(5)	6.91	$0.19^{0.04}_{0.04}$
H2 S(4)	8.03	< 0.06
H2 S(3)	9.66	$0.21^{0.03}_{0.03}$
H2 S(2)	12.28	< 0.14
H2 S(1)	17.03	$0.19^{0.03}_{0.03}$
H2 S(0)	28.22	< 0.08
[ArII]	6.99	$0.52^{0.04}_{0.04}$
[ArIII]	8.99	$0.14^{0.03}_{0.02}$
[NeII]	12.81	$0.86^{0.02}_{0.03}$
[NeIII] 15	15.55	$1.19^{0.02}_{0.02}$
[NeIII] 36	35.01	< 0.07
[NeV] 14	14.32	< 0.21
[NeV] 24	24.32	< 0.03
[NeVI]	7.65	< 0.13
[OIV]	25.91	$0.32^{0.04}_{0.06}$
[SIII] 18	18.71	$0.73^{0.02}_{0.02}$
[SIII] 33	33.48	$1.12^{0.04}_{0.04}$
[SIV]	10.51	$0.14^{0.03}_{0.02}$
[SiII]	34.82	$2.62^{0.07}_{0.06}$
[FeI]	34.71	$0.42^{0.09}_{0.05}$
[FeII] 25	25.99	< 0.21
[FeII] 35a	35.35	< 0.16
[FeII] 35b	35.78	< 0.15

Table B.13: Ionization narrow-line luminosities in M 84.

Line	Central Wavelength (μm)	Luminosity ($10^{39}\,\mathrm{erg\,s^{-1}}$)
PAH	5.27	< 0.4
PAH	5.7	< 0.24
PAH	6.22	$2.8^{0.16}_{0.19}$
PAH	6.69	$1.2^{0.22}_{0.27}$
PAH	7.42	$2.07^{0.37}_{0.55}$
PAH	7.6	$1.14^{0.16}_{0.21}$
PAH	7.85	< 0.58
PAH	8.33	< 0.22
PAH	8.61	$0.43^{0.08}_{0.12}$
PAH	10.68	$0.39^{0.06}_{0.05}$
PAH	11.23	$0.74^{0.05}_{0.05}$
PAH	11.33	$4.56^{0.12}_{0.1}$
PAH	11.99	$1.35^{0.17}_{0.13}$
PAH	12.62	$2.26^{0.2}_{0.15}$
PAH	12.69	< 0.4
PAH	13.48	< 0.91
PAH	14.04	< 0.25
PAH	14.19	< 0.61
PAH	14.19	< 0.65
PAH	15.9	$0.14^{0.05}_{0.04}$
PAH	16.45	$0.43^{0.05}_{0.04}$
PAH	17.04	$3.44^{0.11}_{0.16}$
PAH	17.38	< 0.19
PAH	17.87	$0.29^{0.04}_{0.04}$
PAH	18.92	$0.55^{0.04}_{0.04}$
PAH	33.1	$0.78^{0.15}_{0.13}$

Table B.14: PAH narrow-line luminosities in M 84.

Line	Central Wavelength (μm)	Luminosity ($10^{39}\,\mathrm{erg\,s^{-1}}$)
H2 S(7)	5.52	< 29.45
H2 S(6)	6.11	< 55.1
H2 S(5)	6.91	< 47.06
H2 S(4)	8.03	< 14.66
H2 S(3)	9.66	< 22.81
H2 S(2)	12.28	< 8.77
H2 S(1)	17.03	< 20.89
H2 S(0)	28.22	< 8.4
[ArII]	6.99	$63.13^{10.4}_{9.51}$
[ArIII]	8.99	$14.41^{5.24}_{4.36}$
[NeII]	12.81	$57.99^{3.71}_{3.66}$
[NeIII] 15	15.55	$64.08^{4.26}_{3.59}$
[NeIII] 36	35.01	< 17.91
[NeV] 14	14.32	< 18.49
[NeV] 24	24.32	< 14.17
[NeVI]	7.65	< 35.74
[OIV]	25.91	< 19.85
[SIII] 18	18.71	$25.34^{5.42}_{4.52}$
[SIII] 33	33.48	< 52.4
[SIV]	10.51	< 18.7
[SiII]	34.82	$100.26^{14.02}_{11.33}$
[FeI]	34.71	$68.0^{11.87}_{12.37}$
[FeII] 25	25.99	< 17.82
[FeII] 35a	35.35	< 19.87
[FeII] 35b	35.78	< 21.65

Table B.15: Ionization narrow-line luminosities in M 87.

Line	Central Wavelength (μm)	Luminosity ($10^{39}\,\mathrm{erg\,s^{-1}}$)
PAH	5.27	< 116.31
PAH	5.7	< 153.33
PAH	6.22	$85.62^{24.4}_{24.32}$
PAH	6.69	$349.14^{60.38}_{58.13}$
PAH	7.42	< 284.3
PAH	7.6	< 97.11
PAH	7.85	< 51.18
PAH	8.33	< 43.98
PAH	8.61	< 44.18
PAH	10.68	$34.31^{8.76}_{8.69}$
PAH	11.23	< 18.8
PAH	11.33	< 84.32
PAH	11.99	$81.82^{21.72}_{18.65}$
PAH	12.62	< 111.92
PAH	12.69	< 41.13
PAH	13.48	< 94.77
PAH	14.04	< 50.02
PAH	14.19	< 79.21
PAH	14.19	< 61.03
PAH	15.9	< 24.02
PAH	16.45	< 45.7
PAH	17.04	< 68.98
PAH	17.38	< 30.78
PAH	17.87	$28.72^{8.77}_{9.52}$
PAH	18.92	< 52.04
PAH	33.1	< 105.06

Table B.16: PAH narrow-line luminosities in M 87.

Line	Central Wavelength (μm)	Luminosity ($10^{39}\,\mathrm{erg\,s^{-1}}$)
H2 S(7)	5.52	< 1.26
H2 S(6)	6.11	< 0.43
H2 S(5)	6.91	< 3.08
H2 S(4)	8.03	< 3.23
H2 S(3)	9.66	$1.99^{0.35}_{0.48}$
H2 S(2)	12.28	$1.52^{0.23}_{0.29}$
H2 S(1)	17.03	< 2.42
H2 S(0)	28.22	< 1.28
[ArII]	6.99	$12.46^{0.59}_{0.55}$
[ArIII]	8.99	< 0.76
[NeII]	12.81	$18.66^{0.34}_{0.39}$
[NeIII] 15	15.55	$5.81^{0.57}_{0.49}$
[NeIII] 36	35.01	< 15.52
[NeV] 14	14.32	< 9.6
[NeV] 24	24.32	< 1.56
[NeVI]	7.65	$2.76^{0.94}_{0.83}$
[OIV]	25.91	< 5.92
[SIII] 18	18.71	$4.47^{0.74}_{0.69}$
[SIII] 33	33.48	< 9.07
[SIV]	10.51	$1.35^{0.23}_{0.24}$
[SiII]	34.82	$26.0^{4.34}_{4.22}$
[FeI]	34.71	< 14.45
[FeII] 25	25.99	< 4.62
[FeII] 35a	35.35	< 3.61
[FeII] 35b	35.78	< 2.7

Table B.17: Ionization narrow-line luminosities in NGC 7052.

Line	Central Wavelength (μm)	Luminosity ($10^{39}\,\mathrm{erg\,s^{-1}}$)
PAH	5.27	$22.98^{9.03}_{3.83}$
PAH	5.7	$19.98^{1.79}_{2.1}$
PAH	6.22	$135.26^{2.02}_{3.2}$
PAH	6.69	$32.3^{4.86}_{6.06}$
PAH	7.42	$226.97^{11.88}_{19.69}$
PAH	7.6	$126.26^{3.98}_{4.71}$
PAH	7.85	$218.24^{3.19}_{3.03}$
PAH	8.33	$46.47^{2.35}_{2.53}$
PAH	8.61	$57.32^{2.07}_{1.63}$
PAH	10.68	$5.68^{0.62}_{0.58}$
PAH	11.23	$30.27^{0.93}_{0.93}$
PAH	11.33	$111.9^{1.59}_{1.66}$
PAH	11.99	$57.26^{1.76}_{1.74}$
PAH	12.62	$74.73^{2.38}_{2.84}$
PAH	12.69	$8.18^{0.99}_{0.76}$
PAH	13.48	< 10.59
PAH	14.04	< 7.97
PAH	14.19	< 14.95
PAH	14.19	< 12.89
PAH	15.9	< 4.01
PAH	16.45	$12.63^{1.21}_{1.37}$
PAH	17.04	$83.84^{5.46}_{4.6}$
PAH	17.38	$5.04^{1.27}_{1.14}$
PAH	17.87	$5.35^{1.5}_{1.64}$
PAH	18.92	< 11.46
PAH	33.1	$27.29^{4.96}_{5.09}$

Table B.18: PAH narrow-line luminosities in NGC 7052.

Appendix C

IRAC images

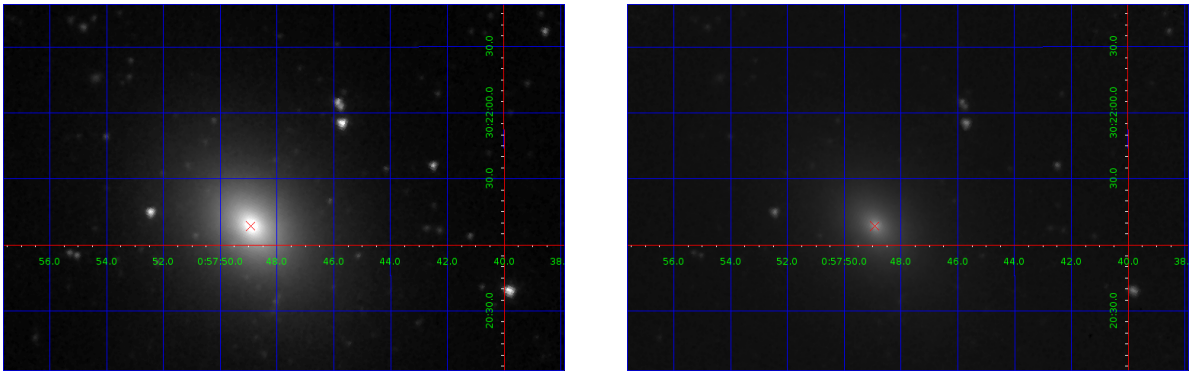

(a) Channel 1 (b) Channel 2

Figure C.1 IRAC images of NGC 315 with extraction locations

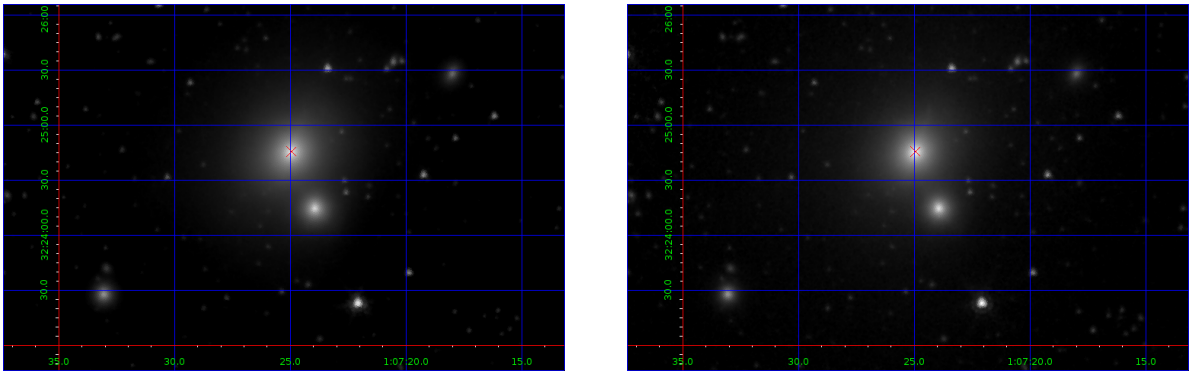

(a) Channel 1 (b) Channel 2

Figure C.2 IRAC images of 3C 31 with extraction locations

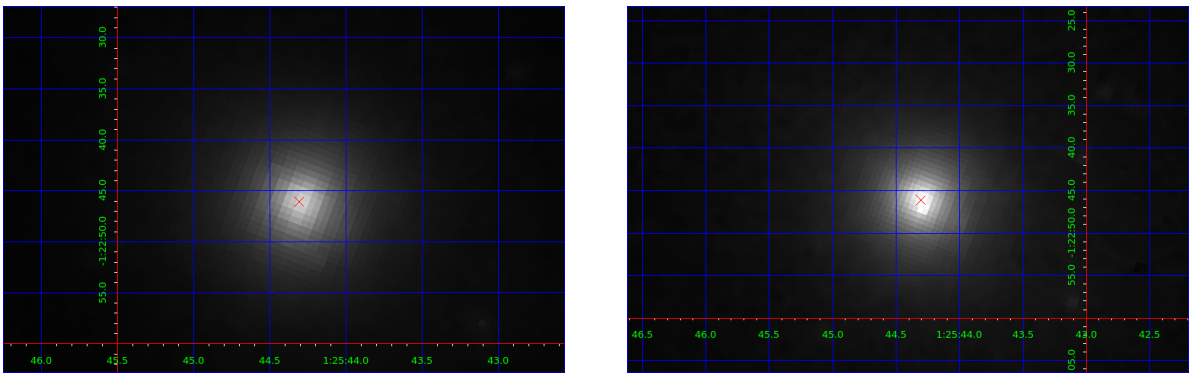

(a) Channel 1 (b) Channel 2

Figure C.3 IRAC images of NGC 541 with extraction locations

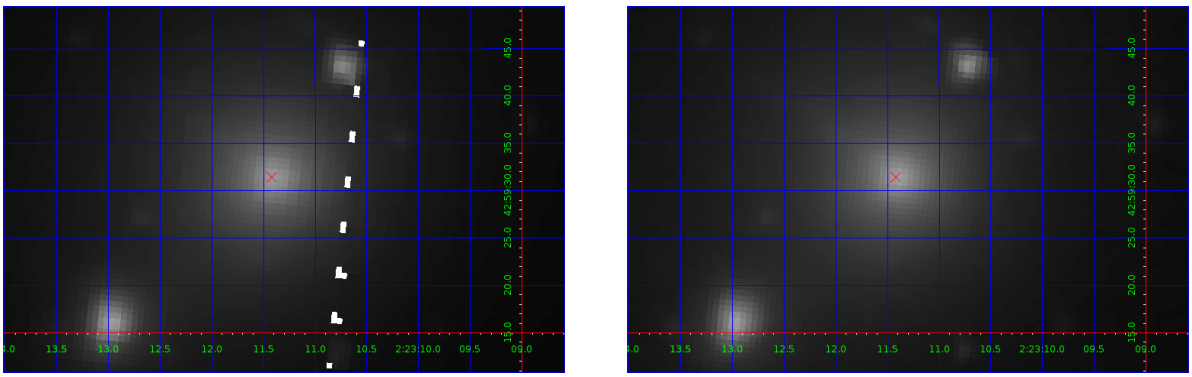

(a) Channel 1 (b) Channel 2

Figure C.4 IRAC images of 3C 66B with extraction locations

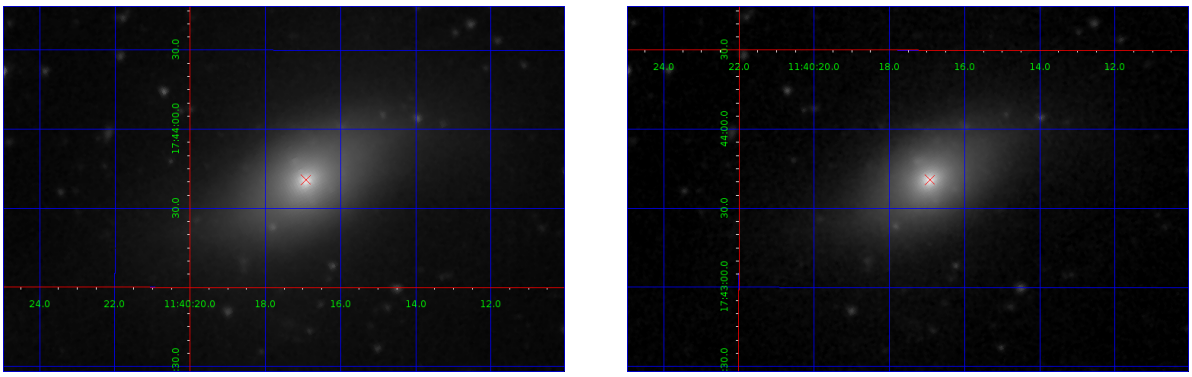

(a) Channel 1 (b) Channel 2

Figure C.5 IRAC images of NGC 3801 with extraction locations

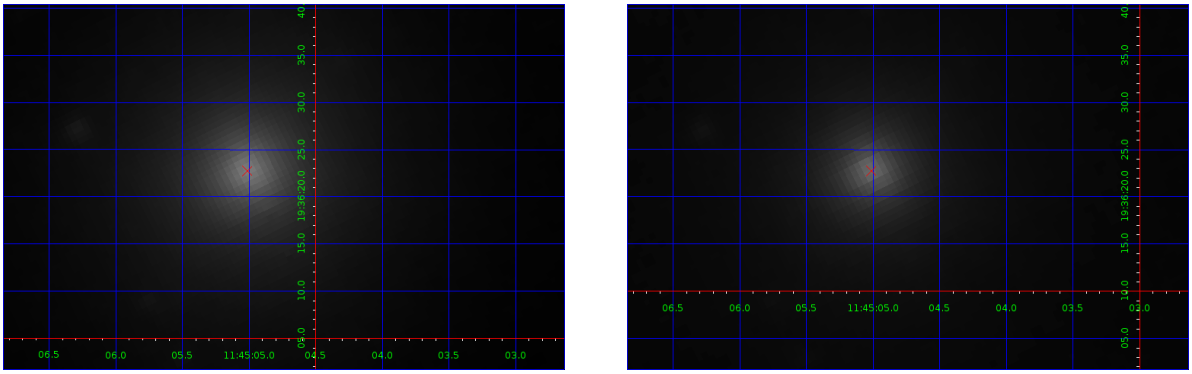

(a) Channel 1 (b) Channel 2

Figure C.6 IRAC images of NGC 3862 with extraction locations

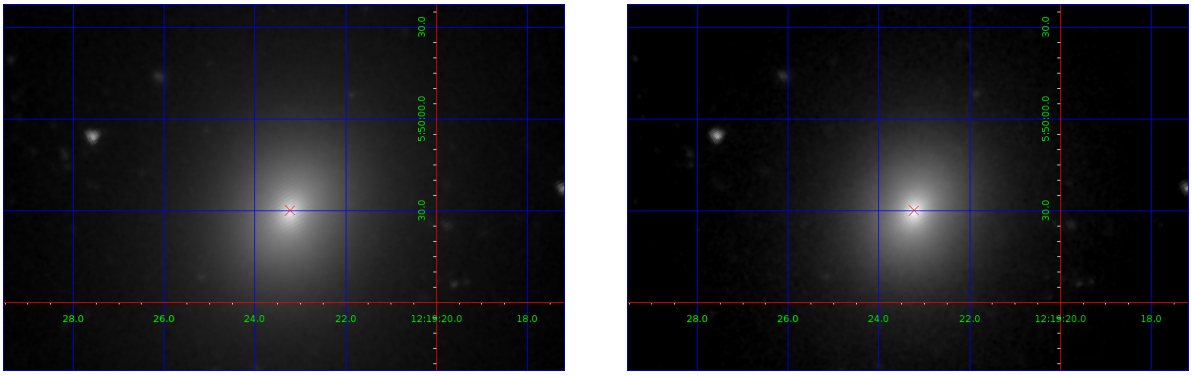

(a) Channel 1 (b) Channel 2

Figure C.7 IRAC images of 3C 270 with extraction locations

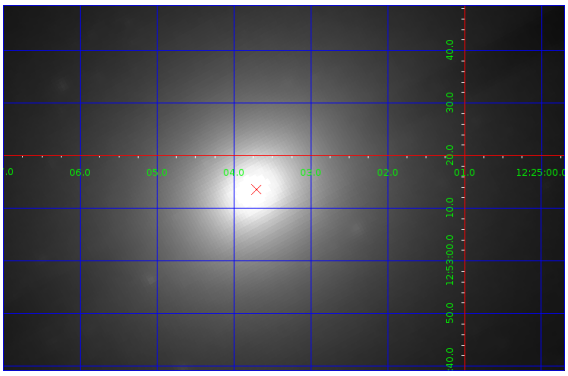

Figure C.8 IRAC channel 2 image of M 84 with extraction location

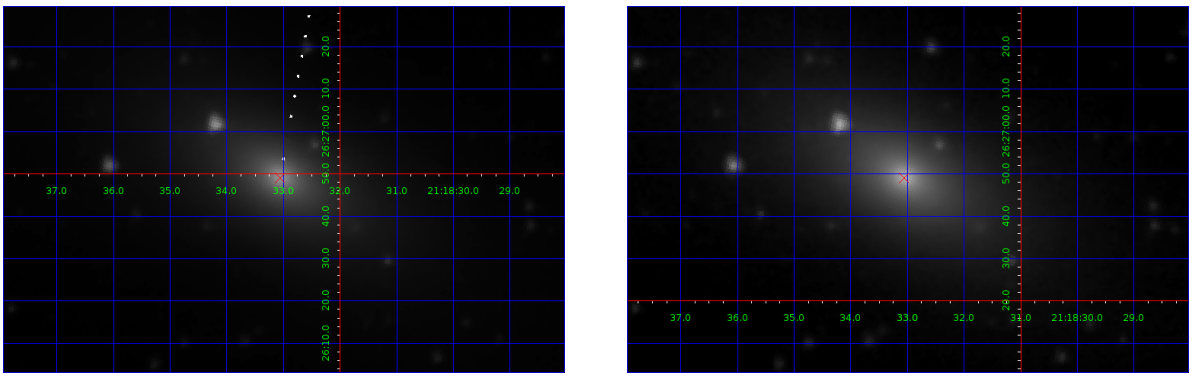

(a) Channel 1 (b) Channel 2

Figure C.9 IRAC images of NGC 7052 with extraction locations

Appendix D

MIPS images

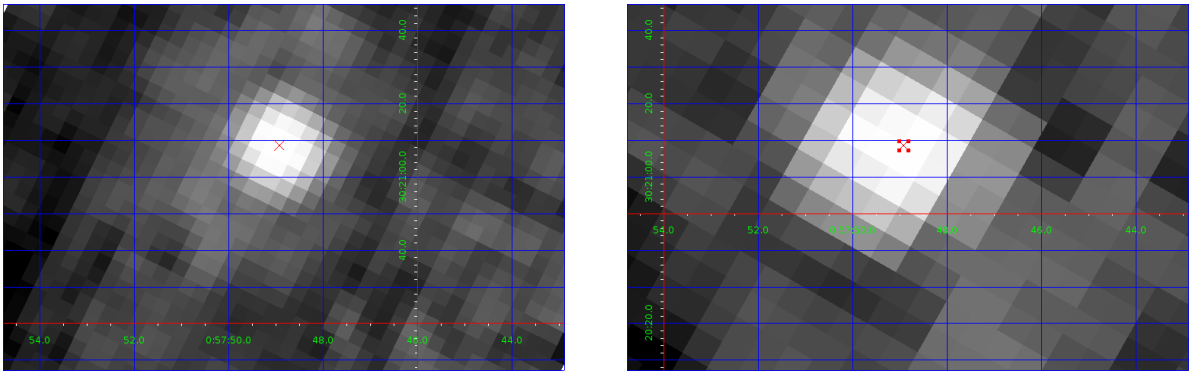

(a) Channel 2 (b) Channel 3

Figure D.1 MIPS images of NGC 315 with extraction locations

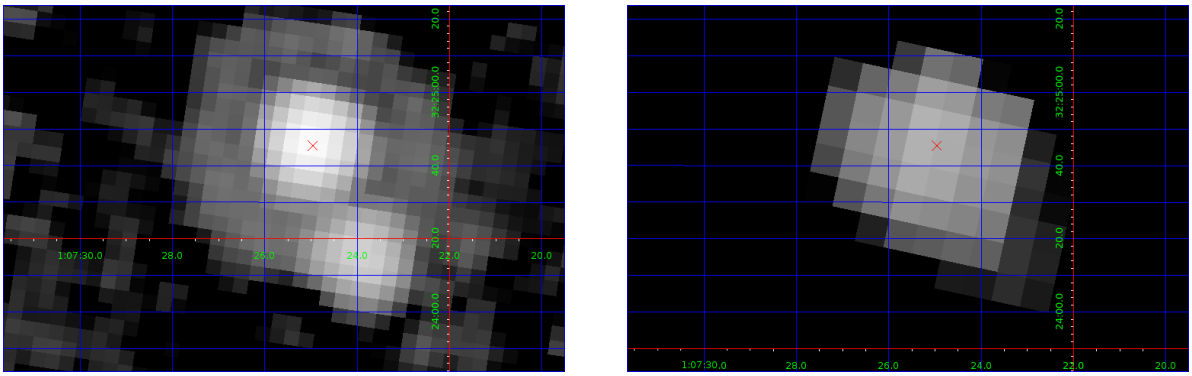

(a) Channel 2 (b) Channel 3

Figure D.2 MIPS images of 3C 31 with extraction locations

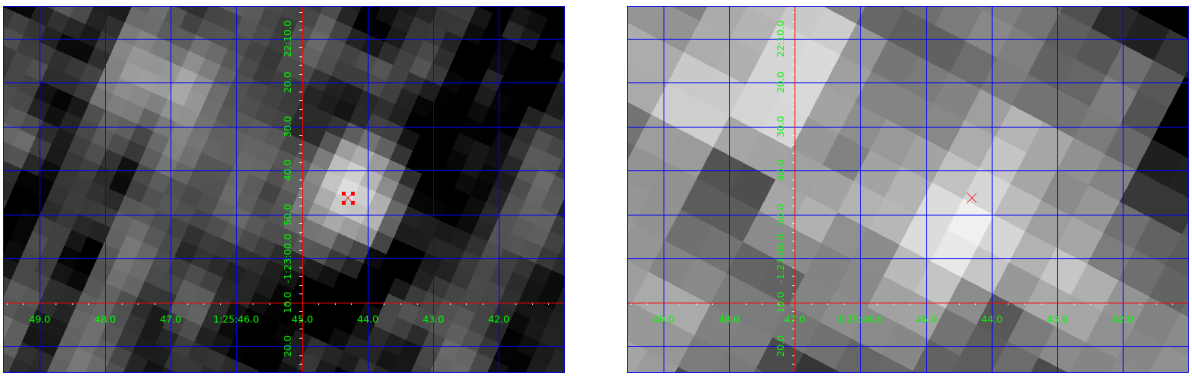

(a) Channel 2 (b) Channel 3

Figure D.3 MIPS images of NGC 541 with extraction locations

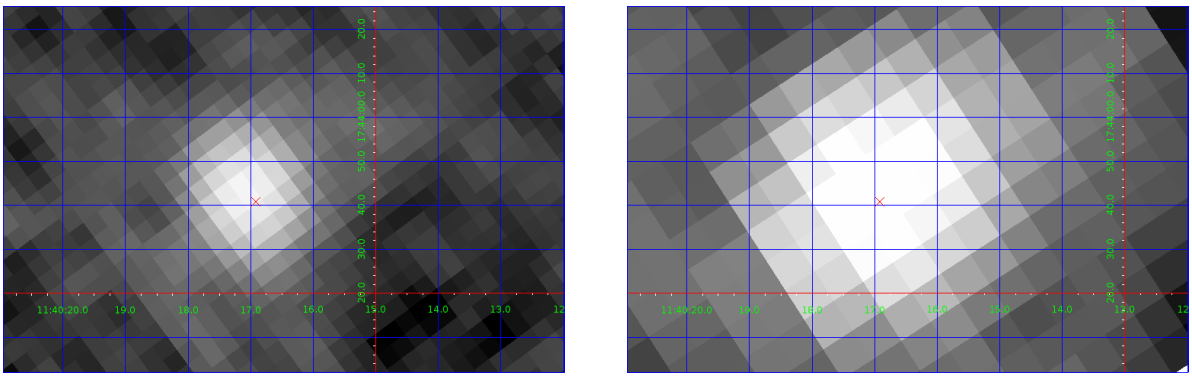

(a) Channel 2 (b) Channel 3

Figure D.4 MIPS images of NGC 3801 with extraction locations

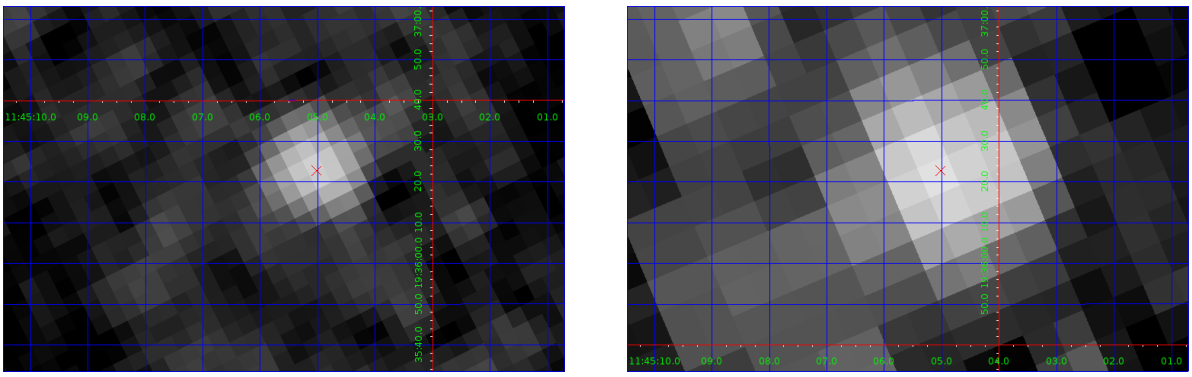

(a) Channel 2 (b) Channel 3

Figure D.5 MIPS images of NGC 3862 with extraction locations

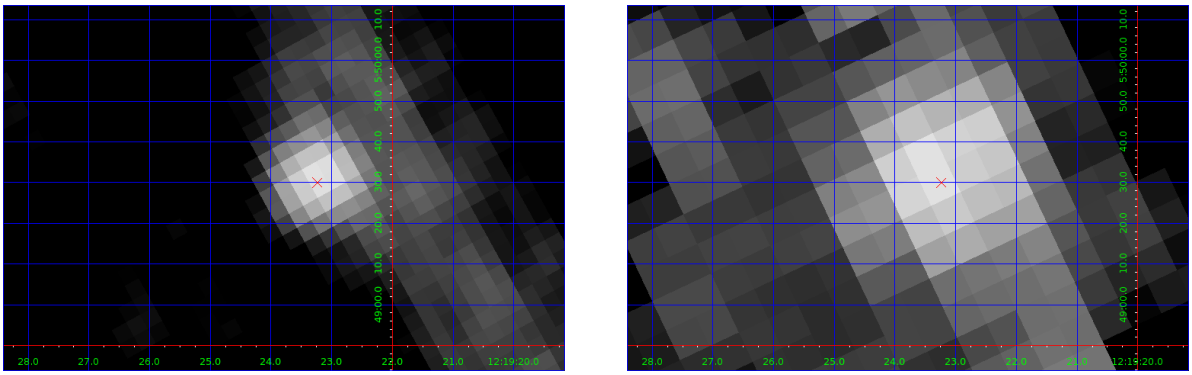

(a) Channel 2 (b) Channel 3

Figure D.6 MIPS images of 3C 270 with extraction locations

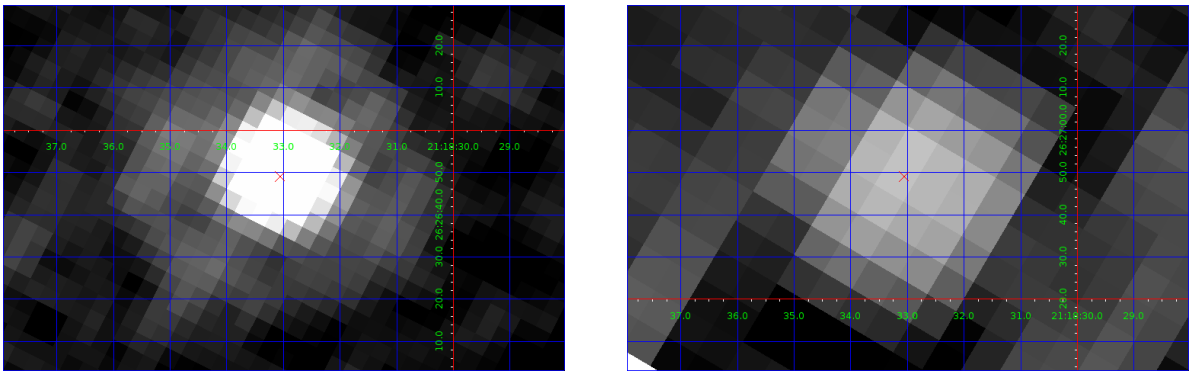

(a) Channel 2 (b) Channel 3

Figure D.7 MIPS images of NGC 7052 with extraction locations

Appendix E

Acknowledgements: Software, Instruments and Archives

This research has made use of the NASA/ IPAC Infrared Science Archive, which is operated by the Jet Propulsion Laboratory, California Institute of Technology, under contract with the National Aeronautics and Space Administration.

This research has made use of the NASA/IPAC Extragalactic Database (NED), which is operated by the Jet Propulsion Laboratory, California Institute of Technology, under contract with the National Aeronautics and Space Administration.

This work is based in part on observations made with the Spitzer Space Telescope, which is operated by the Jet Propulsion Laboratory, California Institute of Technology under a contract with NASA.

SPIRE has been developed by a consortium of institutes led by Cardiff University (UK) and including Univ. Lethbridge (Canada); NAOC (China); CEA, LAM (France); IFSI, Univ. Padua (Italy); IAC (Spain); Stockholm Observatory (Sweden); Imperial College London, RAL, UCL-MSSL, UKATC, Univ. Sussex (UK); and Caltech, JPL, NHSC, Univ. Colorado (USA). This development has been supported by national funding agencies: CSA (Canada); NAOC (China); CEA, CNES, CNRS (France); ASI (Italy); MCINN (Spain);

SNSB (Sweden); STFC, UKSA (UK); and NASA (USA).

Herschel is an ESA space observatory with science instruments provided by European-led Principal Investigator consortia and with important participation from NASA.